Fermilab FERMILAB-THESIS-1995-32

The Lead Jet Pseudorapidity Distribution of Direct Photon Events in $p\bar{p}$ Collisions at $\sqrt{s} = 1.8$ TeV

by Carol Margaret Hawk

A dissertation submitted to the

Graduate School— New Brunswick

Rutgers, The State University of New Jersey

in partial fulfillment of the requirements

for the degree of

Doctor of Philosophy

Graduate Program in Physics and Astronomy

Written under the direction of

Thomas J. Devlin

and approved by

New Brunswick, New Jersey

January, 1996

ABSTRACT OF THE DISSERTATION

The Lead Jet Pseudorapidity Distribution of Direct Photon Events in $p\bar{p}$ Collisions at $\sqrt{s} = 1.8$ TeV

by Carol Margaret Hawk

Dissertation Director: Thomas J. Devlin

The lead jet pseudorapidity distribution in direct photon events probes the kinematic region of Bjorken x between 0.015 and 0.15 and discriminates among parton distributions. Direct photon production directly probes the gluon distribution through the leading order Quantum Chromodynamics Compton process. The data are from $p\bar{p}$ collisions at a total center-of-mass energy of 1.8 TeV recorded with the Collider Detector at Fermilab (CDF) in the 1992-1993 run.

Acknowledgements

Throughout my life I have been continuously surrounded by caring, generous, and talented people. The teachers that befriended and mentored me when I was younger I remember with great fondness. Alan Krueger, my biology teacher in 9th grade, gave me one opportunity after the next and supported me every step of the way. He introduced me to the St. George's School of Oceanography that was lovingly orchestrated by Stephen Leslie. Richard Blanquet welcomed me into his lab at Georgetown University and, under his kind supervision, I was able to continue the biochemistry research I began at St. George's. Bill Robertson introduced me to the fascinating world of physics, Michael Hoover showed me the brilliant prism of literature, and Alan Graham showed me the beauty of wood-working.

At UMASS Richard Kofler's passion for physics and concern for each of the ≈ 600 students in his introductory course turned my attention toward this field. Hajime Sakai welcomed me into his lab and showed me great kindness.

At UVA Dan Larson stood by me during a critical time. Bill Towler, a man of limitless vitality and curiosity, guided my research and gave me his friendship. George Plum gave me half of his counter space and all of his support in the machine shop.

At Rutgers Joseph Sak and Arum Mekjian were particularly kind and careful teachers. Cyrus Taylor's warmth and talent made his class a delight and his friendship a true fortune. Ruth Bennett deftly eased the administrative routine.

At Fermilab, my fellow graduate students offered enlightening physics discussions, constant encouragement, and many fun times. The Rutgers high energy folks have been a pleasure to work with. Rob Kennedy, Cal Loomis, Jodi Lamoureux, and Michael Traynor read various parts of this thesis. My advisor, Tom Devlin, gave me the opportunity to work on CDF, provided constant support, and was a fair and effective manager. His revisions to this document greatly enhanced its quality. Steve Kuhlmann introduced me to the photon group and launched this analysis. Jodi Lamoureux and Steve Behrends also made very significant contributions. Jorge Morfin, Eve Kovacs, and Joey Huston explained the theoretical issues to me.

My friends and family have been endlessly supportive. Sue Dillon, a woman of tremendous talent and tenacity, shared my journey through graduate school. Robert and Phyllis Traynor, and their entire family, welcomed me into their home. My Aunt Kate has constantly showered me with encouragement and affection. My sister Cathy, with her unfailing humor and generosity, has been a constant source of support over the years. Cathy's husband Larry, and their daughter, Lida Ann, have brought much joy to our family. Mom and Dad are two of the most caring, talented, wonderful people I know. They have inspired and nourished me every day of my life. I am honored to be their daughter.

Michael Traynor, who has my greatest love and respect, has contributed to this analysis professionally and, in addition, has provided constant encouragement along the way.

Dedication

To my parents,

Lida Jane and Arthur Leonard Hawk

Table of Contents

Abstract ii

Acknowledgements iii

Dedication v

List of Tables xi

List of Figures xiv

1. Introduction 1

2. Theory 3

2.1. The Standard Model 6

2.2. Quantum Chromodynamics 8

2.2.1. Asymptotic Freedom and Color Confinement 8

2.3. The Running Couplings $\alpha(Q^2)$ and $\alpha_s(Q^2)$ 9

2.4. Feynman Rules for Parton-Level Cross Section Calculation 11

2.5. Parton Distributions 11

2.6. Direct Photon Production 12

2.6.1. The Underlying Event 16

2.7. Momentum Scales Eliminate Singularities in the Cross Section Calculation 16

2.8. Q^2 Evolution of Parton Distributions 17

2.9. Extraction of Parton Distributions from Experimental Data 19

2.10. Partonic Fragmentation and Hadronization to Produce Jets 20

2.10.1. The Effect of Soft Gluon Radiation on Photon + 1 Jet Event Topology 21

2.11. Using Photon + Jet Kinematics to Select Events in Regions of Specific Parton x 21

2.12. The Multiple Photon Background 24

2.13. Next-to-Leading-Order Calculation of the Direct Photon Cross Section 26

3. Accelerator and Detector 28

3.1. The CDF Detector 30

3.1.1. The Central Tracking Chamber 31

3.1.2. The Central Drift Tube Array 35

3.1.3. The Central Preradiator 35

3.1.4. The Central Calorimeter 35

3.1.5. The Central Electromagnetic Calorimeter 36

3.1.6. The Central Electromagnetic Strip Chamber 38

3.1.7. The Central and End Wall Hadronic Calorimeters 38

3.1.8. Calibration of the Scintillator Based Calorimeters 39

3.1.9. The End Plug Electromagnetic Calorimeter 40

3.1.10. The End Plug Hadronic Calorimeter 41

3.1.11. The Forward Electromagnetic Calorimeter 41

3.1.12. The Forward Hadronic Calorimeter 42

3.1.13. Calibration of the Gas Based Calorimeters 42

3.1.14. Detector Access Regions (Cracks) 43

3.2. The Data Acquisition System 44

3.2.1. Level 1 45

3.2.2. Level 2 46

3.2.3. Level 3 47

4. Event Selection and Corrections to the Data 48

4.1. Efficiency of Online Cuts 50

4.2. Offline Production 51

4.3. Offline Physics Analysis 52

4.4. Background Subtraction 55

4.5. Correction of the Jet Transverse Energy 61

5. Measurement of the Lead Jet η Distribution 64

5.1. The Magnitude of the Detector Effects 67

5.1.1. Detector η Resolution: Detector Effects That Alter the Distribution of E_t Within the Jet $\eta - \phi$ Cone 68

5.1.2. Misidentification of the Lead Jet 69

5.2. Correction of Detector Effects 70

5.3. Systematic Uncertainty Associated with Detector Effects 71

5.4. Systematic Uncertainty Associated with Background Subtraction 75

5.5. Final Statistical and Systematic Uncertainty 75

6. Conclusion and Discussion of the Measurement 76

6.1. Theoretical Uncertainty: the Renormalization Scale 77

Appendix A. Finding μ_F, Factorization Methods 78

Appendix B. The $p\bar{p}$ Beam 79

B.1. Longitudinal Synchrotron Oscillations 79

B.1.1. Bunch Rotation 80

B.2. Transverse Betatron Oscillations 81

B.3. Production of the Proton Beam 82

B.4. Production of the Antiproton Beam 83

B.5. Collision of the Proton and Antiproton Beams 84

Appendix C. The Level 3 Trigger 86

C.1. The Level 3 Hardware 86

C.2. Software Used to Control the Event Flow 87

C.3. The Data Structure Input to Level 3 88

C.4. Manipulation of the Data Within Level 3 89

C.5. The Data Structure Output By Level 3 91

Appendix D. Selection of the Lead Jet 92

Appendix E. The Back-to-Back Cut Selects Events of Limited K_t That Contain Correctly Identified Lead Jets 94

E.1. The Back-to-Back Cut Rejects Events Strongly Affected by K_t 96

E.2. The Back-to-Back Cut Rejects Events that Contain Misidentified Lead Jets 96

E.2.1. The Back-to-Back Cut Eliminates Events that Contain No Reconstructed Jet 96

E.2.2. The Back-to-Back Cut Rejects Events in which Underlying Event Energy Replaces the Lead Jet 97

E.2.3. The Back-to-Back Cut Rejects $2 \rightarrow 3$ Events in which the Lead and Second Jets Interchange 98

The Photon + 2 Jet Component in the Data 99

The Interchange of Lead and Second Jets in $2 \rightarrow 3$ Events . . . 100

Appendix F. The Detector Jet η Resolution 108

F.0.4. The Dependence of Jet η Resolution on Jet E_t 109

Appendix G. Deconvolution of the Lead Jet η Distribution 111

Appendix H. The Lead Jet η Resolution in Simulated Events of Various Topology 118

Appendix I. The Systematic Uncertainty Associated with the Detector Simulation 123

Appendix J. The Systematic Uncertainty Associated With the Underlying Event Simulation 127

Appendix K. The Systematic Uncertainty Associated With Photon + 2 Jet Events 129

Appendix L. The Systematic Uncertainty Associated With K_t and Variation of the Back-to-Back Cut 130

Appendix M. The Systematic Uncertainty Associated With the Spectrum Dependence of the Deconvolution Procedure 132

Appendix N. The Systematic Uncertainty Associated with the Background Subtraction 134

Appendix O. The CDF Collaboration 135

References 138

Vita 140

List of Tables

2.1. Fundamental particles of the Standard Model 6

2.2. The parton distribution sets used in this analysis and the corresponding Λ_{QCD} for four flavors are presented here. All of these sets use the $\overline{MS}$ factorization scheme. 20

4.1. Selection criteria for direct photon candidates. 52

4.2. The predicted and measured conversion rates of photons in the material preceding the CPR. 59

5.1. The changes in the measurement that result from the correction of detector effects. 72

5.2. The final statistical and systematic uncertainty. 75

6.1. Results for different renormalization scales. 77

E.1. The percentage of events in which the photon and lead jet are back-to-back within $\pm\phi_{CUT}$. 95

E.2. Unreconstructed jets alter the lead jet η distribution. 97

E.3. $2 \rightarrow 2$+UE+K_t events combine detector effects that change the distribution of E_t within the jet $\eta - \phi$ cone with those that replace the lead jet with underlying event energy. 98

E.4. Comparison of $2 \rightarrow 2+K_t$ events with $2 \rightarrow 2$+UE+K_t events demonstrates the effect of underlying event on the lead jet η distribution. 98

E.5. The effect of the back-to-back cut on the fraction of $2 \rightarrow 3+\mathrm{UE}+K_t$ events that contain interchanged lead and second jets. 105

E.6. $2 \rightarrow 3+\mathrm{UE}+K_t$ events with interchanged lead and second jets would typically fail the back-to-back cut whether or not the jets had interchanged. 105

E.7. Interchange of the lead and second jets in $2 \rightarrow 3+\mathrm{UE}+K_t$ events alters the lead jet η distribution. 106

F.1. Detector effects that change the distribution of E_t within the $\eta - \phi$ jet cone shift the E_t-weighted jet centroid and alter the lead jet η distribution. 108

G.1. To test the deconvolution procedure, the corrected simulated jet η distribution is compared to the corresponding generated parton η distribution. 117

I.1. The sensitivity of the deconvolution matrix, Ω^{-1}, to the simulated distribution of jet E_t near the detector η cracks. 125

I.2. Events simulated with a non-standard distribution of energy within the jet $\eta - \phi$ cone for jets that overlap the η cracks show expected η dependent fluctuations in mean jet E_t. 126

J.1. The sensitivity of the deconvolution matrix, Ω^{-1}, to the underlying event. 127

J.2. A comparison between E_t clusters in minimum bias events and in the underlying event simulation. 128

K.1. The sensitivity of the deconvolution matrix, Ω^{-1}, to the $2 \rightarrow 3$ process. 129

L.1. The sensitivity of the deconvolution matrix, Ω^{-1}, to variation of the back-to-back cut. 130

L.2. The sensitivity of the deconvolution matrix, Ω^{-1}, to the effect of K_t. . . 131

M.1. The sensitivity of the deconvolution matrix, Ω^{-1}, to the η spectrum of the generated events. 133

N.1. The systematic uncertainty associated with the subtraction of multiple photon background. 134

List of Figures

2.1. A gluon self coupling diagram. Gluons propagate the color field and they themselves carry color charge. 10

2.2. The strong force running coupling, $\alpha_s(Q^2)$. 11

2.3. A comparison of parton distributions for the up valance quark, the down valance quark, the sea quarks and the gluons. 13

2.4. Of the total LO cross section, the fraction due to the annihilation process as a function of photon P_t. 13

2.5. LO and NLO Feynman diagrams for direct photon production. 14

2.6. A probe of higher Q^2 resolves structure on a smaller scale. 18

2.7. The Q^2 evolution of the CTEQ2M parton distributions $U_v(x)$ and $G(x)$. 18

2.8. The $\Delta\phi$ between the photon and the lead jet in generated $2 \rightarrow 2$+UE events and $2 \rightarrow 2$+UE+K_t events. 22

2.9. The range of parton x probed by the lead jet η distribution. 23

2.10. The average photon P_t exhibits little dependence on lead jet η. 24

2.11. Feynman diagrams for dijet production. 24

2.12. The ratio of direct photon events to multiple photon events. 26

3.1. A schematic of the Fermilab $p\bar{p}$ accelerator. 29

3.2. A schematic of the CDF detector. 31

3.3. A cross section of the CDF detector. 32

3.4. An end view of the Central Tracking Chamber. 34

3.5. A schematic drawing of one wedge in the Central Electromagnetic Calorimeter. 37

3.6. A schematic in $\eta_D - \phi$ space of the hadronic towers for the Central, End Wall, End Plug and Forward calorimeters. 43

4.1. Efficiencies for the profile and the conversion methods of background subtraction. 58

4.2. Reconstructed mesons are used for calibration of the CPR. 60

4.3. The inclusive direct photon cross section measured at CDF. 61

5.1. The uncorrected lead jet η distribution with small binning to demonstrate the detector effects and with the large binning used in the final measurement to minimize corrections to each bin. 65

5.2. Changes to the distribution of E_t within the jet $\eta - \phi$ cone affect the measured lead jet η distribution. 69

5.3. Lead jet misidentification affects the measured lead jet η distribution. . 70

5.4. The lead jet η distribution corrected for detector effects. 71

5.5. The lead jet η distribution normalized to the value of the first bin and divided by the NLO theory based on CTEQ2M parton distributions. Both corrected and uncorrected data are presented. 73

5.6. Variations in the corrected data corresponding to variations in the simulated events. 74

6.1. The lead jet η distribution normalized to the value of the first bin and divided by the NLO theory based on CTEQ2M parton distributions. 76

6.2. The effect of variation in the μ_R^2 scale in the theory. 77

D.1. A comparison in the data between the E_t spectra of the photon and the lead jet from the hard scattering, and the second jet, generally unassociated with the hard scattering. 92

D.2. Additional jets unassociated with the hard scattering event are reconstructed in the data. 93

E.1. $\Delta\phi$ between the photon and lead jet in the data. 94

E.2. $r(\eta, \phi) = (\Delta\eta^2 + \Delta\phi^2)^{1/2}$ between the photon and the second jet for $2 \rightarrow 2$+UE simulated events. 99

E.3. Event kinematics of data events that pass the back-to-back cut and those that fail. 101

E.4. Event kinematics of $2 \rightarrow 3$+UE+K_t simulated events that pass the back-to-back cut and those that fail. 102

E.5. Identification of $2 \rightarrow 3$+UE+K_t simulated events that contain interchanged lead and second jets. 104

E.6. Event kinematics of $2 \rightarrow 3$+UE+K_t simulated events in which the lead and second jets were interchanged. Events that pass the back-to-back cut and those that fail are compared. 107

F.1. The typical distance of separation in η between the parton and the corresponding jet. 109

F.2. A comparison of detector η resolution between different event topologies and in different lead jet E_t ranges. 110

F.3. A comparison of the lead jet E_t distributions in the $2 \rightarrow 2$+UE+K_t events and in the $2 \rightarrow 3$+UE+K_t events. 110

G.1. A study of detector η resolution according to the 2 $\rightarrow$ 2+UE+K_t simulated events. 112

G.2. The data before and after correction for detector effects. 117

H.1. A study of detector η resolution according to the 2 $\rightarrow$ 2 simulated events. 119

H.2. A study of detector η resolution according to the 2 $\rightarrow$ 2+UE simulated events. 120

H.3. A study of detector η resolution according to the 2 $\rightarrow$ 2+UE+K_t simulated events. 121

H.4. A study of detector η resolution according to the 2 $\rightarrow$ 3+UE+K_t simulated events. 122

I.1. The balance in transverse momentum of dijet events in the data and in the detector simulation. 126

J.1. A comparison between the E_t spectra of clusters in minimum bias events and in the simulated underlying event. 128

M.1. A comparison between the lead jet η spectrum corresponding to Martinelli parton distributions and that corresponding to CTEQ2M parton distributions. 133

Chapter 1

Introduction

Direct photon production in $p\bar{p}$ collisions at high energy provides a means of investigating the internal structure of the proton (or antiproton) on a distance scale of $\approx 10^{-17}$ m and below. In this kinematic regime the proton's constituent partons (quarks and gluons) behave as quasi-free particles. A hard collision between partons can result in outgoing products that emerge at large angles relative to the incident direction. The momenta of the colliding partons is reflected in the angular distribution of the outgoing products. In particular, direct photon production produces a photon and a jet from the hard collision and can result from either a quark-antiquark interaction or a quark-gluon interaction. Because of the latter process, direct photon production provides a direct probe of the momentum distribution among the gluons.

This distribution is mathematically expressed in terms of parton distribution functions, i.e. probability functions that use the fraction, x, of the proton's momentum carried by each parton as the independent variable. Quantum Chromodynamics (QCD) describes the interactions between quarks and gluons and, together with the experimentally determined parton distributions, provides a means to calculate the probabilities for final states resulting from $p\bar{p}$ collisions.

A wide range of experiments and some theoretical constraints have been quite successful in determining the distribution functions for quarks and gluons over a range of x.

However, there are uncertainties in these calculations, and a number of alternative sets of distribution functions are consistent with existing data. This measurement provides a test of parton distributions and will be used to refine the current understanding of the form these functions take.

In Chapter 2, theoretical considerations for this topic are presented. Chapter 3 describes the apparatus and procedures used to produce a large sample of events in which a hard scattering interaction produced a direct photon and jet in the final state. Chapter 4 presents the first stage of data analysis in which the raw events were subjected to various criteria to select direct photon events and to eliminate backgrounds. From these events, the pseudorapidity distribution of the jet was calculated for comparison with those predicted by various sets of parton distributions. This is described in Chapter 5. Chapter 6 provides a summary and conclusion. A number of supporting discussions are given in Appendices.

Chapter 2

Theory

This chapter contains the theoretical context of the analysis. It begins with a discussion of the Standard Model which describes the fundamental particles and their interactions and, of particular relevance to this analysis, the color interactions of the strong force described by Quantum Chromodynamics (QCD).

Perturbative calculations of cross sections for strong force interactions are possible because of asymptotic freedom, the behavior of partons as quasi-free particles at high momentum transfer, Q. The running coupling, $\alpha_s(Q^2)$, decreases as Q^2 increases.

The parton-level cross section describes the probability that two partons of momenta, x_a and x_b respectively, experience a hard scattering that produces two other partons of momenta, x_c and x_d respectively. This calculation is guided by the Feynman rules which assign mathematical expressions to specific aspects of each interaction.

The proton is a complex system of three valance quarks, gluons, and virtual $q\bar{q}$ pairs, or sea quarks. Parton distributions describe the distribution of the proton's momentum among the constituent partons.

The measured cross section for direct photon production includes all processes that produce a photon directly from the initial hard scattering event, that is, not as a secondary decay product. The $2 \rightarrow 2$ processes are $q\bar{q} \rightarrow g\gamma$ and $qg \rightarrow q\gamma$.

Energy from soft collisions, at large impact parameter, between uninvolved, or spectator, partons underlies the hard scattering event. These low energy interactions defy perturbative calculation but yield to experimental measurement.

Low energy processes result in infrared divergences in the cross section calculation. Quarks emit soft gluons of momentum $p \to 0$, directed nearly collinear to the quark momentum. Factorization eliminates the infrared divergence. It leaves the parton distributions, extracted using experimental data and theoretical calculations together, dependent on the factorization momentum scale, μ_F, which is usually set equal to Q^2.

High energy processes result in ultraviolet divergences in the cross section calculation. Gluons become virtual $q\bar{q}$ pairs of possibly infinite energy E that exist for $t \approx \hbar/E$ before reforming to gluons. Renormalization eliminates the ultraviolet divergence. It leaves the calculated strong coupling dependent on the renormalization momentum scale, μ_R, which is usually set equal to Q^2.

Both μ_F and μ_R will be discussed in detail presently. These momentum scales are made necessary by our inability to perform the perturbative calculation of the cross section to all orders in α_s. The total cross section is a physical quantity that includes all possible subprocesses and must not depend on any scale.

Parton distributions evolve in Q^2 to reflect structure accessible in different kinematic regimes. Higher Q^2 probes shorter time and distance scales.

Final state partons are not observed directly. They fragment and hadronize to produce an observable jet of particles. Fragmentation functions describe the probability that this process yields some hadron, h, that carries the fraction z, of the parent parton's momentum.

The calculated cross section is a sum of terms, each of which represents one contributing subprocess. Each term is the product of the appropriate subprocess cross section, running couplings, parton distributions, and, where relevant, fragmentation functions. To extract the parton distribution from experimental data, the parameters of an assumed functional form are varied until the measured cross section and the calculated cross section agree within specified limits.

This process leaves the extracted parton distributions dependent on the following:

- The order in α_s to which the parton-level cross sections were calculated.
- The momentum scales μ_R, μ_F and Λ_{QCD}.

Also, the extracted partons distributions are only valid in the parton momentum range accessible to the experimental data.

Events created by the collision of partons with similar x produce a jet in the central detector since the photon is constrained to have $|\eta| < 0.9$. Events created by the collision of partons with dissimilar x produce a jet in the forward detector. The lead jet $\eta = -ln(tan(\theta/2))$ distribution in direct photon events measures the separation in x of the colliding partons. This separation increases with the jet η coordinate. Here, θ represents the polar angle in the CDF coordinate system, ϕ the azimuthal angle, and z the direction of the proton beam.

A next-to-leading order (NLO) calculation [9] of direct photon production provides the theoretical comparison to this measurement. Other computer programs provide information used for correction of detector effects and estimation of the associated systematic uncertainty. A Monte Carlo subroutine, PAPAGENO [15], generates events at the parton level, a second subroutine, SETPRT [16], fragments the outgoing partons

and a final subroutine, QFL [17], simulates the response of the detector to the resulting hadrons.

2.1 The Standard Model

The four fundamental forces of nature, gravitational, weak, strong, and electromagnetic, are each described as an energy field propagated by an intermediate boson, a particle of integral spin. The gravitational force is mediated by the as yet unobserved graviton, the electroweak force by the photon, Z^o, and W^{+-}, and the strong force by gluons.

These mediating bosons govern the interactions between the basic particles of matter which are, according to the Standard Model, the three generations of fermions, particles of half integral spin. Each generation consists of a lepton, a neutrino and two types, or flavors, of quark, These are listed in Tab. 2.1.

	Quarks	q($\|e\|$)	Leptons	q($\|e\|$)
First Generation	**d***own*	-1/3	e	-1
	u*p*	+2/3	ν_e	0
Second Generation	**s***trange*	-1/3	μ	-1
	c*harm*	+2/3	ν_μ	0
Third Generation	**b***ottom*	-1/3	τ	-1
	t*op* [8]	+2/3	ν_τ	0

Table 2.1: The fundamental particles of the Standard Model. The electromagnetic charge, q, is given in terms of the electron's charge.

To conserve 4-momentum, a boson mediating the interaction between particles must borrow the energy, E, from the vacuum. Heisenberg's uncertainty principle is satisfied since the boson exists only for the time $\Delta t \approx \frac{\hbar}{E}$. The intermediate boson is called *virtual*, or off-mass-shell, because during its existence the invariant mass of the system exceeds the available energy, $E^2 - P^2 < m^2$.

Each fermion in Tab. 2.1 is accompanied by an antifermion. This was first recognized with Dirac's relativistic wave equation for a freely propagating fermion,

$$i\frac{\partial\Psi(\vec{x},t)}{\partial t} = (-i\vec{\alpha}\cdot\vec{\nabla} + \beta m)\Psi(\vec{x},t).$$

Here $\hbar \equiv c \equiv 1$, the mass of the fermion is given as m,

$$\alpha_i = \begin{pmatrix} 0 & \sigma_i \\ \sigma_i & 0 \end{pmatrix},$$

and

$$\beta = \begin{pmatrix} \mathbf{1} & 0 \\ 0 & -\mathbf{1} \end{pmatrix},$$

where the σ_i are the usual Pauli matrices and $\mathbf{1}$ represents the 2×2 unit matrix.

The wavefunction Ψ is written as a *spinor* such that $\Psi \approx we^{-i(Et-\vec{p}\cdot\vec{x})}$ where w is a column vector.

This equation is solved for the particle energy,

$$E = \pm(p^2 + m^2)^{\frac{1}{2}}.$$

Dirac's equation yields both a positive and a negative solution for the energy of a freely propagating electron. The negative energy solution represents an antielectron, or positron, later described by Feynman as an electron traveling backwards in time.

Photons can exist as virtual $e\bar{e}$ pairs for a time $\Delta t \approx \frac{\hbar}{\Delta E}$. Here ΔE has been borrowed from the vacuum and is the additional energy required to create the virtual $e\bar{e}$ pair. In analogy, the gluon can exist as a virtual $q\bar{q}$ pair. The vacuum is filled with such virtual particles.

2.2 Quantum Chromodynamics

The theory of Quantum Chromodynamics (QCD) describes the strong interactions between quarks and gluons, the carriers of *color* charge, collectively termed *partons*. Color represents a degree of freedom and comes in three types, red, blue, or green, although only colorless combinations of partons are observed. This nomenclature is a metaphor that arises from the three primary colors of visible light which optically sum to white. Quarks, which may possess red, blue, or green color, form an $SU(3)$ triplet. Gluons, which carry one color and one anticolor, form an $SU(3)$ octet. A blue quark becomes a red quark by emitting a blue-antired gluon.

Color was first introduced to explain the existence of the Δ^{++}. Without the introduction of another degree of freedom, the Δ^{++} would be a system of three fermions existing in an overall symmetric state, $(u \uparrow u \uparrow u \uparrow)$, a violation of the Pauli exclusion principle. The overall wave function is made antisymmetric by requiring that each quark be of a different color and that the color wave function be antisymmetric. Although the colored quarks cannot be independently observed, the manifestations of color can be. For instance, if the π^o can exist in three different ways, as $r\bar{r}$, $b\bar{b}$, or $g\bar{g}$, the π^o decay to two photons should have a rate three times bigger than if there was no color degree of freedom. Experiment supports this.

2.2.1 Asymptotic Freedom and Color Confinement

The photon propagates the electromagnetic field but does not itself carry electric charge. The gluon, propagator of the color field, does carry color charge. One consequence of this is *asymptotic freedom* , the behavior of partons as quasi-free particles at high energy scales and small distances. Another is *color confinement*, the low energy, long

distance, behavior of the strong force which increases in strength as the partons separate. The color potential between the separating partons increases until production of another colorless parton system becomes the energetically favored state and a $q\bar{q}$ pair is produced. This process is called *hadronization*. Due to color confinement, quarks in mesons and baryons occur only in colorless combinations. In mesons the valance quark-antiquark pair possess equal and opposite color. In baryons the colors of the three valance quarks must optically sum to white, an $SU(3)$ singlet.

2.3 The Running Couplings $\alpha(Q^2)$ and $\alpha_s(Q^2)$

Virtual $e\bar{e}$ pairs created in the vacuum are polarized by an electron since it attracts the virtual positrons and repels the virtual electrons. The electron's *bare* charge is masked by the surrounding cloud of virtual positrons. As the cloud of positive charge is more deeply penetrated by a probe particle, i.e. as the momentum transferred in an interaction increases, the effective charge of the electron increases. This is quantitatively expressed in $\alpha(Q^2)$, the electromagnetic coupling strength, which increases with the momentum transfer Q.

The analogy in QCD is a quark surrounded by a sea of gluons and virtual $q\bar{q}$ pairs. However, as the cloud of surrounding color charge is penetrated more deeply, the strength of the strong interaction decreases. Thus α_s, the effective strength of the strong force, decreases with Q.

The running couplings for the electromagnetic and the strong forces emerge from the loop diagram in QED and QCD. A photon can exist as a virtual $e\bar{e}$ pair, a loop diagram with possibly infinite momentum, then reassemble as a photon within a time $\Delta t \approx \frac{\hbar}{\Delta E}$. The QCD analogue is the diagram of a gluon existing briefly as a $q\bar{q}$ pair.

In addition, gluons carry color charge. This results in the gluon self-coupling diagram of Fig. 2.1.

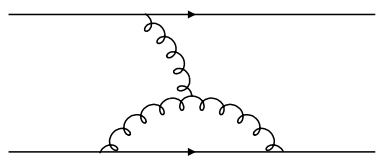

Figure 2.1: A gluon self coupling diagram. Gluons propagate the color field and they themselves carry color charge.

These diagrams lead to infinities in the calculation of the parton-level cross section. With renormalization, the infinities are absorbed into a redefinition of the coupling strength. In this process the calculated value of α_s becomes dependent on the renormalization scale μ_R which is often set equal to the momentum transfer, Q.

In QED the running coupling increases with Q^2,

$$\alpha(Q^2) = \frac{\alpha(\mu^2)}{1-(\alpha(\mu^2)/3\pi)ln(Q^2/\mu^2)}.$$

In QCD the running coupling decreases with Q^2,

$$\alpha_s(Q^2) = \frac{12\pi}{(33-2f)ln(Q^2/\Lambda^2_{QCD})}.$$

The $-2f$ factor, in which f represents the number of quark flavors, arises from the virtual $q\bar{q}$ pair diagram. The positive contribution, which results in asymptotic freedom, arises from the gluon self-coupling diagram.

The condition $Q^2 \gg \Lambda^2_{QCD}$ is required to probe the constituent quarks and gluons of the hadron as quasi-free partons. Λ_{QCD} sets the energy scale for which the system exists in this state rather than in a tightly bound state. Λ_{QCD} is not predicted by theory and must be determined empirically. It is roughly 200 MeV/c^2.

The strong coupling runs as shown in Fig. 2.2

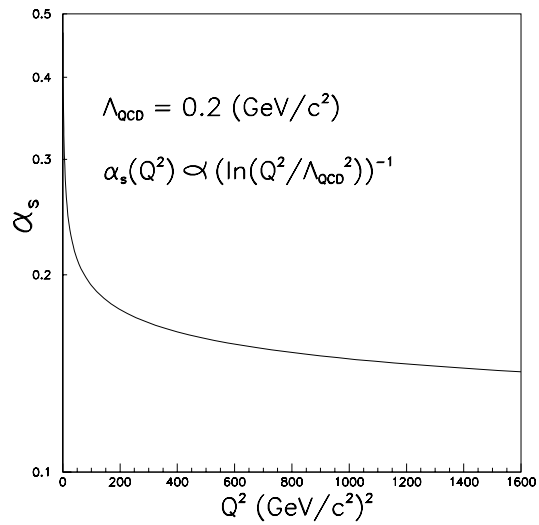

Figure 2.2: The strong force running coupling, $\alpha_s(Q^2)$.

2.4 Feynman Rules for Parton-Level Cross Section Calculation

Feynman established a set of rules used to calculate the cross section for parton-level processes. In a Feynman diagram, for instance Fig. 2.5, each of the incoming and outgoing lines, the internal propagator, and each vertex, represents a mathematical factor included in the calculation of the matrix element, $\mathcal{M}$, so that

$$\frac{d\hat{\sigma}(ab \to cd)}{d\hat{t}} = \frac{|\mathcal{M}^2|}{16\pi\hat{s}^2}.$$

For example, at each vertex a coupling strength, $\frac{g_s}{4\pi}$, is introduced. At an electromagnetic vertex this coupling is $\sqrt{\alpha}$; at a strong force vertex it is $\sqrt{\alpha_s}$. The symbols $\hat{s}$ and $\hat{t}$ used above are two of the three *Mandelstam variables*, $\hat{s} = (p_a + p_b)^2$, $\hat{t} = (p_a - p_c)^2$, and $\hat{u} = (p_a - p_d)^2$.

2.5 Parton Distributions

In the infinite momentum frame, each parton in the proton carries some fraction, x, of the proton's total momentum such that $p_{parton} = x P_{proton}$. The distribution of the proton's momentum among the constituent partons is characterized by a set of

parton distribution functions. In particular, $u_v(x)$ and $d_v(x)$ respectively represent the distribution in x of the valance u and d quarks in the proton.

It is required that

$$\int_0^1 u_v(x)dx = 2,$$

and

$$\int_0^1 d_v(x)dx = 1.$$

The total proton momentum equals the summed momenta of its constituents. The momentum distributions obey the momentum sum rule,

$$\int_0^1 x \sum(Q_v(x) + Q_{sea}(x) + G(x))dx = 1.$$

About half of the proton's momentum is carried by the valance quarks. The remainder is carried by the gluons and the sea quarks, i.e. the virtual $q\bar{q}$ pairs produced by the gluons.

The gluon distribution, $G(x)$, and the quark distribution, $Q(x)$, are shown in Fig. 2.3. The gluon distribution is *soft*, i.e. it is concentrated at low values of x, because gluons are massless and an unlimited number can be created from the available energy. A gluon distribution that approaches infinity as x approaches zero agrees well with deep inelastic scattering data.

2.6 Direct Photon Production

A photon that is not the decay product of a meson but emerges directly from the hard collision is termed a *direct photon.* The leading order (LO) processes for direct photon

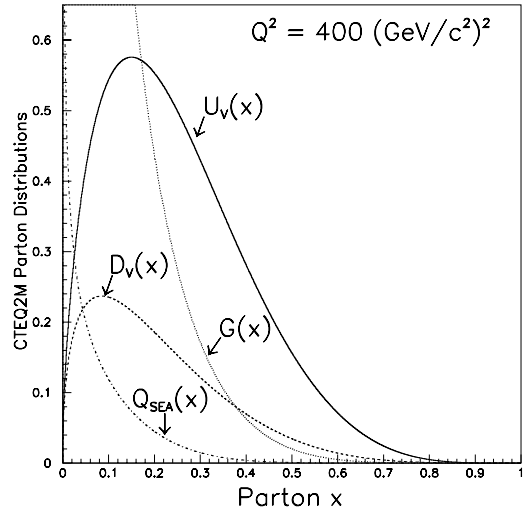

Figure 2.3: A comparison of parton distributions for the up valance quark, the down valance quark, the sea quarks and the gluons.

production are QCD Compton scattering where $gq \rightarrow \gamma q$ and $q\bar{q}$ annihilation where $q\bar{q} \rightarrow \gamma g$. The QCD Compton process involves a hard scattering between a quark and a gluon and provides a direct probe of $G(x)$.

The probability of $q\bar{q}$ annihilation is compared to the probability of the QCD Compton process for a given photon P_t in Fig. 2.4. At lower photon P_t, where $G(x)$ exceeds $Q(x)$, the QCD Compton process dominates. In this analysis the photon P_t is restricted to $16 < P_t < 40$ GeV/c.

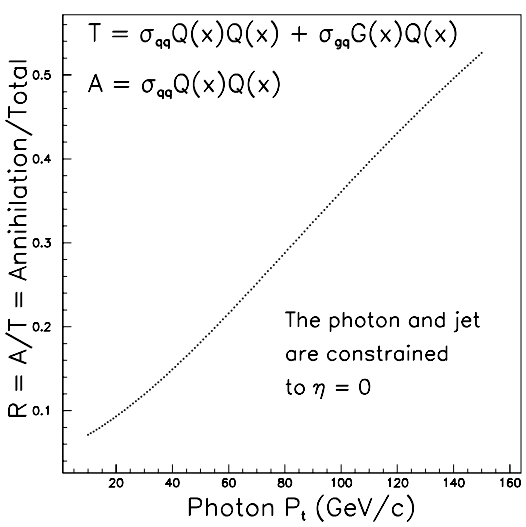

Figure 2.4: Of the total LO cross section, the fraction due to the annihilation process as a function of photon P_t.

Feynman diagrams for direct photon production are presented in Fig. 2.5. The direct photon leading order processes, written in terms of the Mandelstam variables, are:

QCD Compton,

$$\frac{d\hat{\sigma}}{d\hat{t}} = \frac{2}{\hat{s}}\frac{d\hat{\sigma}}{dcos\theta^*} = \pi\alpha\alpha_s e_q^2(-\frac{1}{3\hat{s}^2})(\frac{\hat{u}}{\hat{s}} + \frac{\hat{s}}{\hat{u}})$$

and $q\bar{q}$ Annihilation,

$$\frac{d\hat{\sigma}}{d\hat{t}} = \frac{2}{\hat{s}}\frac{d\hat{\sigma}}{dcos\theta^*} = \pi\alpha\alpha_s e_q^2(\frac{8}{9\hat{s}^2})(\frac{\hat{u}}{\hat{t}} + \frac{\hat{t}}{\hat{u}}).$$

Here, e_q is the electromagnetic charge of a quark.

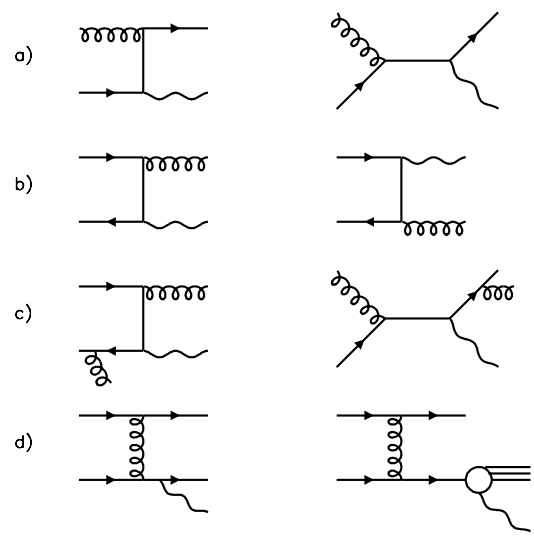

Figure 2.5: LO and NLO Feynman diagrams for direct photon production.

NLO diagrams are created by adding a strong force vertex to a LO diagram. This indicates the emission of a gluon. A soft gluon is included with the parent parton. This is identical to the LO, or $2 \rightarrow 2$, diagram. A hard gluon is not included with the parent

parton. This becomes a NLO, or $2 \rightarrow 3$, process. There are eight NLO diagrams for direct photon production. Two of these are shown in Fig. 2.5c.

The individual parton-level cross sections cannot be directly observed. Only the total hadronic cross section can be directly measured. In the calculation of the physically observed total cross section, there is one term for each parton-level diagram. Each term involves the relevant parton-level cross section convoluted with two parton distribution functions, one for each of the incoming partons.

$$\sigma_{tot} = \alpha\alpha_s \mathrm{G(x)Q(x)}\hat{\sigma}(\hat{u},\hat{s},\hat{t})_{gq\rightarrow\gamma q} + \alpha\alpha_s \mathrm{Q(x)}\bar{Q}\mathrm{(x)}\hat{\sigma}(\hat{u},\hat{s},\hat{t})_{q\bar{q}\rightarrow\gamma g} + \alpha\alpha_s^2 \mathrm{Q(x)}\bar{Q}\mathrm{(x)}\hat{\sigma}(\hat{u},\hat{s},\hat{t})_{q\bar{q}\rightarrow\gamma gg} + \ldots$$

Here, σ_{tot} is the experimentally measured total cross section. The calculated parton-level cross section, $\hat{\sigma}$, is proportional to the probability that two partons a and b, with momenta p_a and p_b, experience a hard collision resulting in two outgoing partons c and d, with momenta p_c and p_d. The parton distribution functions, $G(x)$ and $Q(x)$, represent, respectively, the distribution of gluons and quarks in the variable x, the fraction of the proton's momentum carried by the parton.

The number of parton-level diagrams that exist increases rapidly with the order in α_s of the subprocess. The order to which the total cross section is calculated is limited only by the strength of the theorist to calculate the required number of subprocesses.

The running of α_s, and in particular its smallness at large Q^2, makes the perturbative calculation possible. In the hard collisions that produce the direct photon events used in this analysis, $\alpha_s \approx 0.15$. If α_s was on the order of 1, the total cross section calculation would diverge as higher order terms were added.

2.6.1 The Underlying Event

Spectator partons uninvolved with the hard collision may experience soft collisions at large impact parameter. These soft collisions produce low energy particles, an *underlying event* uncorrelated with the products of the hard collision. Underlying event energy of roughly 2 GeV in a cone of radius $r(\eta, \phi) = (\Delta\eta^2 + \Delta\phi^2)^{1/2} = 0.7$ is distributed with uniform probability throughout the calorimeter. These soft interactions occur at low Q^2 and large values of α_s so they cannot be calculated using perturbation theory and are not well understood theoretically. In this analysis, experimental data taken with the CDF detector is used to account for these effects.

2.7 Momentum Scales Eliminate Singularities in the Cross Section Calculation

The calculation of the NLO cross section involves singularities that necessitate the use of momentum scales in the theory. One example is the ultraviolet (high Q^2) divergence which, as discussed above, is absorbed into the coupling strength with the introduction of the renormalization scale, μ_R. In addition to the ultraviolet cut-off μ_R, the scale μ_F is introduced to control the infrared (low Q^2) sensitivity of the calculation.

An infrared divergence results from the emission of a very low momentum gluon or a gluon that possesses momentum nearly collinear with that of the original parton. Suppose that a quark of momentum $\vec{p}$ emits a gluon of momentum $\vec{k}$ at an angle θ. The quark is left with momentum $\vec{p} - \vec{k}$. For this diagram, calculation of the parton-level cross section involves an integrand with the denominator $2|\vec{p}||\vec{k}|(1-cos\theta)$. This becomes infinite as the angle θ becomes small (collinear divergence) or as the momentum of the emitted gluon, $|\vec{k}|$, approaches zero (infrared divergence).

To control these infinities in the calculation the infrared sensitivity is absorbed into the distribution function. That is, all soft or collinear emissions are considered to be part of the original parton. This necessitates introduction of the factorization scale μ_F which, like μ_R, is often set equal to the momentum transfer, Q. An emitted gluon with momentum $k < \mu_F$ is included with the original parton. Above this momentum the gluon is not included with the original parton, it becomes an additional final state parton. Now the parton distribution function, $\phi(x)$, becomes $\phi(x, \mu_F) \equiv \phi(x, Q)$.

Various *factorization methods* can be used to determine the scale, μ_F. Appendix A elaborates on this.

2.8 Q^2 Evolution of Parton Distributions

The proton is a complex system of three valance quarks amidst a sea of gluons and *sea quarks*, the virtual $q\bar{q}$ pairs produced by the gluons. This system can be studied by measuring the energies and momenta of particles produced in $p\bar{p}$ collisions at high energies, where the partons are asymptotically free.

Through the uncertainty principle, an interaction with momentum transfer, Q, resolves structure on a distance scale (impact parameter) $\Delta x \approx \frac{\hbar}{Q}$. Interactions with large momentum transfer involve phenomena that occur on small length and time scales. Figure 2.6 shows the Feynman diagram for gluon exchange between partons in a $p\bar{p}$ collision.

An incident particle supplying momentum transfer, Q, cannot resolve a gluon radiated and reabsorbed by a quark within $\Delta t < \hbar/Q$. If Q increases and Δt becomes comparable to the time interval during which the radiated gluon exists before reabsorption, the gluon is resolved. As Q^2 increases further, the sea quarks, produced by the

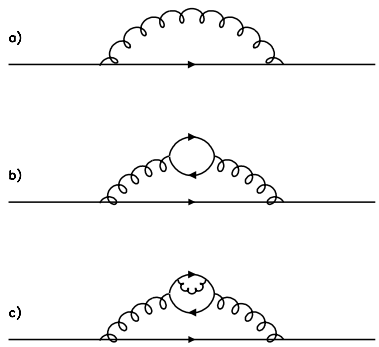

Figure 2.6: A probe of higher Q^2 resolves structure on a smaller scale.

radiated gluons, are resolved. Next, gluons radiated by the sea quarks are resolved. With higher Q^2, partons of greater virtuality, i.e. farther off-mass-shell, are resolved. Figure 2.7 shows the CTEQ2M parton distributions [12] for different values of Q^2. The Altarelli-Parisi evolution equations [2] *evolve* parton distributions from one value of $\mu_F^2 = Q^2$ to other values.

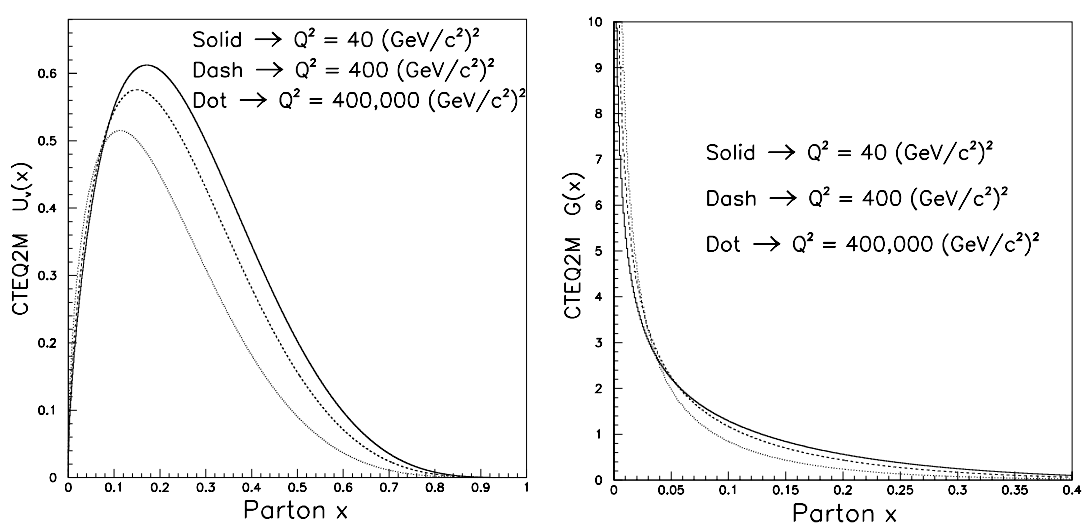

Figure 2.7: The Q^2 evolution of the CTEQ2M parton distributions **a)** $U_v(x)$ and **b)** $G(x)$.

2.9 Extraction of Parton Distributions from Experimental Data

The parton distribution functions are extracted from an experimentally measured total cross section together with a perturbative calculation, to some order in α_s, of the parton-level cross sections involved in the process. The measured total cross section is expressed as,

$$\sigma_{tot} = \alpha\alpha_s \mathrm{G(x)Q(x)}\hat{\sigma}(\hat{u},\hat{s},\hat{t})_{gq\to\gamma q} + \alpha\alpha_s \mathrm{Q(x)}\bar{Q}\mathrm{(x)}\hat{\sigma}(\hat{u},\hat{s},\hat{t})_{q\bar{q}\to\gamma g} \ldots + \mathrm{NLO}$$

Parton distribution functions are universal, i.e. process independent. They can be extracted from deep inelastic scattering, Drell-Yan, or direct photon processes with consistent results. The nontrivial proof of this is called the *factorization theorem.* This property is essential to the process of global fitting, where data from different experiments are combined to extract parton distribution functions.

In global fitting, a form is assumed for the distribution function and the parameters of this form are varied until all the available data are fit within some value of χ^2. Many different parameterizations exist. The CTEQ2 parton distributions take the form [13], $x\phi(x,\mu_F) = A_o x^{A_1}(1-x)^{A_2}(1+A_3 x^{A_4})$. The parameter A_1 governs the low x behavior. CTEQ2M represents the best fit in the $\overline{MS}$ factorization scheme [12] and has $A_1 = -.258$ in xG(x). CTEQ2MF has $A_1 = 0.0$ in xG(x) and the remaining parameters are adjusted to accommodate this. In CTEQ2ML Λ_{QCD} is set to the LEP value and $A_1 = -.212$ in xG(x). See Tab. 2.2. MRSD0 [14] has a similar form with $A_1 = 0.0$ in xG(x).

The parton distributions listed in Tab. 2.2 are NLO. Recall that the parton-level cross sections are calculated to some order in α_s and the extracted parton distribution function is valid only up to this order.

Table 2.2: The parton distribution sets used in this analysis and the corresponding Λ_{QCD} for four flavors are presented here. All of these sets use the $\overline{MS}$ factorization scheme.

Parton Distribution Set	$\Lambda^{(4)}_{QCD}$ (MeV/c^2)
CTEQ2M	213
CTEQ2ML	322
CTEQ2MF	208
MRSD0	215

Λ_{QCD} appears in α_s as $\alpha_s \approx 1/ln(\frac{Q^2}{\Lambda^2_{QCD}})$. The extracted parton distribution function is valid only for a specific value of Λ_{QCD}. Λ_{QCD} determines the rate at which α_s runs with Q^2 and, consequently, the rate at which the parton distribution function evolves with Q^2. As Λ_{QCD} decreases, the Q^2 evolution rate increases.

The measured cross section accesses some range of parton x. The extracted parton distribution function is reliable only within this range. The x range accessible to this measurement is discussed in the next section.

2.10 Partonic Fragmentation and Hadronization to Produce Jets

The final state external quark or gluon appears in the detector as a collimated jet of particles. As the struck parton pulls away from neighbor partons, the potential energy of the strong force between them increases linearly with the separation distance. Eventually hadronization occurs and some number of colorless objects (baryons and mesons) with momenta in the general direction of the original parton are created.

2.10.1 The Effect of Soft Gluon Radiation on Photon + 1 Jet Event Topology

Partons constantly radiate soft gluons. A hard collision, one with large momentum transfer and small impact parameter, results in a more strongly collimated jet than does a soft collision. In a hard collision the influence of gluon radiation on the momenta of the final hadronized particles is overwhelmed by the large final momentum of the struck parton and the particles emerge in a strongly collimated jet. In a soft collision such gluon radiation does exert an influence and the particles emerge with a wide spatial distribution.

Soft gluon radiation introduces a small random transverse momentum, or K_t, that accompanies the large longitudinal momentum of the colliding partons. The neighboring partons that become involved in the hadronization process also possess K_t. K_t of the initial or final state partons sometimes causes the outgoing products of a $2 \rightarrow 2$ interaction to not emerge back-to-back in ϕ. This results in spreading of the $\Delta\phi = \phi_\gamma - \phi_{jet}$ distribution around the central value of 180°. See Fig. 2.8.

2.11 Using Photon + Jet Kinematics to Select Events in Regions of Specific Parton x

The momentum fractions, x_a and x_b, of the incident partons, a and b respectively, are calculated on an event-by-event basis with the following equation.

$$x_{a,b} = \frac{P_t}{\sqrt{s}}(e^{\pm\eta_\gamma} + e^{\pm\eta_{jet}})$$

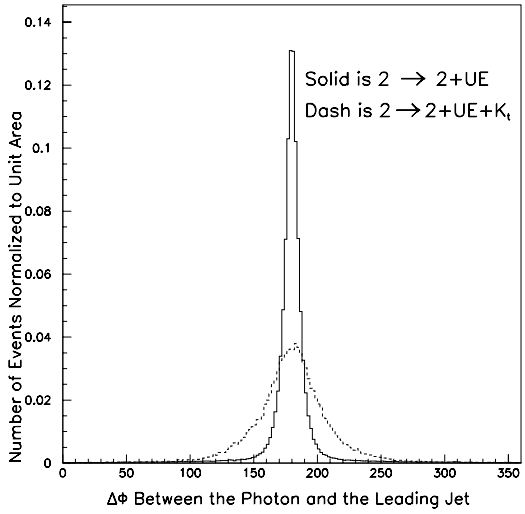

Figure 2.8: The $\Delta\phi$ between the photon and the lead jet in generated $2 \rightarrow 2$+UE events and $2 \rightarrow 2$+UE+K_t events.

For particles of negligible mass, the *rapidity*, or $y = \frac{1}{2}ln(\frac{E+P_z}{E-P_z})$, becomes equivalent to the pseudorapidity, $\eta = \frac{1}{2}ln(\frac{P+P_z}{P-P_z}) = -ln(tan(\theta/2))$. *Detector* η is measured from $z = 0$ and is written here as η_D. *Event* η, is measured from the z position of the hard scattering event and is written here simply as η.

η is a useful coordinate in $p\bar{p}$ collisions where the motion of the quarks and gluons within the proton is varied and the relative motion of the colliding partons differs in each event. The value of η in one reference frame differs by a constant from that in a Lorentz boosted frame; $d\eta$ is thus Lorentz invariant. A measurement of the invariant differential cross section can be given in terms of dP_t and $d\eta$.

In this analysis, the photon is constrained to the central region, $|\eta_\gamma| < 0.9$, where the CDF calorimeters are of highest quality. For the hadron jet, all calorimeters are used so that $|\eta_{jet}| < 4.0$. Thus, the accessible range of parton x is governed by the η coordinate of the lead, i.e. highest E_t, jet. The measurement of the lead jet η distribution probes $0.015 < x < 0.15$ as demonstrated in Fig. 2.9.

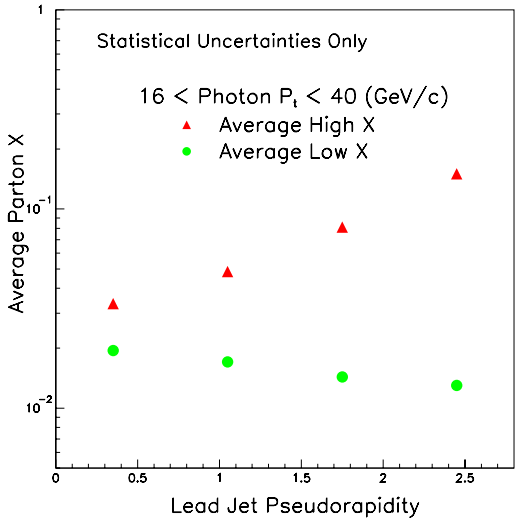

Figure 2.9: The range of parton x probed by the lead jet η distribution.

The ideal kinematic variable for discrimination among parton distributions separates the events by their parton x values and, in particular, isolates events with the highest and lowest accessible x values. In Fig. 2.9, the average high x value, (x_a if $x_a > x_b$), and the average low x value, (x_b if $x_a > x_b$), in the data is shown in terms of the lead jet η. Events in which one of the two initial state partons reaches the lowest attainable x value and the other reaches the highest attainable x value occupy the high η region.

Other kinematic variables were considered. The parton x distribution is related directly to the direct photon P_t distribution as demonstrated by the above equations. The direct photon P_t distribution has been measured for CDF [25], and is presented in Fig. 4.3. The shape difference between the measured and theoretical direct photon P_t spectra in the low P_t region may be due to the effects of K_t. The data used in the present analysis are required to have photon $16 < P_t < 40$ GeV/c. As discussed in Appendix E, the photon and lead jet are also required to be back-to-back in ϕ within $\Delta\phi \pm 30^o$ to select events of limited K_t with correctly identified lead jets. Figure 2.10 shows that the average photon P_t in these data depends little on the lead jet η. Thus, the lead jet η distribution provides an independent test of parton distributions that is insensitive to

K_t. Other variables considered were $\eta_{BOOST} = (\eta_{JET} + \eta_\gamma)/2$ and $\eta^* = (\eta_{JET} - \eta_\gamma)/2$ which extend the available x range by including the photon η. However, they provide insufficient data in the high-η region to correct the measurement for detector effects [11].

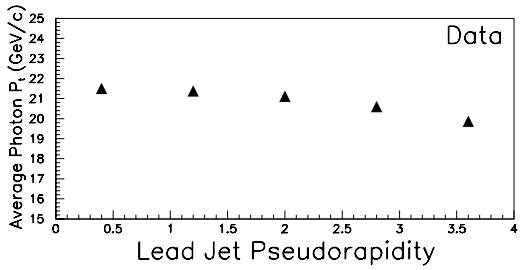

Figure 2.10: The average photon P_t exhibits little dependence on lead jet η.

2.12 The Multiple Photon Background

Background to the direct photon signal arises from mesons that decay to multiple photons, in particular, $\pi^o \rightarrow \gamma\gamma$. Mesons are created in jets. Dijet production is an α_s^2 process in leading order. See Fig. 2.11. The number of diagrams for jet production exceeds that for direct photon production. Jet production occurs roughly 10^3 times more frequently than direct photon production.

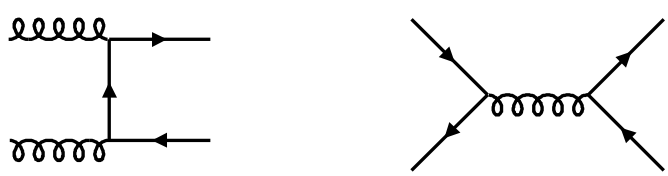

Figure 2.11: Examples of Feynman diagrams for dijet production.

A photon accompanied by any other particle within a certain region of surrounding space is rejected from the data sample. This *isolation* requirement greatly reduces the

meson background to the direct photon signal.

The direct photon signal in the data becomes enhanced as the photon P_t increases. This is an effect of the isolation cut, the fragmentation process, the jet production cross section, and the running coupling α_s.

The isolation requirement becomes more strict as the photon E_t increases. Photons are rejected from the data sample if the accompanying E_t in the surrounding $\eta - \phi$ cone exceeds the *fixed* value of 2 GeV. A jet of $E_t = 10$ GeV that includes one π^o with E_t of 8 GeV is far more common than a jet of $E_t = 100$ GeV that includes one π^o with E_t of 98 GeV.

Fragmentation functions are used to determine the relative population of different particles within a jet as a function of the fractional momentum carried by those particles. The fragmentation function, $D_{\pi q}(z, Q^2)$, expresses the probability that fragmentation and hadronization of a quark, q, will yield a π^o possessing the momentum fraction $z = \frac{p_\pi}{p_q}$. It can be parameterized as $D_{\pi q}(z, Q^2) = C_1 \frac{(1-z)^{C_2}}{z}$ where C_1 and C_2 are constants. It is rare that a high energy quark satisfies $z \rightarrow 1$ and fragments almost entirely into one π^o.

As the photon E_t increases, the jet E_t required to produce a meson that decays to that photon also increases. The higher the photon E_t, the more rare the required jet since the jet production cross section is a steeply falling function of jet E_t.

The running of α_s provides a less important contribution to this effect. α_s decreases as both Q^2 and the photon E_t increase. There is a corresponding decrease in jet production relative to direct photon production.

The ratio of direct photon events to multiple photon events as a function of photon

P_t is shown in Fig. 2.12.

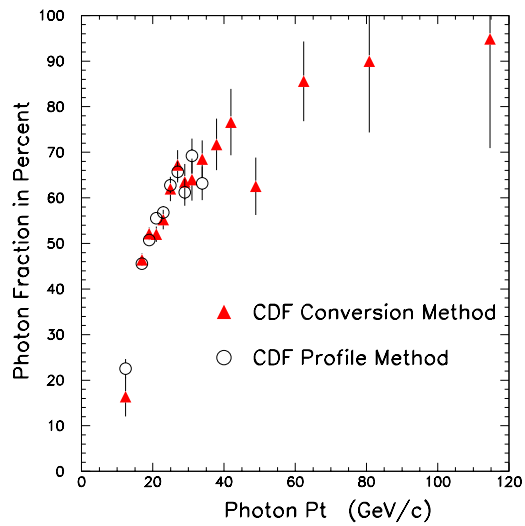

Figure 2.12: The ratio of direct photon events to multiple photon events increases with photon P_t.

2.13 Next-to-Leading-Order Calculation of the Direct Photon Cross Section

The NLO calculation of direct photon production [9] accounts for all diagrams of order $\alpha\alpha_s$ and $\alpha\alpha_s^2$. In addition, it includes LO fragmentation. It also accounts for the isolation requirement.

The soft gluon radiation responsible for K_t occurs in a low energy, non-perturbative kinematic regime and so is not included in the NLO calculation.

The data are corrected using simulated events generated with a set of code independent of the NLO calculation to which the final measurement is compared. The events are generated with PAPAGENO which uses the parton-level matrix elements to generate the hard collision. SETPRT uses ISAJET [18] routines to perform the subsequent fragmentation of partons and produces a list of final state hadrons and their momenta. In addition, this routine models the underlying event and the effect of K_t. It is tuned

on the data of the 1988-1989 run. In dijet events, the energy deposited transverse to the axis defined by the two jets provides an estimate of the underlying event energy. Likewise, the effect of K_t on the kinematics of outgoing particles is modeled using dijet events. Finally, the standard CDF detector simulation QFL simulates the response of the CDF detector to the hadrons in this list.

Chapter 3

Accelerator and Detector

This chapter describes the experimental apparatus. It begins with an overview of the Fermilab accelerator. Appendix B details the techniques used to maintain beam stability, enhance beam luminosity, produce the p and $\bar{p}$ beams, and collide these beams at the B0 interaction point. CDF is a collection of many detectors each designed to measure specific aspects of the hard scattering event. The Central Tracking Chamber discriminates photons from electrons. The Central Preradiator and the Central Electromagnetic Strip Chamber distinguish, on a statistical basis, direct photons from the multiple photon background. The Central Electromagnetic Calorimeter records the photon energy. All calorimeters, both electromagnetic and hadronic, record jet energy and together cover $|\eta_D| < 4.0$. This measurement is corrected for the three regions in η_D where different detectors meet and the jet energy resolution, and hence the jet η resolution, is diminished. A three tiered trigger rejects uninteresting events and records hard scattering events that satisfy certain criteria.

In the 1992-1993 collider Run 1A of the Tevatron six bunches of protons and six bunches of antiprotons circulated in opposite directions at 900 GeV around the 6.28 km circumference of the Tevatron ring. See Fig. 3.1. The superconducting dipole and quadrupole magnets of the Tevatron respectively bent and focused both particle beams. At the B0 interaction point the counter-rotating beams collided with a center-of-mass

energy of 1.8 TeV at the center of the CDF detector.

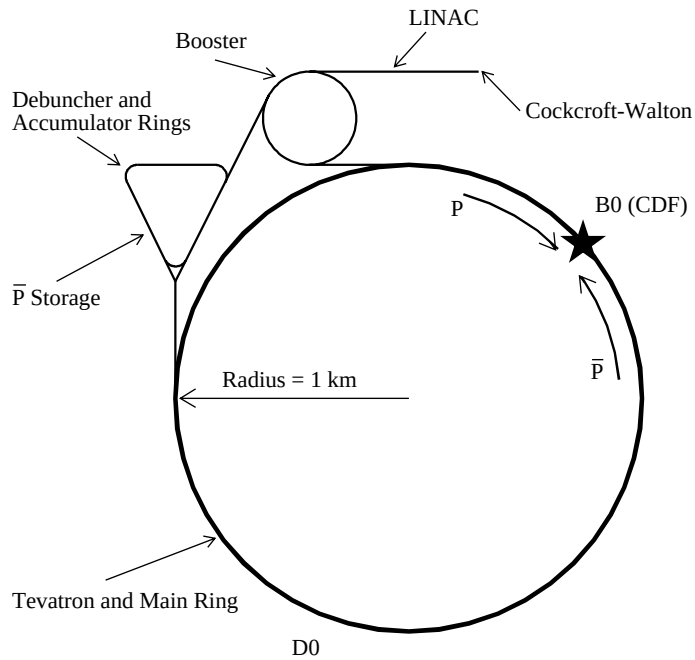

Figure 3.1: A schematic of the Fermilab $p\bar{p}$ accelerator.

The number of hard scattering interactions between partons, N_i, is governed by the relation,

$$N_i = \sigma_{p\bar{p}} L,$$

where $\sigma_{p\bar{p}}$ is the cross section and L is the beam luminosity. To maximize N_i, the luminosity,

$$L = \frac{N_p N_{\bar{p}} R_C}{4\pi\sigma^2},$$

is made as large as possible. Here N_p is the number of protons in the bunch, $N_{\bar{p}}$ is the number of antiprotons, R_C is the rate at which the proton and antiproton bunches cross and σ represents the r.m.s. width of the beam transverse to the direction of motion.

In Run 1A, the beam crossings occurred every 3.5 μs. The average number of protons in a bunch was about 1.5×10^{11} and the average number of antiprotons was about 0.5×10^{11}. The quadrupole magnets immediately preceding the B0 detector hall focused the beams to within $\sigma = 0.04$ mm transverse diameter at the interaction point. An average luminosity of 3.16 X 10^{30} cm^{-2}s^{-1} was delivered in Run 1A. Details of $p\bar{p}$ beam production are given in Appendix B.

3.1 The CDF Detector

The coordinates generally used with the CDF detector are the direction of the proton beam z, the azimuthal angle ϕ, and the pseudorapidity $\eta = -ln(tan(\theta/2))$ where θ is the polar angle. As previously described, two definitions are used for η. *Detector* η is measured from $z = 0$ and is written here as η_D. *Event* η, is measured from the z position of the hard scattering event and is written here simply as η. The detector is generally described as having a central region with $|\eta_D| < 1.1$, a plug region with $1.1 < |\eta_D| < 2.3$, and a forward region with $|\eta_D| > 2.3$. The detectors covering each region are described below.

Alternatively, a right-handed coordinate system with positive z along the proton beam direction, positive y directed upward, and positive x directed outward from the center of the Tevatron, is sometimes used. The detector has approximate cylindrical symmetry. A schematic is shown in Fig. 3.2. A cross section through one quarter of the detector in the $y - z$ plane, with the interaction point located at the lower right hand corner, is shown in Fig. 3.3.

A particle that emerges from the interaction point in the vicinity of $\eta_D = 0$, has a trajectory that passes first through the silicon vertex detector, then through the tracking

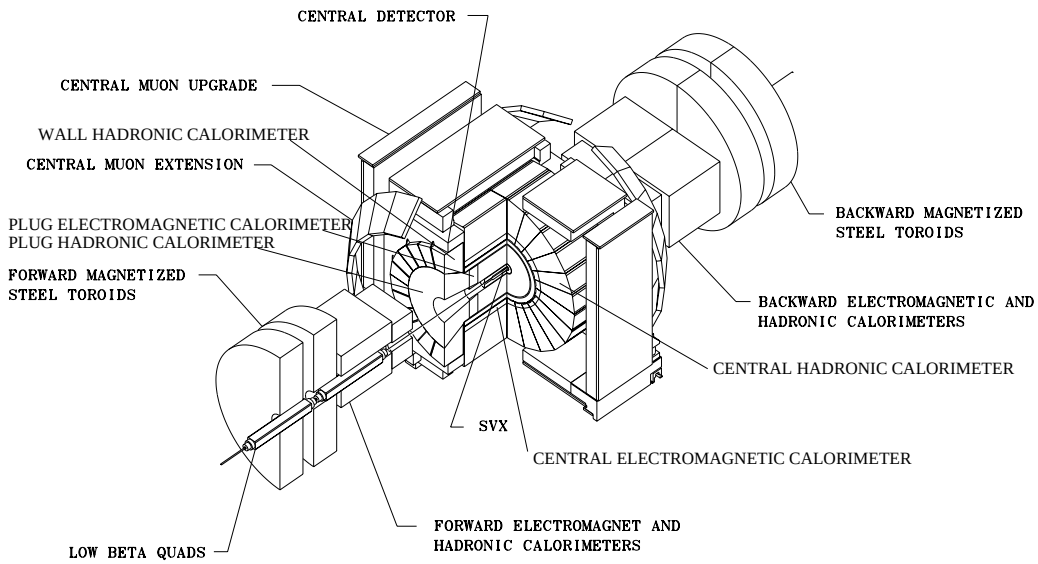

Figure 3.2: A schematic of the CDF detector.

detectors and the surrounding solenoid. Next it encounters the central preradiator then the electromagnetic and hadronic calorimeters and last the muon chambers. As the CDF detector is described in detail elsewhere [20], only the components relevant to this analysis will be discussed here.

3.1.1 The Central Tracking Chamber

The Central Tracking Chamber (CTC) is a cylindrical drift chamber which encircles the beam pipe and covers a region $|\eta_D| < 1.0$. The inner radius extends 28 cm from the beam pipe. The outer radius is 1.3 m. The superconducting solenoid, which surrounds the CTC, generates a 1.5 T magnetic field. A charged particle passes through the CTC with a helical trajectory marked by a trail of electrons ionized from the argon-ethane gas. The particle momentum is determined from the curvature of the track and is

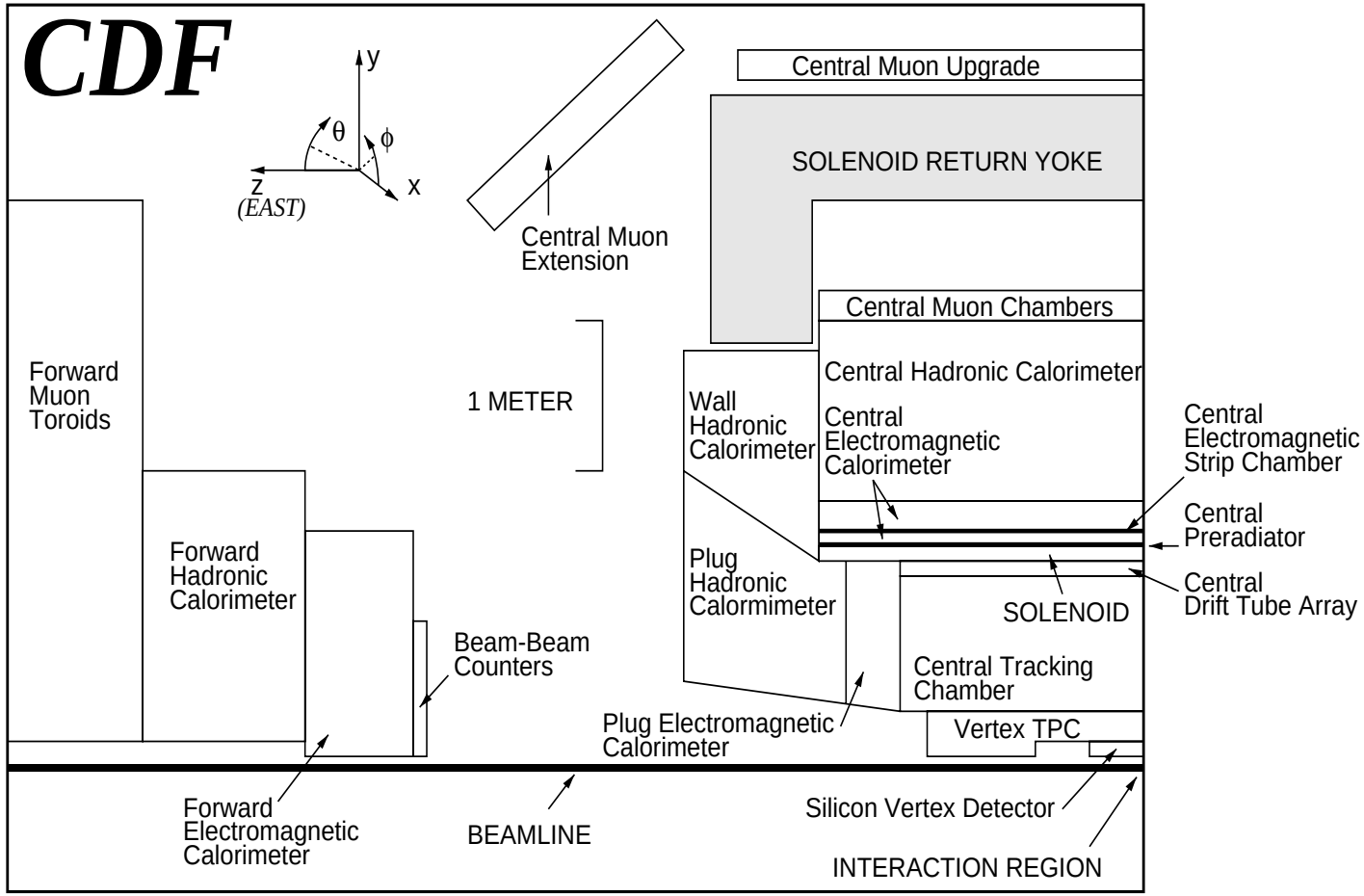

Figure 3.3: A cross section of the CDF detector.

measured within a resolution of $\delta P_t/P_t^2 \leq 0.002$ (GeV/c)$^{-1}$.

The drift field of the CTC is $\approx$ 1350 V/cm. The ionized electrons reach a nearby sense wire within a drift time of 800 ns. This corresponds to a maximum distance of 40 mm. The spatial position of the passing charged particle is determined using 1) the position of the sense wire and 2) the distance corresponding to the drift time of the ionized electrons. An algorithm reconstructs the trajectory using the sequence of measured charged particle positions. Photons are distinguished from electrons using the CTC because only the charged electron leaves a track.

The sense wires are arranged in 84 layers that are in turn grouped into nine super-layers. See Fig. 3.4. In the five *axial* super-layers, 12 sense wires are oriented parallel to the z axis within each drift cell. The six sense wires in the drift cells of the four *stereo* super-layers are tilted $\pm 3^o$ with respect to the z axis. The axial super-layers provide a measurement of the $r - \phi$ position and are alternated with the stereo super-layers which, together with the axial layers, provide $r - z$ information.

The CTC drift cells are tilted at 45° with respect to the radial direction. This compensates for the radial component of the Lorentz force so the net force on the drift electrons is azimuthal when the solenoidal magnetic field is 1.5 T. This maintains the linearity of the time-to-distance relationship.

The ionized electrons may approach the sense wire from the right or the left. No information is recorded that distinguishes the two directions. The 45° tilt of the drift cells eliminates this ambiguity since the true reconstructed trajectory originates from the event vertex and the fake trajectory does not.

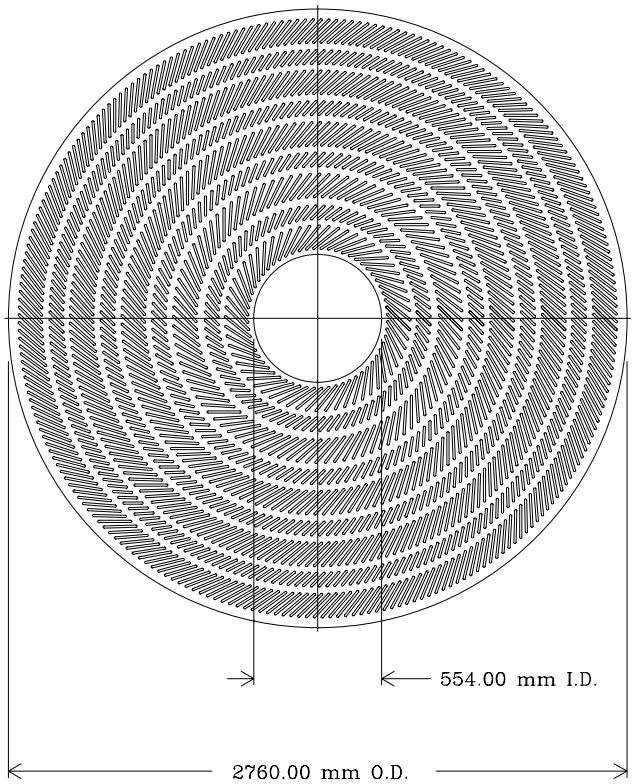

Figure 3.4: An end view of the Central Tracking Chamber.

3.1.2 The Central Drift Tube Array

The Central Drift Tube (CDT) detector immediately surrounds the CTC at a radius of 1.4 m. It is a three layer deep array of 3 m long stainless steel tubes each 1.27 cm in diameter. Each tube contains a sense wire and is oriented parallel to the beam pipe. The amplitude of the electromagnetic pulse measured on either end of the sense wire determines the z coordinate. The ϕ coordinate is first given by the azimuthal position of the tube then more precisely determined by measurement of the drift time required for ionized electrons to reach the sense wire.

3.1.3 The Central Preradiator

The Central Preradiator (CPR) [25] is a multiwire proportional drift chamber positioned outside the solenoid at 168 cm from the interaction point. It records the photon conversions, $\gamma \rightarrow e^+e^-$ in the nuclear Coulomb field, that take place in the 1.075 radiation lengths, or 1.075 L_{RAD}, of intervening material. (One L_{RAD} of a material is that distance over which, entirely through radiation loss, the average energy of an electron beam decreases by the factor $1/e$.) This distance corresponds to a 60% conversion rate for direct photons and an 84% conversion rate for the multiple photon background. Each chamber of the CPR has 32 sense wires ganged in pairs. The sense wires are held at a positive voltage of 1790 V. The nearly rectangular cells are $\approx$ 2 cm wide in the azimuthal and radial directions. The chamber is filled with argon-CO_2 gas.

3.1.4 The Central Calorimeter

The central calorimeter is a collection of 480 calorimeter *towers* . Each tower is segmented in the radial direction and has first an electromagnetic calorimeter then a

hadronic calorimeter. A proportional drift chamber is positioned within the electromagnetic calorimeter to enhance the spatial resolution. The towers have a projective geometry, i.e. each projects back toward the interaction point along a line of constant η_D.

Each tower extends 15° in ϕ and ≈ 0.1 units in η_D. Ten calorimeter towers, consecutive in η, combine to form a *wedge*. These towers form one of the 24 ϕ sections that combine to encircle the beam pipe. Two such calorimeter rings face each other, one on either side of the interaction point. Together they cover the region $|\eta_D| < 1.1$.

3.1.5 The Central Electromagnetic Calorimeter

The Central Electromagnetic Calorimeter (CEM) consists of 31 layers of 3.2 mm-thick lead interleaved with layers of 5 mm-thick scintillator. The full depth is $\approx 18\ L_{RAD}$. The high Z value of the lead nuclei promotes electromagnetic showering of photons and electrons. The energy in the shower excites the scintillator atoms which radiate light when they return to the ground state. The amount of light generated in the scintillator is proportional to the energy of the primary e^- or γ. Waveshifters change the primarily UV/blue scintillator light to green. Lightguides carry the wave-shifted scintillator light to the two phototubes in each CEM tower, one on either side in ϕ, which convert the light to a current pulse. The phototube response is optimized to green light. The energy weighted average of the signal from the two phototubes determines the azimuthal position of the electromagnetic shower. See Fig. 3.5. The CEM has a resolution of $13.5\%/\sqrt{E} + 1.7\%$.

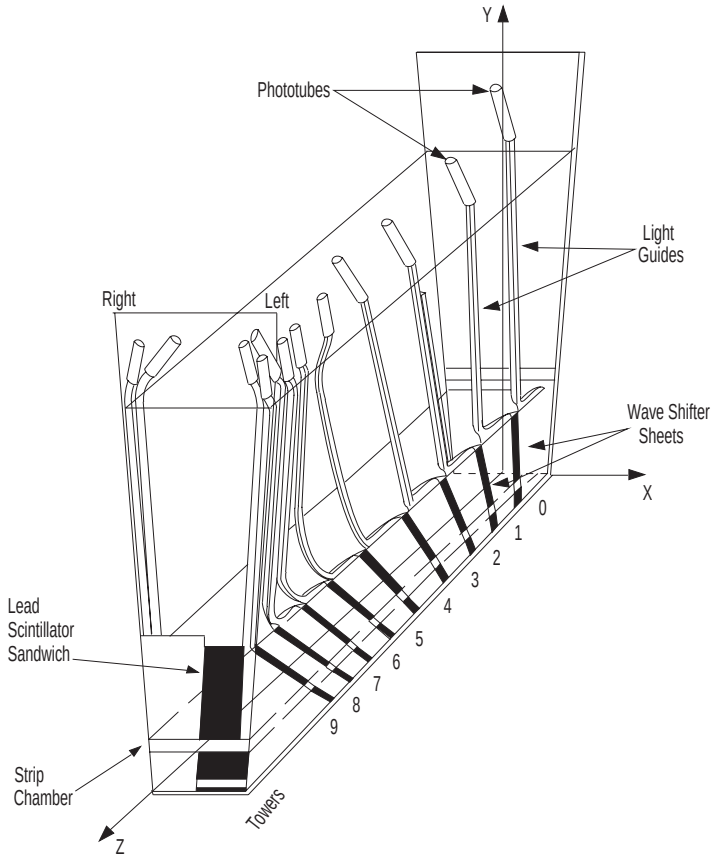

Figure 3.5: A schematic drawing of one wedge in the Central Electromagnetic Calorimeter.

3.1.6 The Central Electromagnetic Strip Chamber

The Central Electromagnetic Strip Chamber (CES) is located within the CEM at a depth of 5.9 L_{RAD}. This distance is approximately equivalent to *shower maximum*, the distance at which the greatest amount of the initial photon or electron energy is expended in the shower.

The CES is a proportional drift chamber used to measure the transverse profile of the electromagnetic shower. This information allows statistical separation between the characteristically broad transverse profile of the multiple photon background and the characteristically narrow transverse profile of the direct photon signal. The 128 strips function as cathodes and lie perpendicular to the 64 anode wires. The latter are set 2 mm apart and held at a potential of 1420 V. The energy independent spatial resolution is 2 mm $\times$ 2 mm and corresponds to the wire spacing of the drift chamber. The window used to measure the shower transverse profile is 11 strips, or 15 cm, wide. The minimum separation of two photons produced in the symmetric decay of a π^o, each photon of transverse momentum P_t, is $(50\text{ cm} - \frac{\text{GeV}}{c})/P_t$ at the position of the CES.

3.1.7 The Central and End Wall Hadronic Calorimeters

The Central Hadronic Calorimeter (CHA) spans $|\eta_D| \leq 0.9$ and consists of 32 steel layers of 2.5 cm thickness interleaved with sheets of 1.0 cm-thick plastic scintillator. The total depth is 4.7 interaction lengths, or 4.7 L_{INT}. (Of N neutral particles that traverse one L_{INT} of a material, all but N/e experience an interaction with the nuclei of the material.) The End Wall Hadronic Calorimeter (WHA) covers $0.7 \leq |\eta_D| \leq 1.3$. A total depth of 4.5 L_{INT} is presented by 15 layers of 5 cm-thick steel interleaved with 1 cm-thick scintillator. Towers in the intermediate region, $0.7 < |\eta_D| < 0.9$, are shared

by the two detectors so that a particle emerging from the interaction point along a path of constant η_D first encounters the CHA and next the WHA.

The charged decay products produced in the collision of particles with the steel nuclei excite the atoms of the scintillator material. The electromagnetic radiation consequently emitted by these atoms is converted to a measurement of the incident particle energy as previously described for the CEM. The energy resolution of the CHA is $80\%/\sqrt{E} + 3.0\%$.

The CHA is used to measure the hadronic energy in jets and, together with the CEM, to determine the ratio of electromagnetic to hadronic energy deposited by passing particles. This ratio is used in the identification of photon candidates.

3.1.8 Calibration of the Scintillator Based Calorimeters

Calorimeters that use plastic scintillator as the active medium were first calibrated in a test stand with radioactive sources and cosmic rays, then in a test beam. Electrons of 50 GeV were used to test the electromagnetic calorimeter response and charged pions of 50 GeV were used to calibrate the hadronic calorimeter.

In both the electromagnetic and hadronic calorimeters, long term variations in gain were monitored by using ^{137}Cs sources to expose the scintillator to γ-rays. For the electromagnetic calorimeter, short term variations were monitored by a Xenon flasher system that tested the response of the waveshifter to light. In addition, a light-emitting diode system was used to inject green light into the phototube. The hadronic calorimeter calibration system employed a Nitrogen laser to inject light into the phototubes. Quartz fibers connected all light flasher systems to the appropriate detector component.

3.1.9 The End Plug Electromagnetic Calorimeter

The End Plug Electromagnetic gas calorimeter (PEM) consists of conductive plastic drift tubes of square cross section strung with gold-plated tungsten wire and arranged in layers perpendicular to the beam line. The PEM is composed of four azimuthal quadrants that together encircle the beam pipe and cover $1.1 < |\eta_D| < 2.4$ in a projective geometry.

Each drift tube layer is arranged by placing tubes parallel to and along side of each other. The length of each tube is adjusted to obtain a fan shaped plane extending radially to an outer diameter of 3 m and occupying 90° in azimuth. The inner diameter of each layer is adjusted so that, with all layers taken together, the PEM leaves an empty cone of opening angle 10° from the beam axis. The opening angle is measured from the interaction point.

There are 34 proportional tube arrays interleaved with 2.7 mm-thick layers of lead. Argon-ethane gas is used as the active medium. The PEM occupies a depth of 50 cm in z which corresponds to about 19 L_{RAD}.

Each array of drift tubes is bordered on either side by a panel of G-10. One panel is used for a ground plane. The copper plating on the other panel is etched in a pattern of radial lines and concentric arcs to form the cathode pad segmentation of 5° in ϕ and 0.09 in η_D.

Longitudinal segmentation into three sections is accomplished by summing over the signals from each pad segment of $\Delta\phi$ and $\Delta\eta_D$ in each of a set of layers. Signals are summed from the first five layers encountered along a line of constant η_D from the interaction point, then from the next twenty-four, and finally from the last five. The central longitudinal segment is larger in order to contain most of the electromagnetic

shower energy.

The pad segmentation is useful for energy measurement. The energy resolution is $28\%/\sqrt{E}+2.0\%$. Strips yield a superior position measurement. Enhanced spatial resolution is required for the first ten layers of the second longitudinal segment since these are positioned around the shower maximum. For these layers the pad segmentation is not used. Instead, strips of concentric arcs are etched in the copper coating of the cathode G-10 boards to measure η_D and strips extending radially are used to measure ϕ. The spatial resolution is 0.2×0.2 cm.

3.1.10 The End Plug Hadronic Calorimeter

The End Plug Hadronic Calorimeter (PHA) covers $1.32 < |\eta_D| < 2.4$ and is of similar construction to the PEM. It has 20 steel layers of 5 cm thickness interleaved with the previously described drift tube layers. The total depth represents 5.7 L_{INT}. The cathode pads have the same segmentation in ϕ and η_D as in the PEM. The energy resolution is $130\%/\sqrt{E}+4.0\%$. There are two longitudinal segments, the first is based on a sum over the first 10 layers and the second results from a sum over the last 10 layers.

3.1.11 The Forward Electromagnetic Calorimeter

The forward calorimeters are located roughly 6.5 m from the interaction point. The Forward Electromagnetic Calorimeter (FEM) covers $2.2 \leq |\eta_D| \leq 4.2$ in a projective geometry. It has 30 layers of lead alternating with drift chambers. This represents a total depth of 25.5 L_{RAD}.

The drift chambers were made from aluminum extruded to form an array of parallel

channels each of transverse dimension 1.0 cm $\times$ 1.5 cm. Each channel was strung with a gold-plated tungsten wire. The cathode pad segmentation on the copper-plated circuit board facing the chamber is 5° in ϕ and 0.1 in η_D. The energy resolution is $25\%/\sqrt{E} + 2.0\%$.

There are two longitudinal segments. The first is formed by summing pad signals from the first 15 layers and the second by summing over the last 15 layers.

As the position of the shower varies in the calorimeter, the strip layers yield a spatial resolution that ranges from 0.1 cm to 0.4 cm.

3.1.12 The Forward Hadronic Calorimeter

The Forward Hadronic Calorimeter (FHA) covers $2.2 \leq |\eta_D| \leq 4.2$ and has 27 layers of 5 cm-thick steel alternating with the drift tube arrays. The total depth represents 7.7 L_{INT}. The cathode pad segmentation is the same as it is for the FEM. The energy resolution is $130\%/\sqrt{E} + 4.0\%$ for isolated pions.

3.1.13 Calibration of the Gas Based Calorimeters

A test beam was used to calibrate the gas calorimeters with 100 GeV/c electrons for the PEM and a combination of pions, electrons and muons in a momentum range of 20-200 GeV/c for the FHA.

For long term monitoring a wire carrying an Fe^{55} source of 5.9 keV X-rays was affixed to the outside of a number of 10 cm-long drift tubes. These tubes were distributed among the normal drift tubes of the calorimeter and used to monitor the gas gain.

The gas gain changes in response to variations of high voltage, pressure, temperature, and gas composition. These parameters were continuously recorded throughout

the run.

3.1.14 Detector Access Regions (Cracks)

The calorimeters have regions with limited instrumentation, *cracks*, in ϕ and η_D required for structural support and cabling. The sum of the cracks every 15° in ϕ where the towers meet represents only 4.8% of the complete azimuthal coverage. There are three areas in η_D that have limited resolution. The crack between the East and West sections of the central calorimeters covers $|\eta_D| \leq 0.1308$, the crack between the End Wall and the End Plug covers $1.1 < |\eta_D| < 1.4$, and the crack between the End Plug and the Forward detector covers $2.3 < |\eta_D| < 2.4$. This analysis is not affected by the ϕ cracks. The effect of the η_D cracks required corrections to the measurement. See Fig. 3.6.

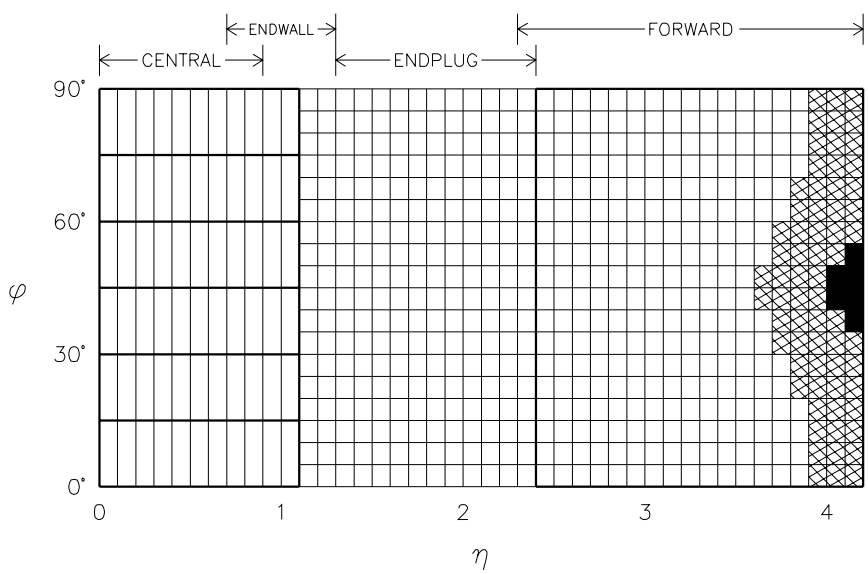

Figure 3.6: A schematic in $\eta_D - \phi$ space of the hadronic towers for the Central, End Wall, End Plug and Forward calorimeters. The shaded regions have only partial depth coverage to accommodate the low-β quadrupole magnets. The black regions have no coverage. There is complete coverage in ϕ by the electromagnetic towers out to $\eta = 4.2$. The η_D cracks occur in the regions $|\eta_D| \leq 0.1308$, $1.1 < |\eta_D| < 1.4$, and $2.3 < |\eta_D| < 2.4$.

3.2 The Data Acquisition System

The first stage of event selection is the online data acquisition system (DAQ). The rate at which events can be selected and written to tape is limited. The imposed requirements must be strict enough to reject background but also be efficient for accepting good events.

A beam crossing occurred every 3.5 μs and, with the luminosity of L $\approx 10^{31}\mathrm{cm}^{-2}\mathrm{s}^{-1}$ at least one interaction was expected at every beam crossing. This corresponds to an event rate of $\approx$ 250,000 events per second (250 kHz). The rate at which events could be written to magnetic tape was limited to $\approx$ 6 Hz. The first and second levels in the three-tiered trigger were hardware based systems that used fast analog signals to quickly reject uninteresting events. The third level was a software trigger that consisted of Unix processors capable of performing full event reconstruction.

Acceptance by Level 1 was determined within the time of one beam crossing. This required only that a hard scattering had taken place as evidenced by a large deposition of transverse energy in the calorimeter. Approximately 5,000 Hz were passed by Level 1 and evaluated by Level 2. The decision by Level 2 was made within $\approx$ 10 μs and was based on a partial reconstruction of the event. Level 2 passed 22 Hz. A digital readout of the front end electronics, requiring $\approx$ 3 ms, was performed only for an event accepted by Level 2. Level 3 had 48 processors that could handle 48 events in parallel and processed each event for roughly 1 s. During this time each event was reconstructed as completely as was necessary to determine if it should be rejected or written to magnetic tape. Level 3 passed 6 Hz. A detailed description of the Level 3 trigger is given in Appendix C.

The data path used to collect the event information processed by the trigger began with the front end electronics. This used roughly 160,000 electronic channels and interfaced with the rest of the DAQ. All calorimeter output voltages were evaluated immediately before and just after a bunch crossing by each of the 129 front-end analog RABBIT crates mounted on the detector. The integrated signal charge recorded from the products of an interaction is proportional to the difference in the two measured voltages. If the event passed Level 2, the calorimeter information was digitized by the analog-to-digital converters in the front-end-electronics and read out by a fast intelligent scanner (MX). Information from the tracking systems was recorded by front-end Fastbus time-to-digital converters and, if digitized, was read out by an intelligent scanner called an SSP. Both the MX and SSP scanners can buffer four events. The digital information was input to the Event Builder which formatted the event into the data structure used in offline analysis. The event data were then transmitted to memory in the Level 3 processors.

The Fastbus network was used to establish electronic transfer of information in an organized way between the different parts of the data acquisition system. The data flow was monitored by programs that ran on the B0 VAX cluster.

3.2.1 Level 1

The Level 1 photon trigger required that the sum of transverse energy in any single central trigger tower exceed a threshold of 6 GeV with at least 4 GeV of this deposited in the electromagnetic calorimeter section of the tower. A trigger tower is defined to be 15° in ϕ and ≈ 0.2 in η_D. In the central detector this is two standard calorimeter towers that are consecutive in η_D. Different single tower thresholds could be required

for different calorimeters.

3.2.2 Level 2

Identification of photons, of leptons, and of jet structure, as well as calculation of the missing E_t and of the summed scalar E_t was performed by the Level 2 hardware.

A clustering algorithm identified jet structure by selecting any calorimeter tower in which transverse energy above a specified threshold was recorded and summing the transverse energy in this seed tower with that of its neighbors. Electromagnetic clusters were distinguished from hadronic by the ratio of total energy over electromagnetic energy in the cluster. Reconstruction of high momentum charged tracks in two dimensions and a rough momentum measurement was performed by a hardware track processor that used signals from the CTC. Photon candidates were identified as clusters with a ratio of total E_t to electromagnetic E_t less than or equal to 1.125. The cluster was required to have $|\eta_D| < 1.19$ and total $E_t > 16$ GeV.

The neural net hardware board calculated an analog sum of transverse energies in towers surrounding the seed tower of a Level 2 cluster. This sum included all towers, both electromagnetic and hadronic, in a 6×5 array of trigger towers excluding only the electromagnetic part of the seed tower. The online isolation cut required that this sum be less than 5 GeV of E_t. This trigger tower array corresponds roughly to a cone of radius 0.65 in $\eta_D - \phi$ space.

Since the experiment ran with many different triggers simultaneously, a maximum acceptance rate was imposed on those with prolific yield such as the photon trigger. This avoided excessive time during which the data acquisition system was occupied and unable to accept new events. The cross section for any physics process is a steeply falling

function of E_t, so low energy events greatly outnumber high energy events. Techniques that limit the rate include: 1) *prescaling*, i.e. accepting only a fraction of such events, and 2) raising the E_t threshold for the trigger.

Trigger rates for low energy events are typically prescaled. The trigger that selected 6 GeV photons was prescaled by a factor of 300. Out of every 300 events that satisfied the Level 2 trigger requirement, only one was actually passed by Level 2.

The neural net was used to apply an isolation cut to the trigger that selected direct photon events used in this analysis. This greatly increased the fraction of good events recorded. Without the isolation requirement the photon E_t above which no prescale was required would be 30 GeV and the 16-30 GeV photon data would be prescaled by ≈ 100. However, the 16 GeV photon trigger used the neural net to apply an isolation cut and was not prescaled. The 50 GeV and 70 GeV photon triggers did not employ the isolation requirement online since they possessed a high enough transverse energy that no prescaling was necessary. The 50 GeV photon trigger was used to check the functioning of the neural net.

3.2.3 Level 3

In Level 3, a tighter isolation cut was imposed. This required that no more than 4.0 GeV of E_t unassociated with the photon be within a cone, centered on the photon, of $r = 0.7$ in $\eta_D - \phi$ space. A fiducial cut was also required. This constrained the electromagnetic cluster to an efficient region of the CES. The centroid of the shower profile was required to be no less than 17.5 cm from the chamber center and within $14.0 < |z| < 217.0$.

Chapter 4

Event Selection and Corrections to the Data

This chapter describes the increasingly stringent selection criteria applied as the data progress from the online trigger, through offline production, and to the final analysis data set. The criteria include restrictions on the photon P_t, fiducial restrictions that ensure advantageous use of the various detectors, and restrictions to reject background events. Of the last, the isolation requirement is the most effective.

An efficiency, in some cases P_t dependent, describes the fraction of true direct photons expected to satisfy the P_t restrictions and each background rejection criterion. The fiducial restrictions accept photons deposited in optimum detector regions and are associated with an acceptance that describes, of all true direct photons, the fraction directed toward these regions. The data in this analysis are corrected for these efficiencies and acceptances.

After application of the selection criteria, the remaining data are a mixture of direct photon signal events and multiple photon background events. The signal and background are separated on a statistical basis using two independent procedures. One procedure employs the CPR and exploits the difference in conversion rate between the direct photon and multiple photon events. The other procedure employs the CES and exploits the difference in shower transverse profile between the direct photon and multiple photon events. The latter procedure offers superior separation from background

in the region $16 < P_t < 40$ GeV/c and so is used in this analysis. Since both methods agree well in the P_t region where they overlap, the systematic uncertainties of the profile method are constrained by the more limited systematic uncertainties of the conversion method.

The standard CDF routine, JTC90V [30] [31] [32], applies corrections to the measured jet energy. Effects of parton fragmentation and hadronization, detector energy resolution and jet clustering require corrections to the absolute jet energy. Relative differences in the response of individual calorimeters to an equivalent jet require corrections to the relative jet energy. Two physics processes affect the measured jet energy and are corrected. The underlying event increases the energy measured in the jet $\eta - \phi$ cone and hadronization of jet particles outside of this cone reduces the measured jet energy.

Event selection takes place in several stages:

- in the online triggers before the events are written to tape,
- in offline production running where raw data tapes are processed with output to data summary tapes (DSTs) and more abbreviated physics analysis data sets (PADs),
- and in the final physics analysis.

Events rejected online cannot be recovered. Offline production is an intensive computing task that cannot easily be repeated. Event selection criteria for these stages are kept as loose and simple as possible to simplify the calculation of and correction for inefficiencies. Tighter and more complex selection criteria are applied with physics analysis where they can be reevaluated and the analysis repeated if necessary.

A discussion of the analysis cuts used to select inclusive direct photon events and the corresponding efficiencies for those cuts is given here. All events used in this analysis were selected from the inclusive direct photon data sample after application of two additional requirements: the photon P_t must be in the range 16 GeV/c to 40 GeV/c and the jet of greatest E_t in the event must be back-to-back in ϕ with the photon within $\pm 30^o$. The latter requirement is discussed in Chapter 5.

To calculate the inclusive direct photon cross section, the acceptance of the detector and the efficiency of the data selection cuts must be determined. The cut efficiencies are evaluated by Monte Carlo event generation [24] and detector simulation, by the use of test beam electron showers, by using electrons from W and Z decay and by studying minimum bias events. The combination of all cut efficiencies and acceptances yields an efficiency of roughly 38% for photons in the region $|\eta| < 0.9$ [25].

4.1 Efficiency of Online Cuts

The selection cuts implemented in the online trigger sometimes reject good photon candidates due to the energy resolution of the calorimeters. This results in the following trigger inefficiencies:

- Level 1 may fail to make the required 6 GeV seed for a photon with a true E_t that exceeds this threshold.
- Level 2 may fail to make an electromagnetic cluster if the measured ratio of total E_t to electromagnetic E_t exceeds the true ratio.
- The Level 2 measured cluster E_t may be below the Level 2 E_t threshold when the true E_t exceeds the threshold.

Events from a minimum bias trigger were used to study the Level 1 trigger inefficiency. Events that were written to tape after passing Level 1 and before filtering by Level 2 were used to study the Level 2 trigger inefficiency. These trigger inefficiencies are less than a 1% effect for 9 GeV electrons [29].

In addition, there were two effects that sometimes caused the Level 2 neural net isolation cut to reject true direct photons. First, early in the run there existed only one neural net hardware board. Each pass over the detector was in one direction only and the first cluster encountered was the only one evaluated. Sometimes an event was rejected because the cluster evaluated was not isolated when a second cluster in the same event was isolated. For the last 73% of the data a second neural net board was added and the two most energetic clusters in each event were evaluated. Second, the energy measured in the cone surrounding the photon may exceed the isolation cut threshold although the true energy is below the threshold. The final P_t dependent efficiency varied roughly from 0.96 to 0.89 as photon P_t increased from 16 GeV/c to 40 GeV/c [29]. It was evaluated using photon candidates selected without the neural net hardware.

4.2 Offline Production

In offline production the events were fully reconstructed and written to Data Summary Tapes. A selected set of banks for each event was written to the more abbreviated Physics Analysis Data Sets. Events from data runs in which the integrity of the data was compromised due to detector effects were not included.

4.3 Offline Physics Analysis

Events included in the measurement of the inclusive direct photon cross section are selected using the criteria presented in Tab. 4.1. The corresponding efficiencies and acceptances are given for photon P_t within $16 < P_t < 40$ GeV/c and are discussed, along with the selection criteria, in the following paragraphs.

Table 4.1: Selection criteria for direct photon candidates.

SELECTION CRITERION	ACCEPTANCE OR EFFICIENCY
$P_t > 16$ GeV/c trigger	0.53 for P_t, $16-18$ GeV/c 0.9 for P_t, $18-20$ GeV/c 1.0 for $P_t > 20$ GeV/c
Neural Net trigger	$0.96 \rightarrow 0.89$ as P_t, $16 \rightarrow 40$ GeV/c
$\lvert\eta_\gamma\rvert < 0.9$	
(Total-Photon) $E_t < 2$ GeV in $r = 0.7$	0.78 at $L = 3.16 \times 10^{30}\mathrm{cm}^{-2}\mathrm{s}^{-1}$
Only one cluster > 1 GeV in relevant CES wedge	$0.94 \rightarrow 0.87$ as P_t, $16 \rightarrow 40$ GeV/c
CES Fiducial cuts in $\lvert x\rvert$ and $\lvert z\rvert$	0.64
Event vertex within $\lvert z\rvert < 60$ cm	0.95
No CTC track directed toward calorimeter cluster	0.943
No CTC track directed toward the relevant CPR chamber	0.93
Missing $E_t < 80\%$ of photon P_t	$0.97 \rightarrow 0.99$ as P_t, $16 \rightarrow 40$ GeV/c
Inoperative regions of CES and CEM	0.977
$\chi^2 < 20$ for CES shower profile	> 0.99
Overall Efficiency for Photons within $\lvert\eta_\gamma\rvert < 0.9$	≈ 0.38

The photon candidate P_t must exceed 16 GeV/c. Photons with true P_t just below (above) the trigger threshold may be erroneously accepted (rejected). The trigger efficiency gradually increases with photon P_t. Once the P_t exceeds the trigger threshold by a few GeV/c, this efficiency stabilizes at a maximum value [29]. For the trigger threshold of 16 GeV/c, the integrated luminosity was 16 pb^{-1}.

Photon candidates are required to have $|\eta| < 0.9$ since this is where the necessary

detectors are located.

No more than 2 GeV of transverse energy unassociated with the electromagnetic cluster may be present in the surrounding $r = 0.7$ cone. This isolation cut reduces the background of non-prompt photons, the decay products of mesons produced in jets. Energy from soft scattering of partons underlies the hard scattering event that satisfied the trigger requirements and contributes to the energy in the cone surrounding the photon candidate. Since the underlying event energy increases with beam luminosity, the isolation cut efficiency decreases. The transverse energy contained in random cones with no track directed toward their center was measured in minimum bias events and used to determine this efficiency. The isolation cut of 2 GeV has an efficiency of 0.78 at a luminosity of $L = 3.16 \times 10^{30}\mathrm{cm}^{-2}\mathrm{s}^{-1}$ [28].

Only one electromagnetic cluster above an energy of 1 GeV in the CES is allowed in one detector wedge. This restriction reduces the background of mesons that decay to multiple photons. The efficiency for this cut decreases from roughly 0.94 to 0.87 as the photon P_t increases from 16 GeV/c to 40 GeV/c [24]. It was evaluated using test beam electrons as well as both actual and simulated electrons from W boson decay.

A fiducial cut in the CES restricts the electromagnetic cluster to be within 17.5 cm of the chamber center and to have $14.0 < |z| < 217.0$ cm. This ensures that only the most efficient part of the CES detector is used. The efficiency for this fiducial cut is 0.64, the ratio of the good physical region of the detector to the total region [24].

The z coordinate of the event vertex is restricted to $|z| < 60$ cm. This rejects events for which the projective tower geometry is not used to full advantage. The P_t independent efficiency is 0.95 and corresponds to the fraction of minimum bias events that pass this cut [34].

The presence in the CTC of a three dimensional reconstructed charged track leading toward any of the towers in the electromagnetic cluster is characteristic of an electron. Such events are rejected. A true direct photon fails this cut if it converts in the $0.0751 \pm 0.0053\ L_{RAD}$ of material encountered before the CTC or if a track from the underlying event is associated with the electromagnetic cluster. The latter effect was evaluated using minimum bias events. This cut has an efficiency of 0.943 [28] [29].

Additionally, events in which a three dimensional reconstructed charged track leads toward the CPR chamber that recorded the photon candidate are rejected. A true direct photon is rejected if it is associated with a track from a minimum bias event. The efficiency of this cut decreases as beam luminosity increases and is 0.93 at a beam luminosity of $3.16 \times 10^{30}\mathrm{cm}^{-2}\mathrm{s}^{-1}$ [28].

Events in which the missing transverse energy is greater than 80% of the photon candidate energy could result from cosmic rays or Texas towers and are rejected. Texas towers are large depositions of energy in the calorimeter due to secondary charged particles moving in the plane of the ionization chamber instead of perpendicular to it. The efficiency of this cut increases from 0.97 to 0.99 as the photon P_t increases from 16 GeV/c to 40 GeV/c [29].

An acceptance correction of 0.977 accounts for the inoperative regions of the CES and CEM.

Events with a transverse shower profile in the CES that had $\chi^2 > 20$ when compared to the transverse shower profile of a true single photon were rejected from the inclusive direct photon data sample regardless of whether the CES or CPR was used to perform the background subtraction. The efficiency for photons is > 0.99.

4.4 Background Subtraction

Most of the $\eta \rightarrow 3\pi^o \rightarrow 6\gamma$ and $K_S \rightarrow 2\pi^o \rightarrow 4\gamma$ background events are rejected by the analysis cuts. The data that pass are a mixture of direct photons and the remaining background events, primarily $\pi^o \rightarrow \gamma\gamma$ and $\eta \rightarrow \gamma\gamma$. At the CES, the distance of separation for the two photons from a 40 GeV/c π^o is $\approx$ 2 cm while the transverse shower profile for a single photon is $\approx$ 3 cm [24]. It is not possible, on an event-by-event basis, to distinguish the direct photon signal from the multiple photon background.

Two statistical background subtraction methods are used. Each of these implements a selection criteria with a high efficiency for separating signal and background. One method uses the CPR to determine if a conversion occurred. The multiple photon background converts more often than the direct photon signal. The other method uses the transverse shower profile recorded by the CES. The multiple photon background has a broader transverse profile than the direct photon signal. A comparison between the transverse profile of the photon candidate and that of a test beam electron is quantified in a χ^2 value used to distinguish the transverse profile left by the multiple photon background from that left by the direct photon signal.

For this discussion the set of events that are exclusively direct photons is defined as the signal. The background is the set of events in which one or some of the multiple photons from a meson decay, in particular $\pi^o \rightarrow \gamma\gamma$, satisfies the single photon selection criteria. The background subtraction method is described here.

First make the following assignments:

- $N \equiv$ The total number of data events.
- $N_P \equiv$ The number of data events that pass a specified cut.

- $N_F \equiv$ The number of data events that fail this cut.
- $\epsilon \equiv N_P/N \equiv$ The data efficiency: the fraction of data events that pass this cut.
- $\epsilon_\gamma \equiv$ The signal efficiency: the fraction of true photon events that pass this cut.
- $\epsilon_b \equiv$ The background efficiency: the fraction of true background events that pass this cut.
- $N_\gamma \equiv$ The true number of signal events in the data.
- $N_b \equiv$ The true number of background events in the data.

Each background subtraction method separates the data events into two categories. One category contains events characteristic of the direct photon signal. The other category contains events characteristic of the multiple photon background. In reality, each category contains some combination of direct photon signal and multiple photon background events. This is expressed as $\epsilon N = \epsilon_\gamma N_\gamma + \epsilon_b N_b$. Combine this equation with $N_b = N - N_\gamma$ to obtain the number of signal events in a bin of N data events,

$$N_\gamma = \left(\frac{\epsilon - \epsilon_b}{\epsilon_\gamma - \epsilon_b}\right) N.$$

The following steps develop an event-by-event weighting factor used to measure the number of direct photons as a function of any variable since the background subtraction is preformed by summation of these weights within each bin of the measurement.

$$N_P = \epsilon_\gamma N_\gamma + \epsilon_b N_b$$

$$N_F = (1 - \epsilon_\gamma) N_\gamma + (1 - \epsilon_b) N_b$$

$$N_\gamma = \frac{(\epsilon_b - 1)}{(\epsilon_b - \epsilon_\gamma)} N_P + \frac{\epsilon_b}{(\epsilon_b - \epsilon_\gamma)} N_F$$

The weight assigned to data events that pass the cut is

$$W_P = \frac{(\epsilon_b - 1)}{(\epsilon_b - \epsilon_\gamma)},$$

and the weight assigned to events that fail the cut is

$$W_F = \frac{\epsilon_b}{(\epsilon_b - \epsilon_\gamma)}.$$

For the profile method, ϵ_γ and ϵ_b are evaluated with a simulation modeled on test beam electrons [24]. The number of events with $\chi^2 < 4$ divided by the number of events with $\chi^2 < 20$ defines ϵ.

For the conversion method, ϵ_γ expresses the probability of direct photon conversion in the material preceding the CPR. This distance, $t = 1.075 \pm 0.023\ L_{RAD}$ [25], is used to evaluate $\epsilon_s = 1 - e^{\frac{-7t}{9}}$. Including the effect of multiple photons yields $\epsilon_b = 1 - e^{-7tN_\gamma(P_t)/9}$. Here $N_\gamma(P_t)$, a function of particle P_t and type, represents the average number of photons within a 66 mrad region, or equivalently five CPR channels, centered on the direction of the photon candidate. It is derived using a detector simulation of π^o, η, and K_S^o mesons produced in the ratio of 1:1:0.4 respectively [25]. The fraction of events for which a conversion is recorded in this region defines ϵ.

For the profile method, ϵ, ϵ_γ and ϵ_b depend on P_t. For the conversion method this dependence is slight. The profile method is used in this analysis since the separation from background in the relevant P_t region, 16 Gev/c $< P_t <$ 40 GeV/c, is superior to that for the conversion method. See Fig. 4.1.

For the profile method, ϵ_b increases at both high and low P_t and reaches a minimum at $P_t \approx 20$ GeV/c. In the asymmetric decay of a π^o, one photon may gain most of the π^o momentum and satisfy the single photon selection criteria. Low momentum pions produce two photons of low energy and large separation. In some events, these

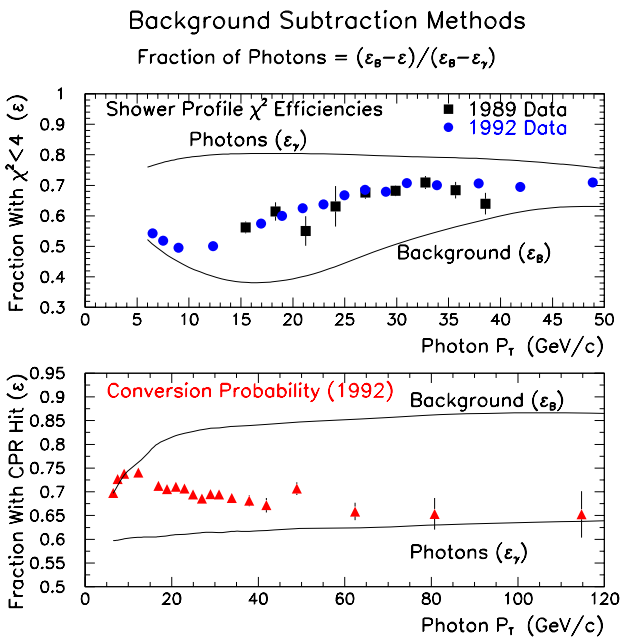

Figure 4.1: Efficiencies for the profile and the conversion methods of background subtraction [25].

photons are recorded in separate towers and one of them satisfies the single photon selection criteria. High momentum pions produce two photons of high energy and small separation. In some events, these two photons are unresolved and together satisfy the single photon selection criteria.

The conversion method has little P_t dependence. However, below 10 GeV/c, ϵ is similar to ϵ_b. The signal to background in this region is about 1 to 10. For this reason the inclusive direct photon P_t spectrum was not measured below 10 GeV/c.

Systematic uncertainty in the background subtraction corresponds to the systematic uncertainty in ϵ, ϵ_γ, and ϵ_b.

The primary uncertainty in the profile method is the shape of the shower transverse profile and fluctuations in this shape. Test beam electrons were used in the simulation of the shower shape [24]. The longitudinal development of an electron shower differs slightly from that of a photon since electrons deposit ionization energy in the detector

as soon as they enter and photons do so only after the first conversion. To study this, the thickness of material preceding the CES was varied. To study the effect of gas saturation the voltage on the CES was varied. The shower is more collimated for a particle of higher energy. Both particle energy and the angle of entry were included in the simulation of the transverse shower profile [24].

The primary uncertainty in the conversion method is the photon conversion rate which depends on the thickness, t, of material preceding the CPR. The uncertainty in t is $\pm 0.023\ L_{RAD}$ and corresponds to an uncertainty of 0.006 in $\epsilon_b = 1 - e^{-7tN_\gamma(P_t)/9}$ and 0.0078 in $\epsilon_s = 1 - e^{-7t/9}$ [29].

The conversion rate calculated using t agrees with that measured using π^o, η, and $\rho^\pm$ mesons. See Tab. 4.2. The number of daughter photons that convert and are detected by the CPR is used to measure the rate of photon conversion in the distance t. Only mesons with well separated photon decay products can be used to reconstruct the mass of the parent particle. These are identified in Fig. 4.2 by their photon mass peaks at 135 MeV/c^2, 540 MeV/c^2 and 780 MeV/c^2 respectively.

Table 4.2: The predicted and measured conversion rates of photons in the material preceding the CPR [35].

Meson	Measured Rate	Predicted Rate
π^o	0.842 ± 0.008	0.847
η	0.831 ± 0.012	0.842
$\rho^\pm$	0.836 ± 0.010	0.834

Corrections to ϵ_γ for the conversion method account for the following effects:

- The number of radiation lengths traversed changes with the angle of entry.

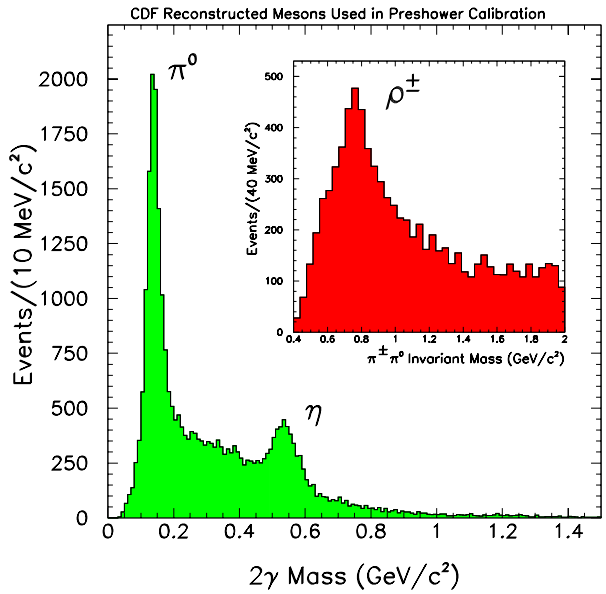

Figure 4.2: Reconstructed mesons are used for calibration of the CPR [25].

- The pair production cross section varies with photon energy [26].
- Infrequently, a conversion recorded in the CPR results from a backwards scattered electron or low energy photon. An electromagnetic shower simulation is used to study this effect [27].
- Soft photons from the underlying event sometimes result in a CPR signal. Minimum bias events are used to study this effect.
- 0.5% of the CPR was inoperative.

In the P_t region where both background subtraction methods are applicable, the measurement of the inclusive direct photon cross section shows little dependence on which method is used. See Fig. 4.3. The systematic uncertainty associated with the profile method exceeds that of the conversion method and can be constrained by the agreement between the two methods.

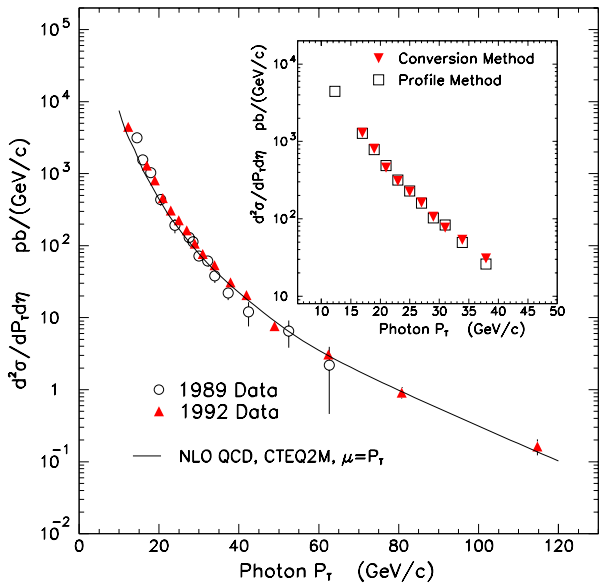

Figure 4.3: The inclusive direct photon cross section [25] measured at CDF.

4.5 Correction of the Jet Transverse Energy

The transverse energy of the measured jet may differ from that of the fragmented and clustered parton for several reasons. The measured absolute jet energy is affected by the way in which the parton fragments and hadronizes, by the detector energy resolution and by the effects of clustering. Also, there exists a relative difference in the response of different calorimeters to an equivalent jet. Corrections to both the absolute and the relative jet energy are applied using the standard CDF routine, JTC90V.

The relative correction is determined by using dijet events with one jet in the central detector, $0.2 < |\eta_D| < 0.7$. The other of the pair, the probe jet, is allowed to range over all η. The central jet energy is well measured. The ratio of P_t between this jet and the probe jet varies from unity when probe jet energy is lost in a detector crack.

The absolute energy scale of the calorimeters relates the true energy of a hadron to the measured energy. If these two values differ it becomes necessary to correct the

measured jet energy for this difference.

Only a fraction of the energy is deposited in the active material, the scintillator layer, of a sampling calorimeter such as the CEM and CHA. For identical incident particles the detector response varies statistically. The shower profile, i.e. energy deposition as a function of calorimeter layer, varies with the energy of the primary particle and the type of particles in a hadron jet.

Consequently, the signal output of the detector is only approximately proportional to the particle energy and non-linear corrections are required. These have been studied extensively with several different methods that include test beams and use of the requirement that $E/p \approx 1$ for electrons. The latter allows a comparison of the energy deposited in the calorimeter by an electron with a measurement of its momentum using the CTC. A further requirement is that, on average, there be a balance of the E_t in $p\bar{p}$ collisions. The results of these studies are included in the detector simulation used to evaluate the absolute jet energy correction.

This correction is determined by the generation of partons, simulation of the detector effects on the resulting jets, and comparison of the original fragmented and clustered parton P_t with the P_t of the resulting measured jet. The parton P_t is determined by summing the transverse momentum of all particles in the cone before simulation of detector effects [30].

Two physics processes cause the measured jet energy to differ from the true value. The underlying event deposits energy within the jet clustering cone. Some jet energy is lost when particles hadronize outside of the jet clustering cone.

Underlying event energy is subtracted from the measured jet energy. For a cone of $r = 0.7$ and a beam luminosity of $3.16 \times 10^{30}\mathrm{cm}^{-2}\mathrm{s}^{-1}$, the underlying event contributes

roughly 2 GeV to the jet energy. This is the level of energy deposited in the central calorimeter towers in minimum bias events. It is independent of the jet P_t.

The energy out-of-cone correction is determined by simulating the fragmentation of a generated parton, clustering the resulting jet after detector simulation and summing the P_t of all associated hadrons that are outside of the jet cone.

The data used in this measurement of the lead jet η distribution in direct photon events satisfy the inclusive direct photon selection criteria and have photon E_t between 16 GeV and 40 GeV. The only additional requirement is that the lead jet and photon be back-to-back within $\Delta\phi = \pm 30^o$. This rejects events in which the lead jet is misidentified.

It also rejects events strongly affected by K_t which gives the jet in a $2 \rightarrow 2$ process a momentum component transverse to the momentum of the photon. This is a result of soft gluon radiation from the initial or final state parton and is not modeled in the NLO theory.

Finally, it rejects the NLO $2 \rightarrow 3$ process. This process is included in the theory but rejected from the data sample due to the rare occurrence of lead jet misidentification. Appendix E explores this issue.

Chapter 5

Measurement of the Lead Jet η Distribution

This chapter describes the techniques developed to correct the lead jet η distribution for detector effects and to determine the associated systematic uncertainty. There are two ways in which mismeasurement of jet energy distorts the η distribution of the lead, or highest E_t, jet. First, the E_t-weighted jet centroid shifts if detector effects alter the distribution of E_t within the jet $\eta - \phi$ cone. Second, the lead jet is misidentified if the E_t of another cluster in the event fluctuates above that of the true lead jet. Simulated events model these detector effects and provide information used for their correction. The systematic uncertainty associated with the measurement lies in the characteristics of these simulated events.

The detector η cracks and the calorimeter energy resolution distort the measured lead jet η distribution. Both affect the measured distribution of E_t within the jet $\eta - \phi$ cone which determines the E_t-weighted jet centroid. They also affect the measured total jet E_t which identifies the lead, or highest E_t, jet.

Unrecorded jet energy alters the distribution of E_t within the jet $\eta - \phi$ cone and shifts the E_t-weighted jet centroid from the true position. If jet E_t deposited in the crack is not recorded, only the E_t deposited in the calorimeter towers bordering the crack can be used to determine the E_t-weighted jet centroid. Jets directed toward the crack region are sometimes reconstructed to either side.

In addition, the lead, or highest E_t, jet is misidentified if its total E_t fluctuates below that of another E_t cluster in the event. In some events a photon and two jets emerge from the hard scattering and, rarely, the lead and second jets in such an event interchange. Also, in most events jets unassociated with the hard scattering are reconstructed and are sometimes misidentified as the lead jet. These result from involvement of the underlying event, multiple interactions and soft initial or final state gluon radiation. Rarely, enough jet energy is lost that the event contains no reconstructed jets. Appendix D describes lead jet selection.

The lead jet η distribution of Fig. 5.1a shows the resulting depletion of events in each of the detector cracks at η of roughly 0.1, 1.3 and 2.4. Simulated events provide information used to study and correct these detector effects. This measurement uses the larger bin size of Fig. 5.1b to minimize the required corrections.

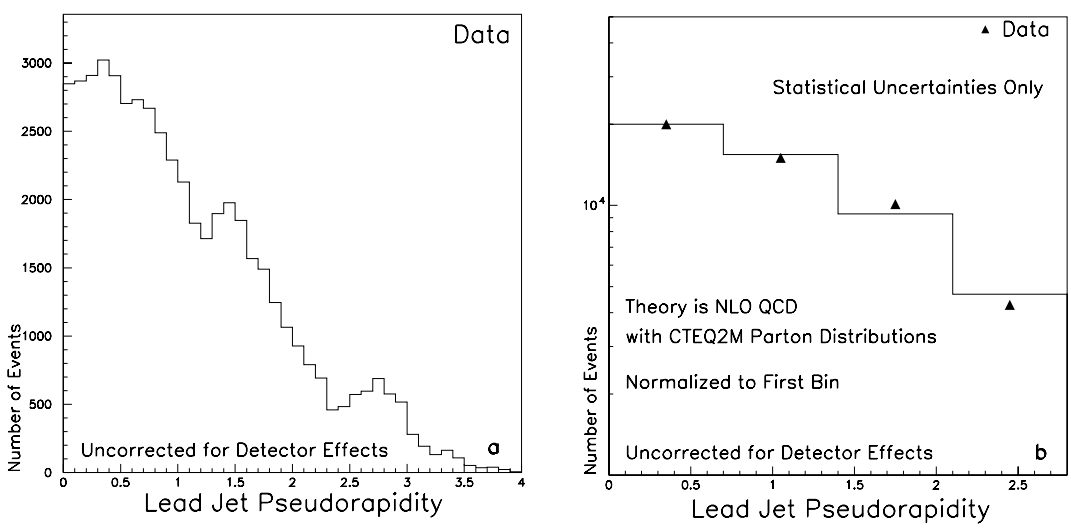

Figure 5.1: **a)** The local minima at the detector cracks of $\eta \approx 0.1$, 1.3 and 2.4, result from loss of jet energy in these regions and consequent reconstruction of the E_t-weighted lead jet centroid to either side or misidentification of the lead jet. **b)** The measurement uses large bins to minimize the correction of detector effects.

Simulated events model the detector η resolution. The generated parton provides the true η. The associated jet of particles is subjected to detector simulation prior

to clustering and provides the measured η. The perfect detector would measure not the initial outgoing parton but the particles resulting from the hadronization of this parton. In this document, *parton* refers to the physical object formed by clustering these particles. The E_t-weighted centroid of this cluster yields the parton η position. After the detector simulation, these particles are again clustered to yield the E_t-weighted centroid of the associated final *jet*. The same clustering scheme is used for both the parton and the jet. It involves summation of the E_t within a cone of radius r = 0.7 in $\eta - \phi$ space centered on an initial seed E_t. The E_t weighted centroid of the resulting cluster is calculated and the E_t within r = 0.7 of this new centroid is summed. This iterative process continues until the E_t weighted centroid becomes stable. Ideally the jet should always be reconstructed in the same measurement bin as the associated parton. Comparison of parton η to the associated jet η provides information used to study and correct detector effects.

The simulated events used in this analysis satisfy all selection criteria applied to the data including, unless explicitly indicated otherwise, the requirement that the photon and lead jet be back-to-back in ϕ within $\Delta\phi = \pm 30^o$.

Throughout this document $2 \rightarrow 2$ refers to generated LO events which have a photon and one parton in the final state. To denote that underlying event simulation is included this becomes $2 \rightarrow 2$+UE. To denote that K_t simulation is included this becomes $2 \rightarrow 2+K_t$. Likewise, $2 \rightarrow 3$ represents NLO generated events which have a photon and two partons in the final state. After detector simulation, the $2 \rightarrow 2$ events usually contain one or two reconstructed jets, and the $2 \rightarrow 3$ events usually contain two or three reconstructed jets. However, both LO and NLO generated events may contain zero, one, two or more reconstructed jets after detector simulation.

In 2 $\rightarrow$ 2 events, any additional jets result entirely from fragmentation and clustering effects. In 2 $\rightarrow$ 2+UE events, additional jets also arise from the simulated underlying event energy. The 2 $\rightarrow$ 3 events introduce the added effect that the lead and second jets might interchange. The system grows quickly in complexity.

Most data events have only one jet associated with the hard scattering although they may contain additional E_t clusters. These data events are termed photon + 1 jet events. Data events with two jets from the hard scattering are termed photon + 2 jet events. In the data, the continuum of radiated gluon momenta obscures the distinction between a 2 $\rightarrow$ 2 event and a 2 $\rightarrow$ 3 event. Soft gluon radiation from the initial or final state parton adds to the final jet E_t in a 2 $\rightarrow$ 2 event while hard gluon radiation produces the second jet in a 2 $\rightarrow$ 3 event.

Requiring that the photon and lead jet be back-to-back in ϕ within $\Delta\phi = \pm 30^o$ rejects events strongly affected by K_t and rejects events that contain misidentified lead jets. The soft gluon radiation that imparts K_t occurs in the non-perturbative kinematic regime and so is not modeled by the NLO theory. Appendix E describes the characteristics of events selected, and of events rejected, by the back-to-back cut.

5.1 The Magnitude of the Detector Effects

The simulated events show that detector effects result in both misidentified lead jets and altered distributions of E_t within the lead jet $\eta - \phi$ cone, particularly near the detector η cracks. These effects distort the measured lead jet η distribution. The following discussion of the former and latter detector effects is expanded in Appendix E.2 and Appendix F respectively.

This section presents R_i^G and R_i^L which respectively represent, for bin i, the fractional increase and decrease of the jet η distribution relative to the parton η distribution due to various detector effects. Let P_i represent the number of partons in bin i, J_i^G the number of jets artificially gained by bin i, and J_i^L the number of jets lost from bin i. Then $R_i^G = J_i^G/P_i$ and $R_i^L = J_i^L/P_i$. The difference, $\Delta R_i = R_i^G - R_i^L$, quantifies the effective distortion. Section 5.3 explores the sensitivity of the corrected data to these effects.

5.1.1 Detector η Resolution: Detector Effects That Alter the Distribution of E_t Within the Jet $\eta - \phi$ Cone

Detector effects that alter the distribution of E_t within the lead jet $\eta - \phi$ cone sometimes place an event into the wrong bin. The $2 \rightarrow 2+K_t$ events contain correctly identified jets and test detector effects due to the mismeasured distribution of E_t within the lead jet $\eta - \phi$ cone.

For these events, Fig. 5.2a presents the fraction of partons in each bin reconstructed as jets in a bin at higher η as well as the fraction reconstructed as jets in a bin at lower η. The jet centroid is usually reconstructed toward lower η since the steeply falling η spectrum places more events at the lower η edge of each bin than at the higher η edge.

Figure 5.2b presents R_i^G and R_i^L for these events. The jet and parton η distributions are similar in the first two bins; however, $R_4^L = 0.16$. Jets lost from bin four are usually reconstructed in bin three so that $R_3^G = 0.12$. The steep spectrum enhances distortion of the last bin, bin five, which shows $R_3^G = 0.28$. The underlying event simulation introduces lead jet misidentification. This effect is discussed in the following section.

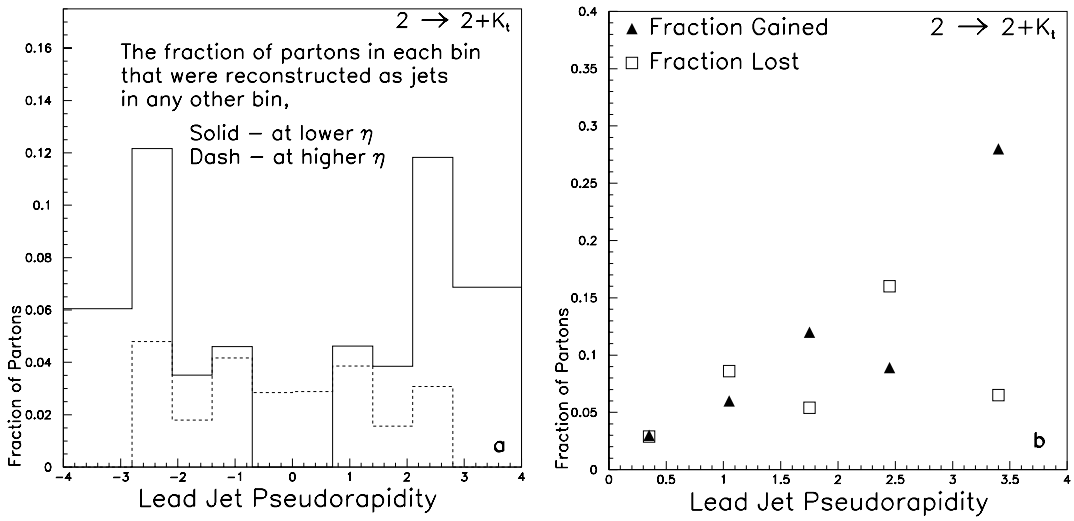

Figure 5.2: **a)** The fraction of partons in each bin reconstructed as jets in a bin at higher η, is overlayed with the fraction of partons in each bin reconstructed as jets in a bin at lower η. **b)** The R_i^G and R_i^L corresponding to the shift in jet η that results from changes to the distribution of E_t within the jet $\eta - \phi$ cone near the detector η cracks.

5.1.2 Misidentification of the Lead Jet

Lead jet misidentification sometimes places an event into the wrong bin. It occurs in the following ways:

1. The lead jet may be replaced by an upward fluctuation in the underlying event energy.

2. The lead jet may be replaced by a jet produced in a multiple interaction.

3. The event may contain no reconstructed jet.

4. The second jet associated with the hard scattering in a 2 $\rightarrow$ 3 process may replace the lead jet.

Figure 5.3 presents R_i^G and R_i^L for various means of lead jet misidentification. Figure 5.3a overestimates the effect of the underlying event and multiple interactions. It shows the first four bins to have $|\Delta R_i| < 5\%$ and bin five to have $\Delta R_5 = 56\%$. Again, this enhanced sensitivity of bin five results from the steep η spectrum. The E_t clusters

found in minimum bias data, which include events with multiple interactions, are both fewer in number and lesser in E_t than those produced by the underlying event simulation. It will be shown presently that the corrected data are insensitive to the simulated underlying event. It follows that they must be insensitive to multiple interactions as well.

In Fig. 5.3b $R_i^L < 7\%$ and in Fig. 5.3c, $|\Delta R_i| < 3\%$. Figure 5.3c overestimates the effect of lead and second jet interchange in $2 \rightarrow 3$ events since the majority of the data are photon + 1 jet events, not photon + 2 jet events.

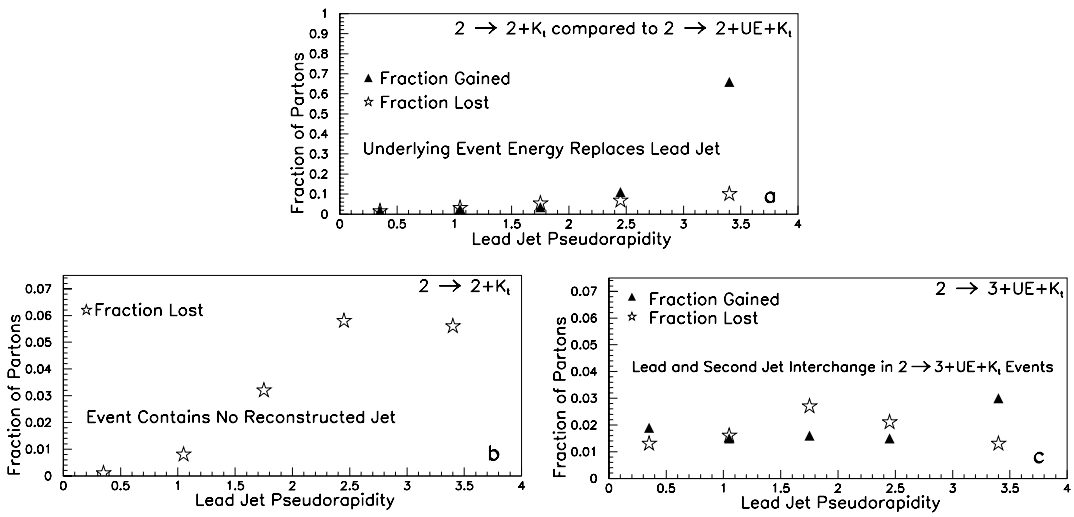

Figure 5.3: The R_i^G and R_i^L corresponding to the following means of lead jet misidentification: **a)** the lead jet is replaced with underlying event energy, **b)** the event contains no reconstructed jets, and **c)** the lead and second jets switch in a $2 \rightarrow 3$ event.

5.2 Correction of Detector Effects

Simulated events show that the η coordinate of the parton and that of the associated jet sometimes occupy different bins of the lead jet η distribution. The data, corrected with this information, are presented in Fig. 5.4. Appendix G describes the correction procedure and Appendix H depicts the detector η resolution modeled by simulated

events of various topology.

Bin four undergoes the largest correction. It increases by 15% of its uncorrected value primarily to replace jets reconstructed in the third bin but associated with partons in the fourth bin. See Tab. 5.1.

The data normalized to the NLO theory with CTEQ2M parton distributions and divided by the value of the first bin yield discrimination among parton distributions in the shape comparison of Fig. 5.5a. The uncorrected data are presented in Fig. 5.5b.

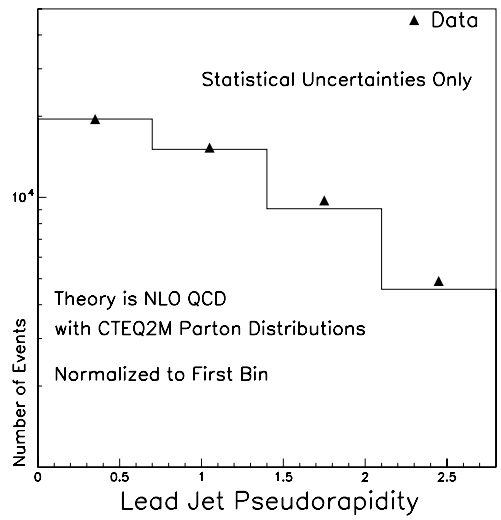

Figure 5.4: The lead jet η distribution corrected for detector effects.

5.3 Systematic Uncertainty Associated with Detector Effects

The systematic uncertainty quoted in Fig. 5.5a is determined by variation of the standard simulated events used in the correction procedure. These events satisfy the same selection criteria as the data and have the following characteristics:

- All events result from the $2 \rightarrow 2$ process,
- with the η spectrum shape dictated by the Martinelli [37] parton distributions,

Table 5.1: The changes in the measurement that result from the correction of detector effects.

	Bin 1	Bin 2	Bin 3	Bin 4
The Number of Events in the Uncorrected Data	19990	15015	10116	4283
The Number of Events in the Corrected Data	19507	15317	9745	4905
The Total Number of Events Added	855	1801	1051	1107
The Total Number of Events Subtracted	1339	1499	1422	484
The Final Correction (Added-Subtracted)	-484	302	-371	622
The Fraction of the Bin:				
Added Back to the Bin	0.04	0.12	0.10	0.26
Subtracted from the Bin	0.07	0.10	0.14	0.11
Used in the Final Correction	-0.03	0.02	-0.04	0.15

- with underlying event simulation,
- with K_t simulation,
- and with the standard CDF detector simulation, QFL.
- For all events the lead jet and photon are back-to-back in ϕ within $\Delta\phi = \pm 30^o$.

D_i^C represents the number of data events in bin i obtained when the data are corrected using the standard event simulation. Variation of one characteristic in the simulated events changes this value to D_i^{CV}. The difference, $\Delta B_i^V = D_i^C - D_i^{CV}$, is given in Fig. 5.6 for each variation. The following paragraphs describe each variation and present the corresponding greatest value of $|\Delta B_i^V|$.

Figure 5.6a tests the effect of altering the simulated distribution of E_t within the jet $\eta - \phi$ cone near the η detector cracks and thus altering the simulated jet η resolution. In the detector simulation, the model of shower spreading and the detector geometry

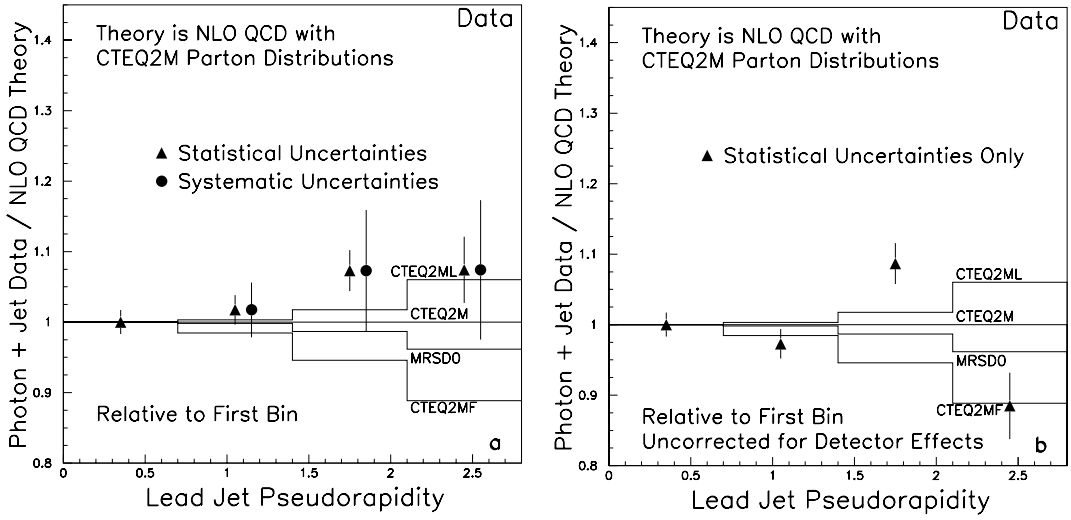

Figure 5.5: The lead jet η distribution in the data normalized to the value of the first bin and divided by the NLO theory based on CTEQ2M parton distributions. This measurement is presented **a**) corrected for detector effects and **b**) not corrected for detector effects.

determine the distribution of energy in the calorimeter towers that border the η cracks. The standard correction uses the standard detector simulation. If energy deposited in the crack border towers is increased by 50% of its value before the jet E_t is clustered $|\Delta B_3^{50\%}| = 0.053$. Appendix I details this study.

Figure 5.6b tests the effect of underlying event energy which increases the rate of lead jet misidentification. SETPRT models the underlying event energy on dijet data from the 1988-1989 collider run and, according to comparison with minimum bias data, overestimates the effect. The standard correction includes underlying event simulation. If the underlying event is not simulated $|\Delta B_3^{NoUE}| = 0.048$. Appendix J details this study.

Figure 5.6c tests the effect of 2 $\rightarrow$ 3 events which increase the rate of lead jet misidentification. A mixture, prior to the back-to-back cut, of 50% 2 $\rightarrow$ 2+UE+K_t and 50% 2 $\rightarrow$ 3+UE+K_t events, here termed S50:50 events, overestimates the photon + 2 jet component of the data. The standard correction uses exclusively 2 $\rightarrow$ 2+UE+K_t events. If S50:50 events are used $|\Delta B_4^{NLO}| = 0.018$. Appendix K

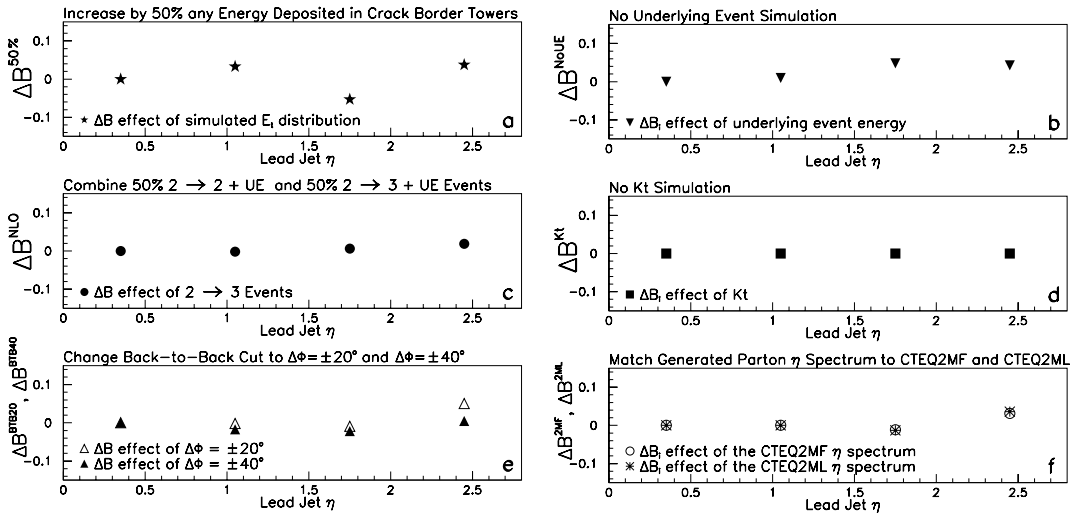

Figure 5.6: The ΔB_i^V corresponding to variation of the following simulated event characteristics: **a)** the simulated distribution of E_t within the jet $\eta - \phi$ cone near the detector η cracks, **b)** the underlying event energy, **c)** the $2 \rightarrow 3$ contribution, **d)** K_t, **e)** the back-to-back requirement and **f)** , the generated η spectrum.

details this study.

Figure 5.6d tests the effect of K_t which occurs in the non-perturbative kinematic regime and so is not modeled in the NLO theory of Fig. 5.5. The back-to-back requirement rejects events strongly affected by K_t. SETPRT models K_t on dijet data from the 1988-1989 collider run. The standard correction includes K_t simulation. If K_t is not simulated $|\Delta B_{3,4}^{NoK_t}| = 0.037$. Appendix L details this study.

Figure 5.6e tests the effect of altering the back-to-back cut which, when tightened, selects events of higher quality. The standard correction requires that the photon and lead jet be back-to-back in ϕ within $\phi = \pm 30^o$. If this requirement is tightened to $\phi = \pm 20^o$, then $|\Delta B_4^{BTB20^o}| = 0.051$; if it is relaxed to $\phi = \pm 40^o$, then $|\Delta B_3^{BTB40^o}| = 0.022$. Appendix L details this study.

Finally, Fig. 5.6f tests the effect of the generated η spectrum which, when steeper, increases (decreases) the influence of detector characteristics at the low (high) η edge of each bin. The parton distributions CTEQ2MF and CTEQ2ML provide the greatest

separation in the NLO theory of Fig. 5.5. The standard correction uses events generated with Martinelli parton distributions. If the η spectrum of the generated partons is matched to that produced by the CTEQ2MF parton distributions $|\Delta B_4^{2MF}| = 0.031$; if it is matched to that of the CTEQ2ML parton distributions $|\Delta B_4^{2ML}| = 0.036$. Appendix M details this study.

5.4 Systematic Uncertainty Associated with Background Subtraction

The systematic uncertainty associated with the CES method of background subtraction used in this analysis is constrained by the more limited uncertainty of the CPR method since both methods produce comparable results. Appendix N discusses this uncertainty, represented by ΔB_i^{BS}, which is $< 2\%$ in each bin.

5.5 Final Statistical and Systematic Uncertainty

The ΔB_i^V provide a range of values that, combined with ΔB_i^{BS}, determines the final systematic uncertainty of the corrected data,

$$\sigma_i^{SYS} = \sqrt{\sum_V (\Delta B_i^V)^2 + (\Delta B_i^{BS})^2}.$$

Table 5.2 presents the final statistical and systematic uncertainty.

Table 5.2: The Final Statistical and Systematic Uncertainty

	Bin 1	Bin 2	Bin 3	Bin 4
Systematic Uncertainty		0.039	0.086	0.099
Statistical Uncertainty	0.017	0.021	0.029	0.047

Chapter 6

Conclusion and Discussion of the Measurement

In conclusion, the lead jet η distribution in direct photon events in $p\bar{p}$ collisions at $\sqrt{s} = 1.8$ TeV probes parton x in the range $0.015 < x < 0.15$ and is particularly sensitive to the high x parton. In this measurement the photon P_t is constrained to $16 < P_t < 40$ GeV/c. Direct photon production accesses the gluon momentum distribution through the QCD Compton process which dominates in this kinematic region. The measurement is consistent with NLO QCD predictions and favors the parton distributions CTEQ2ML and CTEQ2M. See Fig. 6.1. It will be used by the CTEQ collaboration [12] in a global fitting procedure to refine our current understanding of parton distributions.

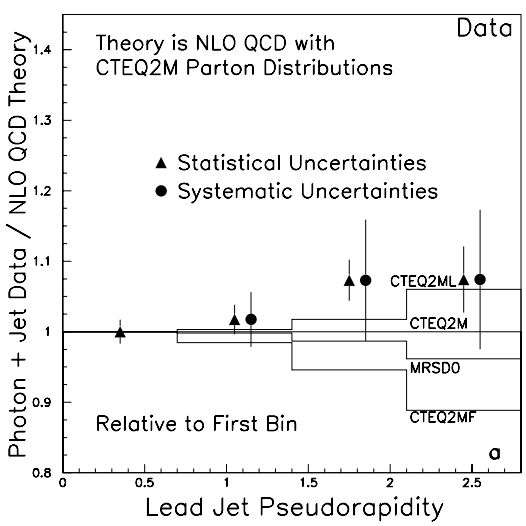

Figure 6.1: The lead jet η distribution in the data normalized to the value of the first bin and divided by the NLO theory based on CTEQ2M parton distributions.

6.1 Theoretical Uncertainty: the Renormalization Scale

The theoretical uncertainty is represented in Fig. 6.2 which shows the measurement compared to the NLO theoretical calculation with different renormalization scales.

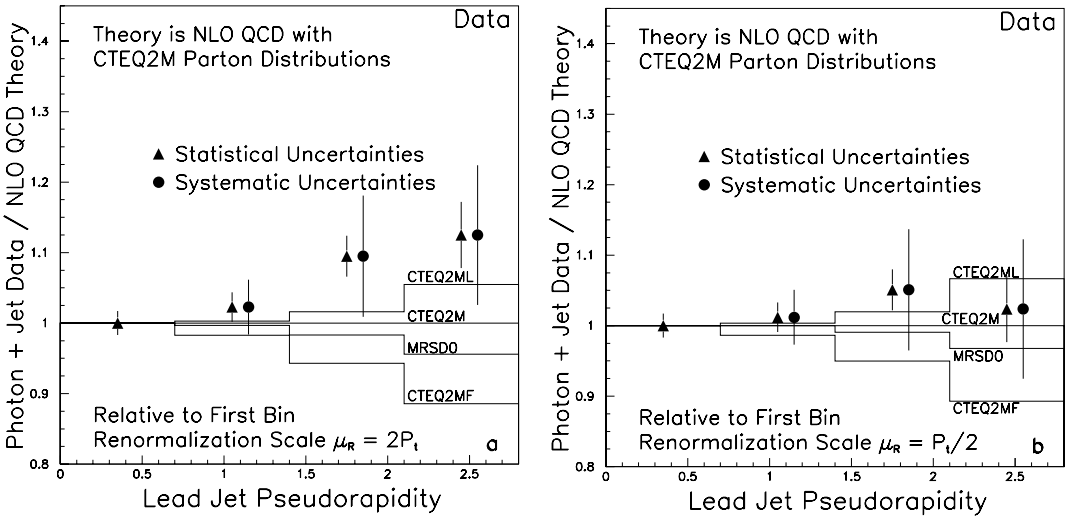

Figure 6.2: The effect of variation in the μ_R scale in the theory. **a)** The measurement with a renormalization scale of $\mu_R = 2P_t$ and **b)** with $\mu_R = P_t/2$.

Table 6.1: Results for different renormalization scales.

	Bin 1	Bin 2	Bin 3	Bin 4
Main Result $\mu_R = P_t$	1.00	1.017	1.073	1.074
Renormalization Scale $\mu_R = P_t/2$	1.00	1.012	1.051	1.024
Renormalization Scale $\mu_R = 2P_t$	1.00	1.023	1.095	1.125

Appendix A

Finding μ_F, Factorization Methods

A factorization method must be selected to determine μ_F. The K_t *cut off* method, although not widely used because it is not Lorentz invariant, provides a clear description of the meaning of μ_F and is described here. The parton distributions listed in Tab. 2.2 were extracted using the $\overline{MS}$ method which is Lorentz invariant and is more convenient for use in calculations than the K_t cut off method.

Consider a quark that radiates a gluon with momentum, K_t, at an angle, $\Delta\theta$, from the quark's direction of motion. If $\Delta\theta \approx \frac{K_t}{Q} < \frac{\mu_F}{Q}$ then, in the collinear approximation, the gluon is considered part of the quark and the gluon momentum is accounted for in $Q(x)$. If, however, $\frac{K_t}{Q} > \frac{\mu_F}{Q}$, the gluon is considered part of the hard scattering process and the gluon momentum is accounted for in the parton level cross section. Selection of a specific direction, the K_t of a radiated gluon, destroys Lorentz invariance in this factorization scheme.

Appendix B

The $p\bar{p}$ Beam

The production of the beam is discussed in the latter part of this Appendix. Maintainance of beam stability influences the method of beam production and is discussed first.

In order to obtain maximum luminosity, the beam must be stable and well focused. Longitudinal oscillations are controlled by manipulating the phase and amplitude of the driving RF voltage. Transverse oscillations are damped by repeated measurement and readjustment of the beam position.

B.1 Longitudinal Synchrotron Oscillations

Protons that are not traveling in *synchronous phase* with the driving RF voltage exhibit longitudinal synchrotron oscillations. The longitudinal position of the proton within the bunch determines the phase of the RF field that that proton encounters in the gaps between the drift cells of the accelerator.

A synchronous proton enters the gap when the oscillating electromagnetic field is at the phase most effective for both acceleration and bunch stability. In the linear accelerator the length of each successive drift cell is increased so that an accelerating proton traveling in synchronous phase always encounters the same optimal electromagnetic field gradient and intensity. In the synchrotron this is achieved by a continuous

increase in the frequency of the driving voltage as the proton is accelerated and as the guiding magnetic field generated by the dipole magnets is intensified.

The synchronous phase angle is defined to be $\phi_s = 0^o$ when the RF voltage reaches maximum amplitude in the gap. If this maximum accelerating voltage were used then protons lagging behind the main synchronous group would be given a smaller acceleration and fall farther behind. Protons in advance would also experience a smaller acceleration. This might cause them to fall behind the main group and likewise be lost. The nonrelativistic protons in the Fermilab linear accelerator enter each gap between drift cells when $\phi_s = -32^o$. This offset from the maximum accelerating voltage results in a greater acceleration for protons traveling behind the synchronous bunch and a smaller acceleration for those protons ahead of the bunch. Stable longitudinal oscillations about the synchronous phase are thus established.

In the Fermilab booster synchrotron, when the proton energy exceeds ≈ 4.2 GeV, the bunches go through *transition*, the point where they are sufficiently relativistic that their speeds do not increase significantly with energy. Now, the lower momentum protons lead the group since their orbital radius is smaller and their transit time shorter. The higher momentum protons travel a farther distance at a greater orbital radius and consequently fall behind the group in time. This is the reverse situation to the nonrelativistic case described above and the synchronous phase must be appropriately adjusted to maintain the stability of the longitudinal oscillations.

B.1.1 Bunch Rotation

Stable synchrotron oscillations, when combined with the conservation of phase space as expressed in Liouville's theorem [22], can be exploited to limit differences in phase

or momentum among protons in a bunch. If the RF voltage driving a bunch of protons with a narrow momentum distribution is reduced to minimal amplitude for a few milliseconds then synchrotron oscillations will subside and the protons will spread out longitudinally, occupying many different phases. If the RF voltage is then quickly increased a synchrotron oscillation will begin. After completing one half of the oscillation a relativistic proton of less (greater) than average momentum will have moved from its position in front of (behind) the main group, through the ideal synchronous position, to a position behind (in front of) the main group. If the RF voltage is suddenly decreased after one quarter of an oscillation the out-of-phase protons will remain with the main group at the synchronous phase. By conservation of phase space, the resulting narrow spread in time corresponds to a large momentum spread. This procedure, called *bunch rotation*, can be reversed so that a bunch with a short distribution in time (phase) can be manipulated to have a short momentum distribution. As will be described presently, this technique is used to produce antiprotons with a narrow momentum distribution.

B.2 Transverse Betatron Oscillations

The protons also experience stable Betatron oscillations, transverse to the direction of motion, resulting from the divergence in the initial proton source and small asymmetries in the guiding magnetic fields. The wavelength is associated with the focal length of the quadrupole magnets which focus the beam in one transverse plane while defocusing it in the other. Alternation of the quadrupole magnets that focus the beam vertically with those that focus in the horizontal direction results in a focused beam with stable transverse oscillations. The amplitude of the Betatron oscillations is damped by the process of *stochastic cooling* which will be discussed presently.

B.3 Production of the Proton Beam

A magnetron surface-plasma source is used to produce negative Hydrogen ions, H^-, from which the proton beam is eventually derived. This device sits in a constant magnetic field and consists of a cathode encased in an anode. A dense plasma is produced from Hydrogen gas held at a few hundred mtorr in the 1 mm gap between the cathode and anode. Absorbed Hydrogen atoms are sputtered off the cathode surface in response to bombardment by energetic plasma particles. Cesium vapor is added to the gap to reduce the work function of the cathode surface so that 10% of these released Hydrogen atoms become H^- when they capture a surface electron. The 18 KeV negative Hydrogen ion beam is produced in a metal dome held at -750 kV by a Cockcroft-Walton generator. It is accelerated to 750 keV as it traverses the electrostatic accelerating column toward the transport line to the linear accelerator (LINAC) which is held at ground potential.

After raising this energy to 400 MeV using the LINAC the H^- ions are passed through a thin carbon foil and the electrons are stripped away. The resultant protons are injected into a booster synchrotron that increases their energy to 8 GeV. The proton energy is then raised to 150 GeV by injection into the Main Ring (MR) which sits above the Tevatron in the accelerator tunnel and passes above the CDF detector. Finally, the protons are injected into the Tevatron which passes directly through the center of the CDF detector. See Fig. 3.1.

B.4 Production of the Antiproton Beam

Protons are extracted from the Main Ring and directed onto a nickel target to produce antiprotons. Since antiprotons will eventually be injected into the Main Ring it is desirable to produce them at the 8 GeV standard injection energy of protons from the booster into the Main Ring. Protons of 120 GeV are used since this is the most effective proton energy for the production of 8 GeV antiprotons.

Roughly 10^7 antiprotons are created in each collision of a proton bunch with the target. The proton bunches in the Main Ring have a narrow momentum distribution and, before extraction, are rotated by 90° in phase space (that is 1/4 of the wavelength of a synchrotron oscillation) such that they have a short time distribution. The antiprotons maintain the short time distribution of the incident proton bunch.

The initial spatial divergence of the newly produced antiprotons is corrected by the cylindrical Lithium lens located directly after the target. The azimuthal magnetic field produced by a pulsed current of about 0.5 MA directed along the cylindrical z axis forces the antiprotons to emerge from the lens with parallel trajectories. Antiprotons of 8 GeV are selected by a pulsed dipole magnet and injected into the debuncher.

Upon injection to the debuncher, each of the ≈ 83 bunches of antiprotons is rotated in phase space by 90° so that the short time distribution is traded for a narrow momentum distribution. The bunch rotation results in a decrease in the momentum spread of the antiprotons from 4% to 0.2%. This corresponds to a final energy spread of about 18 MeV. The RF voltage is then adiabatically removed and the antiprotons orbit as one bunch.

The remaining time of the approximately two seconds spent in the debuncher is

occupied by the process of stochastic cooling which decreases the amplitude of betatron oscillations by roughly a factor of two. In regions of low dispersion where longitudinal momentum has the least effect on transverse position, sensors placed above and below the beam record the average vertical and horizontal beam position at each rotation. If the transverse beam position is not ideal, the bunch receives an electromagnetic kick later in that revolution which directs the beam toward the optimum orbit.

In the accumulator, the newly injected antiprotons are decelerated by ≈ 60 MeV through RF manipulation so that they join the lower radius orbit at the tail of the growing *stack* of antiprotons. The momentum of antiprotons in the stack tail is measured in regions of high dispersion where the spread of momentum and thus orbit radii is large. Later in the revolution an appropriate deceleration is applied. This momentum stochastic cooling is used to accumulate antiprotons in the *core* of the stack which is roughly 150 MeV lower in energy than the injection orbit. It is also used to maintain their momentum spread once in the core.

Both momentum and Betatron stochastic cooling are continued in the stack core. When required, a portion of the antiprotons stored in the accumulator is injected back into the Main Ring and from there to the Tevatron.

B.5 Collision of the Proton and Antiproton Beams

In the Tevatron, the relative phase of the RF driving the protons and that driving the antiprotons is adjusted so that the two beams collide at the B0 interaction point. After this procedure, called *cogging*, the beams are accelerated to 900 GeV.

Immediately outside the CDF detector hall are the low-β quadrupole magnets that focus the beams at the collision point to a transverse diameter of $\sigma \leq 0.04$ mm. Stray

protons and antiprotons form a beam halo that is scraped away as the final step before physics data taking begins.

Appendix C

The Level 3 Trigger

Level 3 (L3) is a software trigger and is the last filter in the DAQ path. At 90% livetime and a luminosity of 1.2×10^{31} cm^{-2}s^{-2} the Event Builder outputs at a rate of 22 Hz into L3 which in turn outputs at a rate of 6 Hz to tape. Roughly 75% of the events input to L3 are filtered out and discarded. The output rate of L3 is limited by the speed at which events can be written to tape.

C.1 The Level 3 Hardware

Each of the six SGI boxes has eight nodes and each node has two buffers. Only one buffer in a node may process an event at a time since one executable runs in each node. There is no break in the flow of events through the L3 system since, while one buffer processes an event, the other buffer has a processed event read out and a new event input.

Each one of the six SGI boxes is connected to four Branch Bus cables. Two cables push events into L3 from the two Event Builders, one cable allows the Buffer Multiplexer to pull events from the node and place them in the Global Event Buffer, and the last cable allows the Farm Steward to poll the L3 farm and check for nodes that have finished processing an event and are waiting for output. These programs will be described presently.

Each SGI box has 96 Megabytes of memory. A typical uncompressed event is 160 Kbytes, after L3 compression it is 80 Kbytes. Compared to a VAX 11/780 which can perform one million instructions per second (1 mip), the L3 farm has (according to SGI estimates),

- 1 SGI 280 that can perform 20 mips/node
- 1 SGI 380 that can perform 26 mips/node
- 4 SGI 480s that can perform 32 mips/node

The measured value of the computing power of the L3 SGI farm is 1100 mips.

C.2 Software Used to Control the Event Flow

The software does much more than what is listed below, only the functions directly related to L3 event flow are presented here.

The Event Builder (EVB) formats the events into the YBOS bank structure and pushes the events into L3.

The Buffer Manager acts as a traffic cop, it directs the EVB to push the next event to a selected idle L3 node.

The Farm Steward (FS) informs the Buffer Manager that an event has completed processing in L3. If the Buffer Manager decides that the event should be saved and written to tape, it instructs the Buffer Multiplexer to pull the event from the L3 buffer and place the event in the Global Event Buffer.

A consumer process, selected according to which triggers the event passed, pulls the event from the Global Event Buffer. The consumer processes include:

- the Data Logger which writes all events to tape that are passed by L3,
- YMON to monitor minimum bias events,
- LUMON to monitor luminosity and,
- TRIGMON to monitor trigger types.

The Farm Steward acts as the polling routine. It reads a done bit set in the VRM (a board in each SGI machine) by the node when the node's buffer holds a completed event. The Farm Steward starts the L3 executable running in each node of the L3 farm and shuts down these processes when necessary. The Farm Steward also informs the node executable that a run is to begin and that the run is to be ended. It is not necessary to shut down the L3 farm of node processes between runs.

Level3 Process is the program by which the user interacts with L3. It runs as a subprocess of Run Control, the primary software interface used for data taking. The trigger table name and the node executable name must be provided to Level3 Process by the user at the beginning of each run.

C.3 The Data Structure Input to Level 3

The event pushed into L3 from the EVB is contained in a YBOS bank structure. The CDF event structure is described in [38]. The following YBOS banks are pushed into L3 by the Event Builder.

1) All ***D banks, which contain detector information, are passed from the EVB to L3. For example:

- The calorimetry ***D banks which contain phototube information, e.g. CEMD and PHAD.

- The muon ***D banks which contain the position of hits in the muon detector.

2) The Event Record banks:

- The LRID bank which contains the date, the time of the run, the event number, the creating process ID etc.

- The EVCL bank which contains the 128 bit trigger mask. Each bit represents a L1, L2 or L3 trigger and is set to 1 or 0 depending on whether the trigger passed or failed. When EVCL is pushed into L3, the L1 and L2 bits are set. Of course, the L3 bits will not be set until the event has been processed by L3.

3) The banks containing raw Time to Digital Converter (TDC) information used by the tracking algorithms are pushed into L3 by the EVB. These banks are reformatted within L3. The reformatted TDC banks contain tracking information from the VTX, CTC and Central Muon upgrade.

C.4 Manipulation of the Data Within Level 3

The executable that runs in each of the nodes in the L3 farm is a standard analysis control job that uses all of the production analysis control modules. The event can be reconstructed in L3 exactly as it would be offline with the one exception that global tracking is not implemented in L3.

Analysis control can be thought of as a processing shell that allows the user to combine various code modules to form an executable that reconstructs, filters, and performs analysis on, the events.

Reconstruction of the event means that raw information from the detector is analyzed to determine what physics objects are present in the event. For example, in

reconstructing a high P_t electron in the Central Calorimeter the phototube readout information is taken from the Calorimeter ***D banks and, by use of the analysis control module Calorimetry, is converted into the energy deposited in each calorimeter tower. These energy values are stored in a bank called TOWE. Other analysis control modules can be executed to determine what physics objects are represented by the energy deposition recorded in TOWE.

In L3 an event is reconstructed only to the extent necessary to determine which trigger paths the event passes and which it fails. The analysis control job used to process the events in L3 consists of a trigger table containing a number of different trigger pathways each of which represents a specific physics object such as a photon of given P_t. Some of the modules in the pathway act as filters. If the event as it is reconstructed up to the point where the filter is imposed does not satisfy the cuts required to pass the filter, execution of that trigger pathway is halted and the next trigger path is executed. Each trigger path in the trigger table is executed for each event until the event has failed to pass any filter in the trigger pathway or has passed all filters. The bit in the EVCL trigger mask corresponding to that trigger path is set to 0 or 1 respectively and the next path is executed.

Each analysis control module in the trigger table is executed only once per event even though it may appear in more than one trigger path. Only if the module is called again with a different set of TALKTO parameters is it executed again.

All modules are identical to offline modules except in the following:

1. The TALKTOs, which describe the cuts applied to the data specific to each analysis control module, are different. The only banks that are kept in L3 between

events are the banks that contain the default parameters to be used for the TALK-TOs in the analysis control modules.

2. L3 is running custom analysis control input and output modules whereas offline events are read from tape or disk

C.5 The Data Structure Output By Level 3

Each event that passes a L3 trigger has a processing time of roughly one second. The tracking algorithm, if executed, requires at least one second.

All banks pushed into L3 by the EVB are also written out by L3 for each event that passes. This includes all detector banks, such as LRID and EVCL. The only exception is that banks containing raw TDC information are not passed out of L3. The reformatted TDC banks are passed out of L3.

The only bank output by L3 with information that has been changed after processing in L3 is the EVCL bank. The 128 bit trigger mask in EVCL records which triggers pass or fail in L3 as well as in L1 and L2.

Only a very few small banks created by the analysis control job executed in the L3 nodes are written to tape for each event. Since the event can be fully reconstructed offline it is not necessary to preserve the results of the L3 event reconstruction. It can, however, be specified in the trigger table that for certain events the YBOS banks be preserved. This is done very infrequently. One reason for doing so is to display an event online using the CDF event display program.

Appendix D

Selection of the Lead Jet

The data consist primarily of events in which a photon and single jet emerge from the hard scattering, each with $E_t \approx 18$ GeV. See Fig. D.1a. Additional jets, unassociated with the hard scattering, are found in most events. These are sometimes misidentified as the lead jet although it typically possesses much greater E_t. Figure D.1b shows a comparison between the E_t spectra of the highest E_t, or lead, jet and the second highest E_t jet. Figure D.2 confirms that the additional jets are of relatively low E_t since the requirement that events contain only jets of $E_t > 10$ GeV primarily selects events that contain the lead jet and no additional jets.

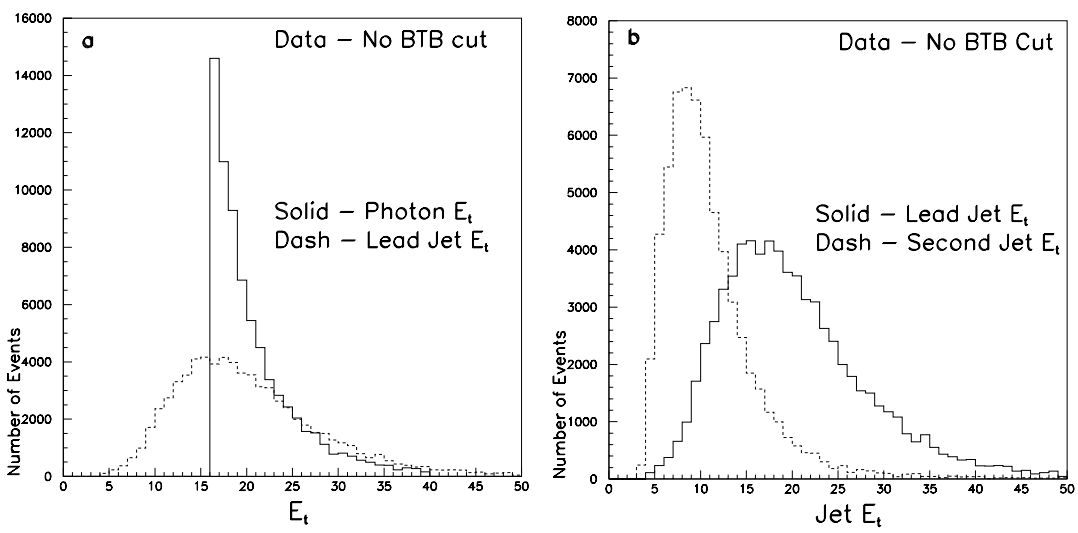

Figure D.1: **a)** The E_t spectrum of the photon and the lead jet both peak at ≈ 18 GeV. **b)** A comparison between the lead jet and the second jet E_t spectra shows that the second jet is typically of much smaller E_t than the lead jet.

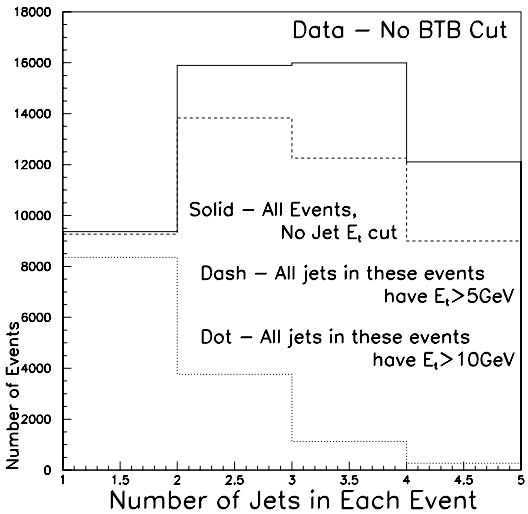

Figure D.2: The number of events that have at least N jets and not N+1 are entered in bin N. A comparison is made between events with jets of any E_t and those events for which all jets have $E_t > 5$ GeV, as well as those events for which all jets have $E_t > 10$ GeV.

Appendix E

The Back-to-Back Cut Selects Events of Limited K_t That Contain Correctly Identified Lead Jets

In photon + 1 jet events, the final interaction products emerge back-to-back in ϕ. Figure E.1 shows $\Delta\phi$ between the photon and lead jet in data events. Most events occupy the peak at $\Delta\phi = 180^o$. Events strongly affected by K_t, events with misidentified lead jets, and photon + 2 jet events occupy the shoulders. Requiring that the photon and lead jet be back-to-back (BTB) in ϕ within $\pm 30^o$, $150^o < \Delta\phi < 210^o$, selects events that exhibit little effect of K_t and contain correctly identified lead jets.

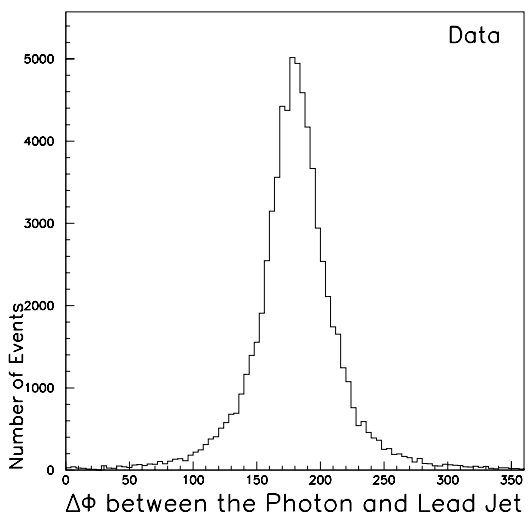

Figure E.1: The back-to-back cut selects events of limited K_t that contain correctly identified lead jets. The events on the shoulder of the peak may be strongly affected by K_t, may contain misidentified lead jets, or may be photon + 2 jet events.

The percentage of events that pass the back-to-back cut in the data and in simulated events of various topology is presented in Tab. E.1.

Table E.1: The percentage of events in which the photon and lead jet are back-to-back within $\pm\phi_{CUT}$. This is presented for the data as well as for simulated events of various topology.

	$\phi_{CUT} = 20^o$	$\phi_{CUT} = 30^o$	$\phi_{CUT} = 40^o$
Event Type			
$2 \rightarrow 2$	95%	97%	98%
$2 \rightarrow 2$+UE	92%	94%	95%
$2 \rightarrow 2+K_t$	67%	83%	92%
$2 \rightarrow 2$+UE$+K_t$	59%	74%	83%
$2 \rightarrow 3$	31%	49%	65%
$2 \rightarrow 3$+UE	30%	48%	64%
$2 \rightarrow 3$+UE$+K_t$	29%	44%	58%
Mixture (before back-to-back cut): 95% of $2 \rightarrow 2$+UE$+K_t$ and 5% of $2 \rightarrow 3$+UE$+K_t$	57%	72%	81%
Mixture (before back-to-back cut): 50% of $2 \rightarrow 2$+UE$+K_t$ and 50% of $2 \rightarrow 3$+UE$+K_t$	44%	59%	71%
Data	58%	72%	82%

E.1 The Back-to-Back Cut Rejects Events Strongly Affected by K_t

Of the $2 \rightarrow 2$+UE events, 94% pass the back-to-back cut. Events strongly affected by K_t are rejected by the back-to-back cut. Of the $2 \rightarrow 2$+UE+K_t events, 74% pass this cut. The data, which are subject to K_t and are primarily photon + 1 jet events, have a passing rate of 72%.

E.2 The Back-to-Back Cut Rejects Events that Contain Misidentified Lead Jets

The lead jet is misidentified when it is replaced with an energy cluster unassociated with the hard scattering or, in a photon + 2 jet event, when the lead and second jets interchange. The back-to-back cut rejects such events.

E.2.1 The Back-to-Back Cut Eliminates Events that Contain No Reconstructed Jet

The 3% of $2 \rightarrow 2$ events that fail the back-to-back cut are primarily events in which the lead jet was not reconstructed. Fragmentation and clustering effects account for the remainder. To be recognized by the clustering algorithm, a jet must deposit at least 1 GeV of E_t in a single calorimeter tower. For the spatially broad low E_t jet this required *seed* E_t may be shared between neighboring towers, not deposited in a single tower. If so the jet is not reconstructed.

The parton η distribution for events with no reconstructed jets, P_i^{NR}, divided by the parton η distribution of all events, P_i, yields, of the partons in each bin, the fraction associated with unreconstructed jets, $R_i^{NR} = P_i^{NR}/P_i$. R_i^{NR} is plotted for various event topologies in Figs. G.1f, H.1f, H.2f, H.3f and H.4f, and is tabulated in Tab. E.2.

This loss decreases the $2 \rightarrow 2$ jet η distribution by $< 6\%$ of its true value in any bin. Introduction of underlying event simulation and $2 \rightarrow 3$ events contributes additional E_t clusters that typically replace an unreconstructed lead jet. Comparison between the $2 \rightarrow 2$+UE events and the $2 \rightarrow 2$ events shows that $> 85\%$ of unreconstructed jets are replaced with underlying event energy. Of the data events before application of the back-to-back cut $< 1\%$ contain no reconstructed jet.

Table E.2: Unreconstructed jets alter the lead jet η distribution.

	Bin 1	Bin 2	Bin 3	Bin 4	Bin 5
R^{NR} for $2 \rightarrow 2$	$< 1\%$	0.01	0.03	0.05	0.03
R^{NR} for $2 \rightarrow 2$+UE	$< 1\%$	$< 1\%$	$< 1\%$	$< 1\%$	$< 1\%$
R^{NR} for $2 \rightarrow 2+K_t$	$< 1\%$	0.01	0.03	0.06	0.06
R^{NR} for $2 \rightarrow 2$+UE$+K_t$	$< 1\%$	$< 1\%$	0.01	0.02	0.02
R^{NR} for $2 \rightarrow 3$+UE$+K_t$	0.00	0.00	0.00	0.00	0.00

E.2.2 The Back-to-Back Cut Rejects Events in which Underlying Event Energy Replaces the Lead Jet

Of the $2 \rightarrow 2$ events, 97% pass the back-to-back cut and, of the $2 \rightarrow 2$+UE events, 94% pass. Replacement of the lead jet with an underlying event energy cluster causes roughly 3% of $2 \rightarrow 2$+UE events to fail the back-to-back cut. The underlying event energy is uniformly distributed throughout the calorimeter so the percentage that fail, $P_{fail} \approx 3\%$, is related to the percentage that pass, P_{pass}, by $P_{pass}/P_{fail} = 60^o/360^o \div 300^o/360^o = 1/5$. This yields $P_{pass} \approx 1\%$ for these events that are unaffected by K_t.

Subtraction of each entry in Tab. F.1, which presents R^G, R^L and ΔR for $2 \rightarrow 2+K_t$

Table E.3: $2 \rightarrow 2$+UE+K_t events combine detector effects that change the distribution of E_t within the jet $\eta - \phi$ cone with those that replace the lead jet with underlying event energy.

	Bin 1	Bin 2	Bin 3	Bin 4	Bin 5
R^G	0.05	0.08	0.16	0.20	0.94
R^L	0.04	0.12	0.11	0.23	0.17
ΔR	$< 1\%$	-0.03	0.05	-0.03	0.77

events, from the corresponding entry in Tab. E.3, which presents R^G, R^L and ΔR for $2 \rightarrow 2$+UE+K_t events, yields the changes to the lead jet η distribution that result from replacement of the lead jet with underlying event energy. See Tab. E.4.

Table E.4: Comparison of $2 \rightarrow 2+K_t$ events with $2 \rightarrow 2$+UE+K_t events demonstrates the effect of underlying event on the lead jet η distribution.

	Bin 1	Bin 2	Bin 3	Bin 4	Bin 5
R^G	0.02	0.03	0.04	0.11	0.66
R^L	0.02	0.03	0.06	0.07	0.10
ΔR	$< 1\%$	$< 1\%$	-0.02	0.04	0.56

When replaced with underlying event energy, the true lead jet often becomes the measured second jet. Figure E.2 shows that $r(\eta, \phi) = (\Delta\eta^2 + \Delta\phi^2)^{1/2}$ between the photon and second jet in $2 \rightarrow 2$+UE events rejected by the back-to-back cut peaks at $\approx \pi$.

E.2.3 The Back-to-Back Cut Rejects $2 \rightarrow 3$ Events in which the Lead and Second Jets Interchange

The data, which are subject to K_t, are primarily photon + 1 jet events, with some contribution from photon + 2 jet events. This contribution is included in the NLO

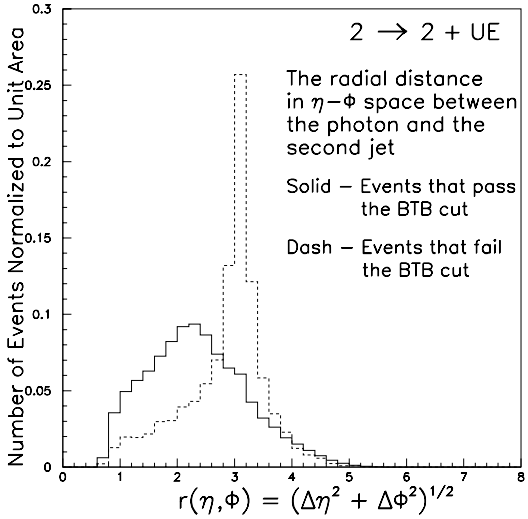

Figure E.2: The radial distance in $\eta - \phi$ space, $r(\eta, \phi) = (\Delta\eta^2 + \Delta\phi^2)^{1/2}$, between the photon and the second jet for 2 $\rightarrow$ 2+UE events.

theory used for comparison to the final measurement. A mixture of 95% 2 $\rightarrow$ 2+UE+K_t events and 5% 2 $\rightarrow$ 3+UE+K_t events pass the back-to-back cut at the rate observed in the data, 72%.

The Photon + 2 Jet Component in the Data

In the data that pass the back-to-back cut the second jet is generally unassociated with the hard scattering event. Figure E.3a demonstrates that $\Delta\phi$ between the lead and second jets in these events is nearly random. The second jet typically arises from lead jet E_t deposited outside of the lead jet $\eta - \phi$ cone as well as underlying event energy. Second jets formed primarily from the former effect occupy the broad peak at $\Delta\phi \approx 50^o$. Figure E.3b shows that the second jet is of low E_t relative to the lead jet in these events and Fig. E.3c confirms that, on average, it is kinematically uncorrelated with the photon and the lead jet.

However, the data that fail the back-to-back cut do exhibit such a correlation. It arises from the rejected photon + 2 jet events. These data show a broad peak at

$\Delta\phi \approx 120^o$ between the lead and second jets in Fig. E.3a and, as demonstrated in Fig. E.3b, typically have lead and second jets of similar E_t. Compare Fig. E.3d to the $2 \rightarrow 3$+UE+K_t events presented in Figs. E.4c and E.4d.

Some photon + 2 jet events pass the back-to-back cut. In Fig. E.3c the average lead jet E_t exceeds the average photon E_t for events with $\Delta\phi > 90^o$ and lies below the average photon E_t for events with $\Delta\phi < 90^o$. Events with dissimilar lead jet and photon E_t require a second jet produced in the hard scattering to balance the transverse momentum.

$2 \rightarrow 3$ events that pass the back-to-back cut have two primary topologies. In one topology, the second jet aligns with the photon and has small E_t relative to the lead jet. The photon and second jet are both roughly back-to-back in ϕ with the lead jet. These events peak at $\Delta\phi \approx 180^o$ in Fig. E.4a and, in Fig. E.4c, appear above $\Delta\phi \approx 90^o$ where the average E_t of the lead jet exceeds that of both the photon and the second jet.

In the other topology the second jet aligns with, and has similar E_t as, the lead jet. Both jets are roughly back-to-back in ϕ with the photon. These events peak at $\Delta\phi \approx 60^o$ in Fig. E.4a and, in Fig. E.4c, appear below $\Delta\phi \approx 90^o$ where the average lead jet E_t lies below that of the average photon E_t.

The Interchange of Lead and Second Jets in $2 \rightarrow 3$ Events

Less than 1% of the data sample are photon + 2 jet events with interchanged lead and second jets. The S50:50 events are a mixture, prior to the back-to-back cut, of 50% $2 \rightarrow 2$+UE+K_t and 50% $2 \rightarrow 3$+UE+K_t events. N_T represents the total number

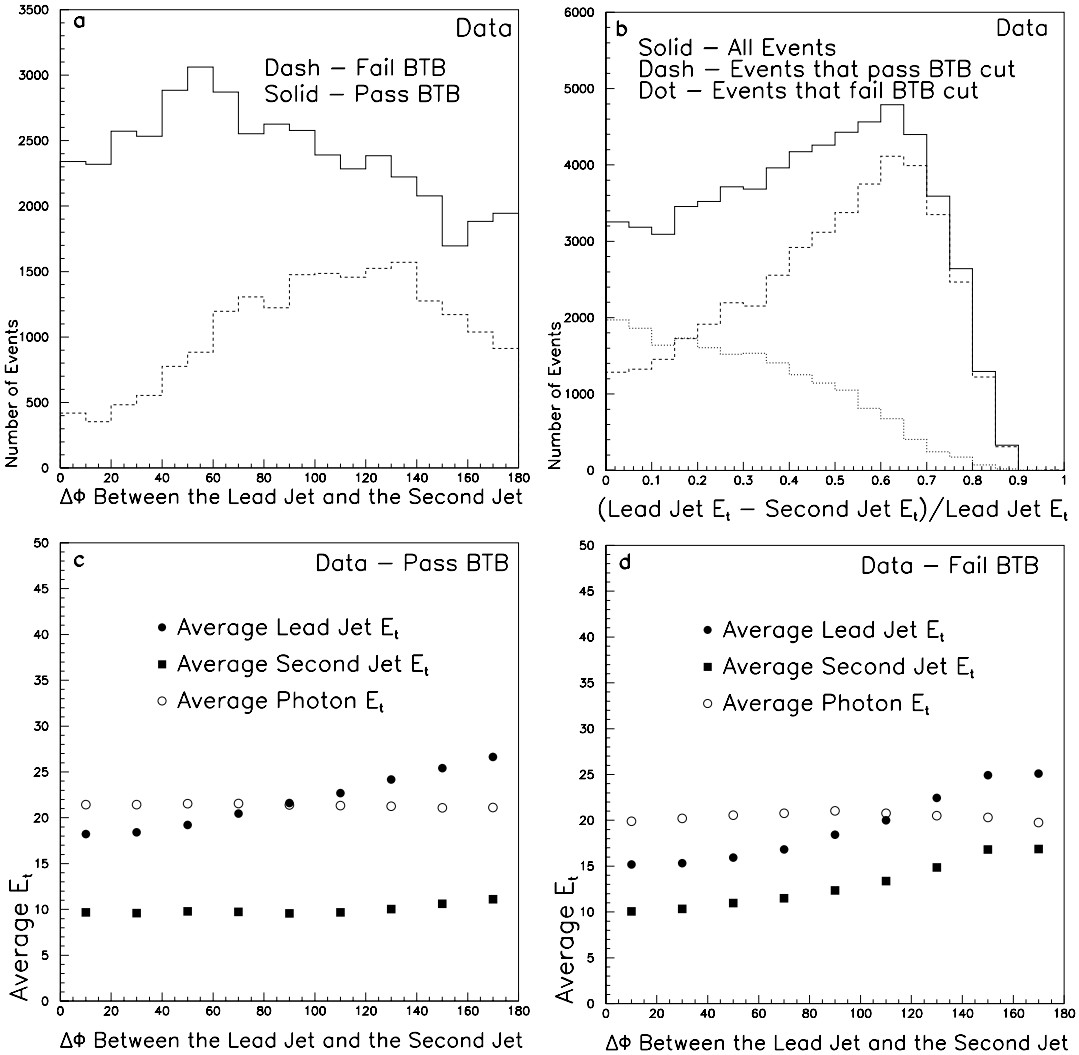

Figure E.3: In the data the **a)** $\Delta\phi$ between the lead and the second jets for events that pass the back-to-back cut as well as for those that fail, **b)** a comparison of the lead jet E_t to the second jet E_t in events that pass the back-to-back cut and in those that fail and **c)** the average E_t of the photon, the lead jet, and the second jet, as a function of $\Delta\phi$ between the lead and the second jets for events that pass the back-to-back cut and **d)** those that fail

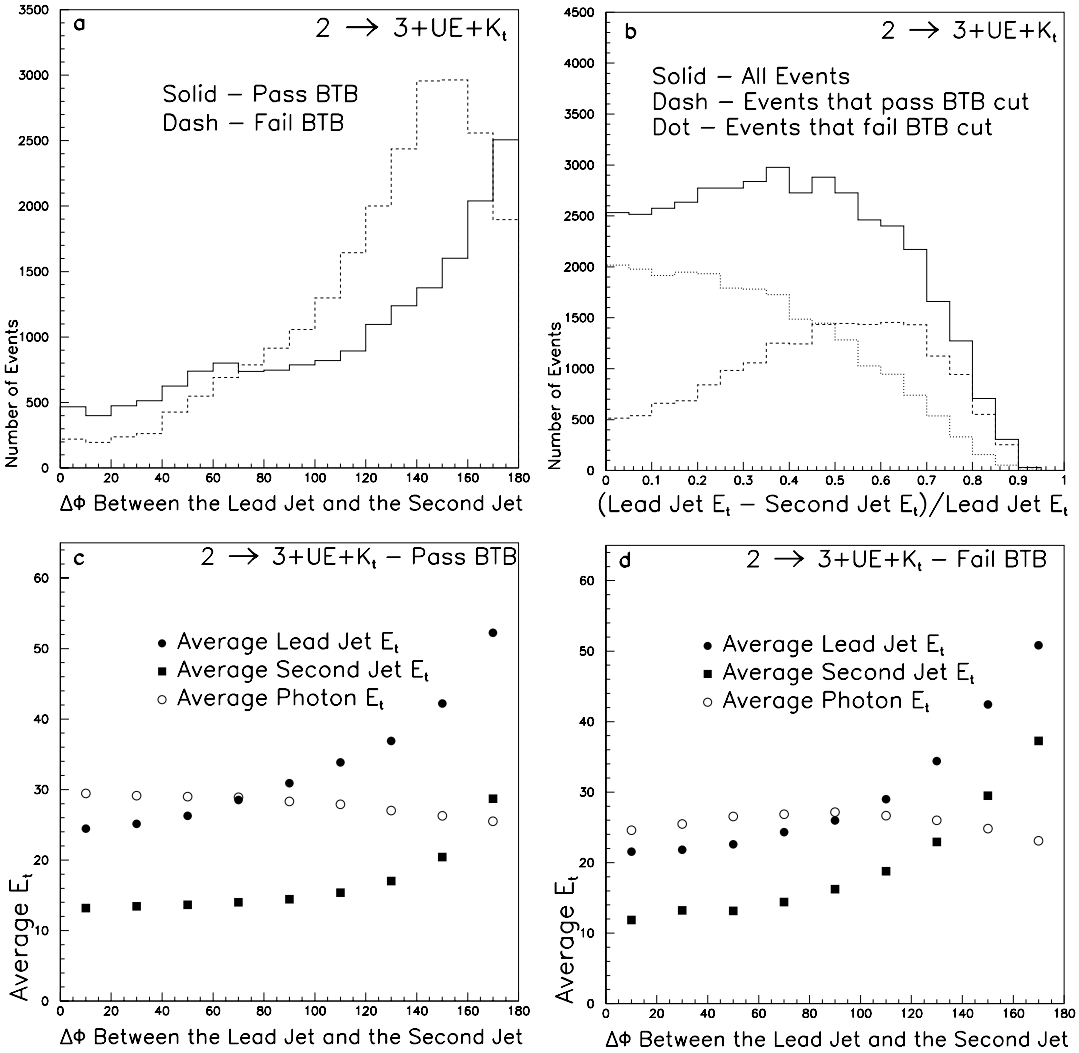

Figure E.4: In the 2 → 3+UE+K_t events the **a)** $\Delta\phi$ between the lead and the second jets for events that pass the back-to-back cut as well as for those that fail, **b)** a comparison of the lead jet E_t to the second jet E_t in events that pass the back-to-back cut and in those that fail and **c)** the average E_t of the photon, the lead jet, and the second jet, as a function of $\Delta\phi$ between the lead and the second jets for events that pass the back-to-back cut and **d)** those that fail

of S50:50 events in the sample. There are $0.41N_T$ events that fail the back-to-back cut and $0.59N_T$ events that pass. The $0.59N_T$ events that pass include $0.22N_T$ $2 \rightarrow 3+\mathrm{UE}+K_t$ events and $0.37N_T$ $2 \rightarrow 2+\mathrm{UE}+K_t$ events. The $0.41N_T$ that fail include $0.28N_T$ $2 \rightarrow 3+\mathrm{UE}+K_t$ events and $0.13N_T$ $2 \rightarrow 2+\mathrm{UE}+K_t$ events. The $0.28N_T$ that are $2 \rightarrow 3+\mathrm{UE}+K_t$ events that fail include $0.03N_T$ with interchanged lead and second jets and the remainder without interchanged lead and second jets. The $0.22N_T$ that are $2 \rightarrow 3+\mathrm{UE}+K_t$ events that pass include $< 0.01N_T$ with interchanged lead and second jets and the remainder without interchanged lead and second jets.

Figure E.5a shows $r(\eta, \phi)$ between the generated lead parton and the associated lead jet in $2 \rightarrow 3+\mathrm{UE}+K_t$ events. Figures E.5b and E.5c present $r(\eta, \phi)$ between the generated lead (second) parton and the second (lead) jet for all these events and for these events that pass the back-to-back cut, respectively. If $r(\eta, \phi) < 0.5$ between the lead jet and second parton *and* $r(\eta, \phi) < 0.5$ between the second jet and lead parton, the event contains interchanged lead and second jets. In such events, the measured lead jet (true second jet) is here referred to as the lead jet and the measured second jet (true lead jet) is referred to as the second jet.

N_N represents the number of $2 \rightarrow 3+\mathrm{UE}+K_t$ events to which no back-to-back cut is applied. Of these, the number with interchanged lead and second jets is N_N^I. The fraction of events with interchanged lead and second jets in this total sample is $F_N^I = N_N^I/N_N$.

After application of the back-to-back cut, the number of $2 \rightarrow 3+\mathrm{UE}+K_t$ events remaining is N_P. Of these, the number with interchanged lead and second jets is N_P^I. The fraction of events with interchanged lead and second jets in this sample of

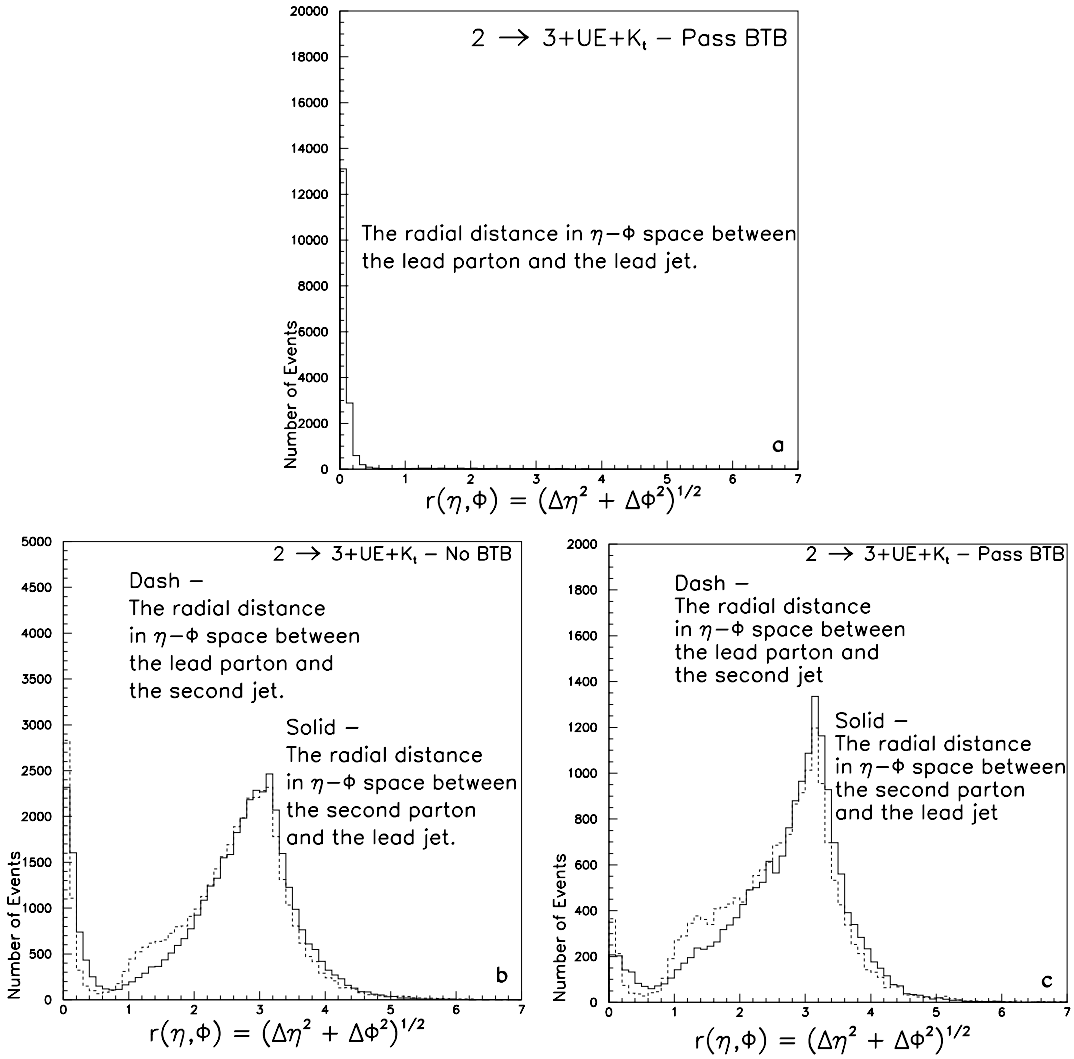

Figure E.5: **a)** The radial distance in $\eta - \phi$ space between the lead parton and the lead jet. Also shown is the radial distance in $\eta - \phi$ space between the lead (second) parton and the second (lead) jet for events **b)** with no back-to-back cut and **c)** that pass the back-to-back cut.

$2 \rightarrow 3+\text{UE}+K_t$ events that pass the back-to-back cut is $F_P^I = N_P^I/N_P$. See Tab. E.5.

Table E.5: The effect of the back-to-back cut on the fraction of $2 \rightarrow 3+\text{UE}+K_t$ events that contain interchanged lead and second jets.

F_N^I	F_P^I
0.07	0.02

Interchanged jets possess similar E_t. This requires an event topology that typically fails the back-to-back cut whether or not the jets are interchanged. See Fig. E.4b. Of the $2 \rightarrow 3+\text{UE}+K_t$ events with no back-to-back cut, N_N, Tab. E.6 lists the fraction that contain interchanged lead and second jets and fail (pass) the back-to-back cut and would have passed (failed) before the interchange or fail (pass) both before and after the interchange.

Table E.6: $2 \rightarrow 3+\text{UE}+K_t$ events with interchanged lead and second jets would typically fail the back-to-back cut whether or not the jets had interchanged.

	Fail After Interchange	Pass After Interchange
Fail Before Interchange	5%	$< 1\%$
Pass Before Interchange	2%	$< 1\%$

In $2 \rightarrow 3+\text{UE}+K_t$ events, the lead parton η distribution of events containing interchanged lead and second jets is P_i^I and the lead parton η distribution of all events is P_i. The fraction $R_i^T = P_i^I/P_i$ is listed in Tab. E.7. For events containing interchanged lead and second jets in which the lead jet and lead parton occupy different bins, J_i^I represents the lead jet η distribution and P_i^I represents the corresponding parton η

distribution. The fractional increase in each bin, $R_i^G = J_i^I/P_i$, the fractional decrease of each bin, $R_i^L = P_i^I/P_i$, and the effective change, $\Delta R_i = R_i^G - R_i^L$, are listed in Tab. E.7.

Table E.7: Interchange of the lead and second jets in 2 $\rightarrow$ 3+UE+K_t events alters the lead jet η distribution.

	Bin 1	Bin 2	Bin 3	Bin 4	Bin 5
R^T	0.01	0.02	0.02	0.02	0.01
R^G	0.02	0.02	0.02	0.02	0.03
R^L	0.01	0.02	0.03	0.02	0.01
ΔR	0.01	$< 1\%$	-0.01	$< 1\%$	0.02

Interchanged lead and second jets have similar E_t. See Fig. E.6b. Below $\Delta\phi \approx 120^o$ between the lead jet and the second jet, events with interchanged lead and second jets that pass the back-to-back cut and those that fail have similar topology. See Figs. E.6c and E.6d. These events have two jets aligned together, both possessing about half the photon E_t. Typically, both jets are roughly back-to-back in ϕ with the photon, and such an event passes the back-to-back cut if the lead and second jets interchange. However, the effects of K_t allow both jets to move away from back-to-back with the photon but remain close together in ϕ. Such an event may fail the back-to-back cut.

As $\Delta\phi$ between the lead and second jets increases beyond $\Delta\phi \approx 120^o$, the E_t of each jet increases. This balances the photon E_t which is restricted to the range $16 < E_t < 40$ GeV. Typically, the true lead jet is more back-to-back in ϕ with the photon than is the true second jet and such an event fails the back-to-back cut if the lead and second jets interchange. However, the effects of K_t allow the true second jet to be more back-to-back in ϕ with the photon than is the true lead jet so that, if these

jets interchange, such an event may pass the back-to-back cut.

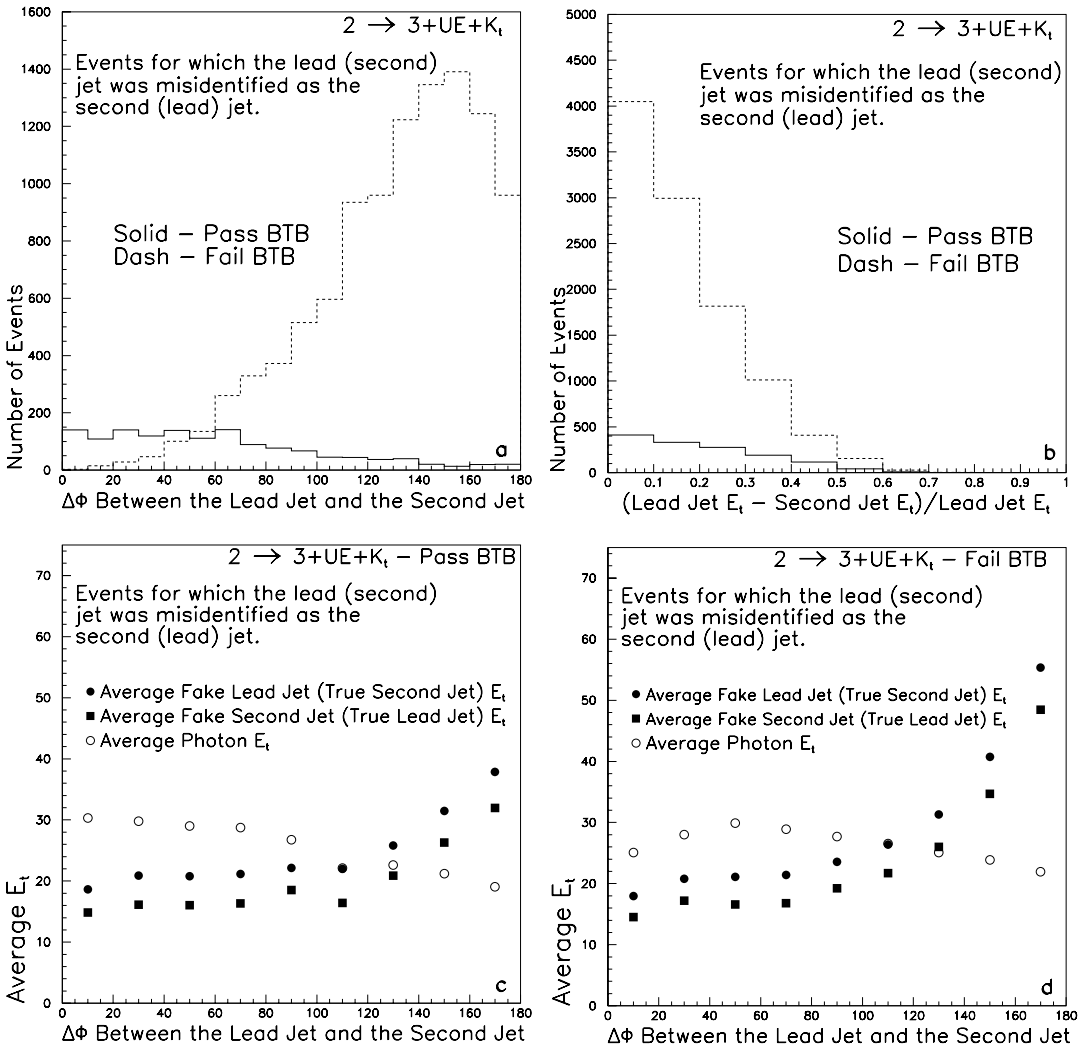

Figure E.6: Events in which the lead and second jets were interchanged were selected from the 2 $\rightarrow$ 3+UE+K_t events. **a)** $\Delta\phi$ between the lead and second jets for events that pass the back-to-back cut as well as for those that fail. **b)** A comparison of the lead jet E_t to the second jet E_t in events that pass the back-to-back cut and in those that fail. **c)** The average E_t of the photon, the lead jet, and the second jet, as a function of $\Delta\phi$ between the lead and second jets for events that pass the back-to-back cut and **d)** those that fail

Appendix F

The Detector Jet η Resolution

For $2 \rightarrow 2+K_t$ events P_i represents the full parton η distribution. For those events in which the lead parton and lead jet occupy different bins, J_i^G represents the jet η distribution and P_i^L represents the parton η distribution. The fraction of events artificially gained by each bin due to detector effects is $R_i^G = J_i^G/P_i$ and the fraction lost is $R_i^L = P_i^L/P_i$. Table F.1 lists R_i^G, R_i^L, and the effective change, $\Delta R_i = R_i^G - R_i^L$. For instance, the net change in bin one is an increase by $< 1\%$ of its true value while the net change in bin four is a decrease by 7% of its true value.

Table F.1: $2 \rightarrow 2+K_t$ events demonstrate detector effects that alter the lead jet η distribution by changing the distribution of E_t within the jet $\eta - \phi$ cone and consequently shifting the E_t-weighted jet centroid.

	Bin 1	Bin 2	Bin 3	Bin 4	Bin 5
R^G	0.03	0.06	0.12	0.09	0.28
R^L	0.03	0.09	0.05	0.16	0.07
ΔR	$< 1\%$	-0.03	0.07	-0.07	0.21

Of the partons in each bin, the fraction separated in η from the associated jet by less than $\Delta\eta$ is presented in Fig. F.1.

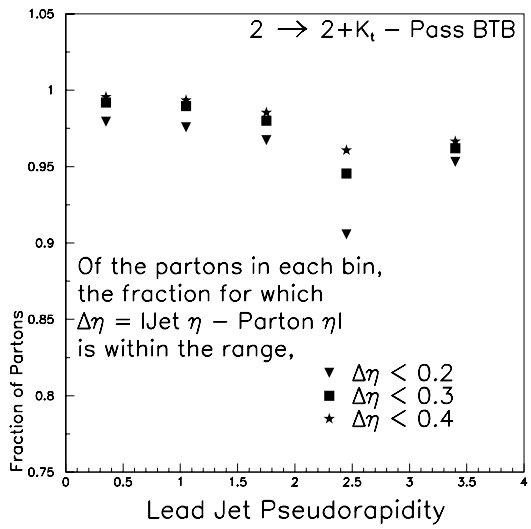

Figure F.1: For 2 → 2+K_t events, of the number of partons in each bin, the fraction for which the difference in η between each parton and its associated jet, $\Delta\eta$, was less than a given value.

F.0.4 The Dependence of Jet η Resolution on Jet E_t

The detector jet η resolution improves as the jet E_t increases. The fraction of partons in each bin reconstructed as jets in a different bin is presented for intervals of lead jet E_t and for different event topologies in Fig. F.2. In 2 → 3 events the lead jet recoils against both the photon and the second jet. Here the lead jet E_t can be larger than that in 2 → 2 events where only one jet exists and must alone balance the photon. See Fig. F.3.

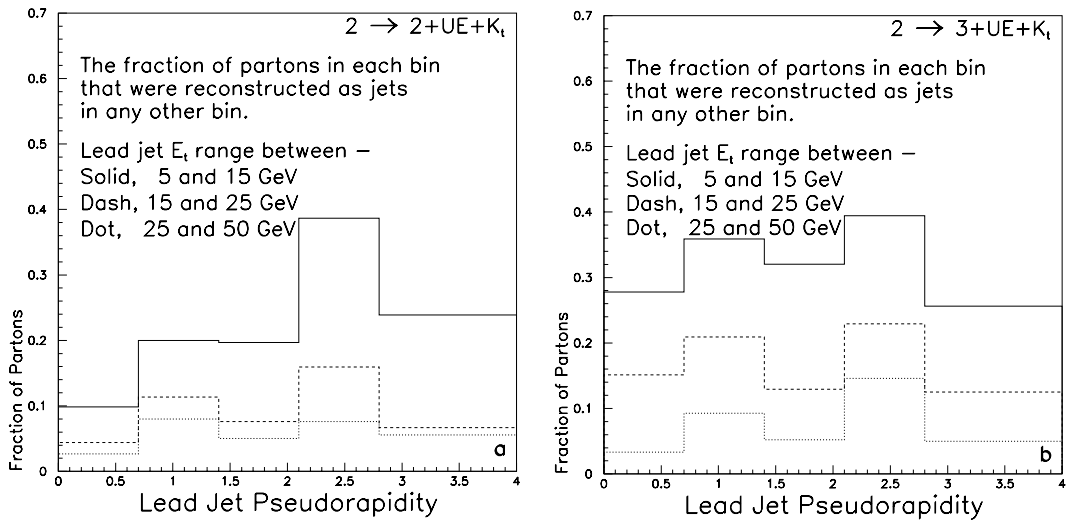

Figure F.2: A comparison of detector η resolution between different event topologies and in the different lead jet E_t ranges, $5 < E_t < 15$, $15 < E_t < 25$, and $25 < E_t < 50$ (in GeV). The fraction of partons in each bin that are associated with jets in any other bin is presented for **a)** the $2 \rightarrow 2+\mathrm{UE}+K_t$ events and **b)** the $2 \rightarrow 3+\mathrm{UE}+K_t$ events.

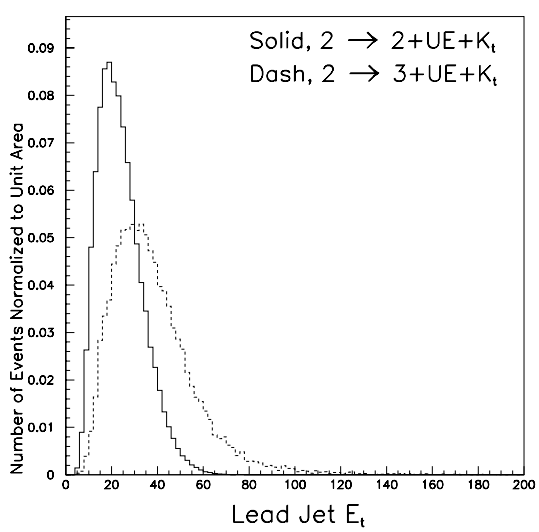

Figure F.3: A comparison of the lead jet E_t distributions in the $2 \rightarrow 2+\mathrm{UE}+K_t$ events and in the $2 \rightarrow 3+\mathrm{UE}+K_t$ events.

Appendix G

Deconvolution of the Lead Jet η Distribution

The information in Fig. G.1 was used to derive Ω, a 5×5 matrix that represents the transformation of the corrected data, D^C, into the uncorrected data, $D^U = \Omega D^C$. For instance, Fig. G.1a shows that roughly 4% of the partons that occupy η bin one, produce a jet that occupies η bin two. Figure G.1f represents the fraction of partons in each bin associated with an unreconstructed jet. The use of partons rather than jets in the denominator of the ratios in Fig. G.1 requires that Ω be derived for application to the corrected data, not the uncorrected data. The inverse of the matrix Ω transforms the uncorrected data into the corrected data, $D^C = \Omega^{-1} D^U$. The vector D^U has five elements containing the uncorrected jet η distribution in the five bins of Fig. G.2.

Figures G.1a-e represent the fraction of partons in bin j that are associated with jets in any other bin $k \neq j$. These fractions are independent of the number of partons in either bin and provide information concerning the detector effects in the region of bin j without introducing spectrum dependence between bins. If Ω had been derived to act directly on the uncorrected data, the ratios of interest would have been the fraction of jets in bin j associated with partons in any other bin k. This procedure was not implemented since this fraction for bin j increases (decreases) as the number of partons in bin k increases (decreases). This would have introduced spectrum dependence between bins j and k.

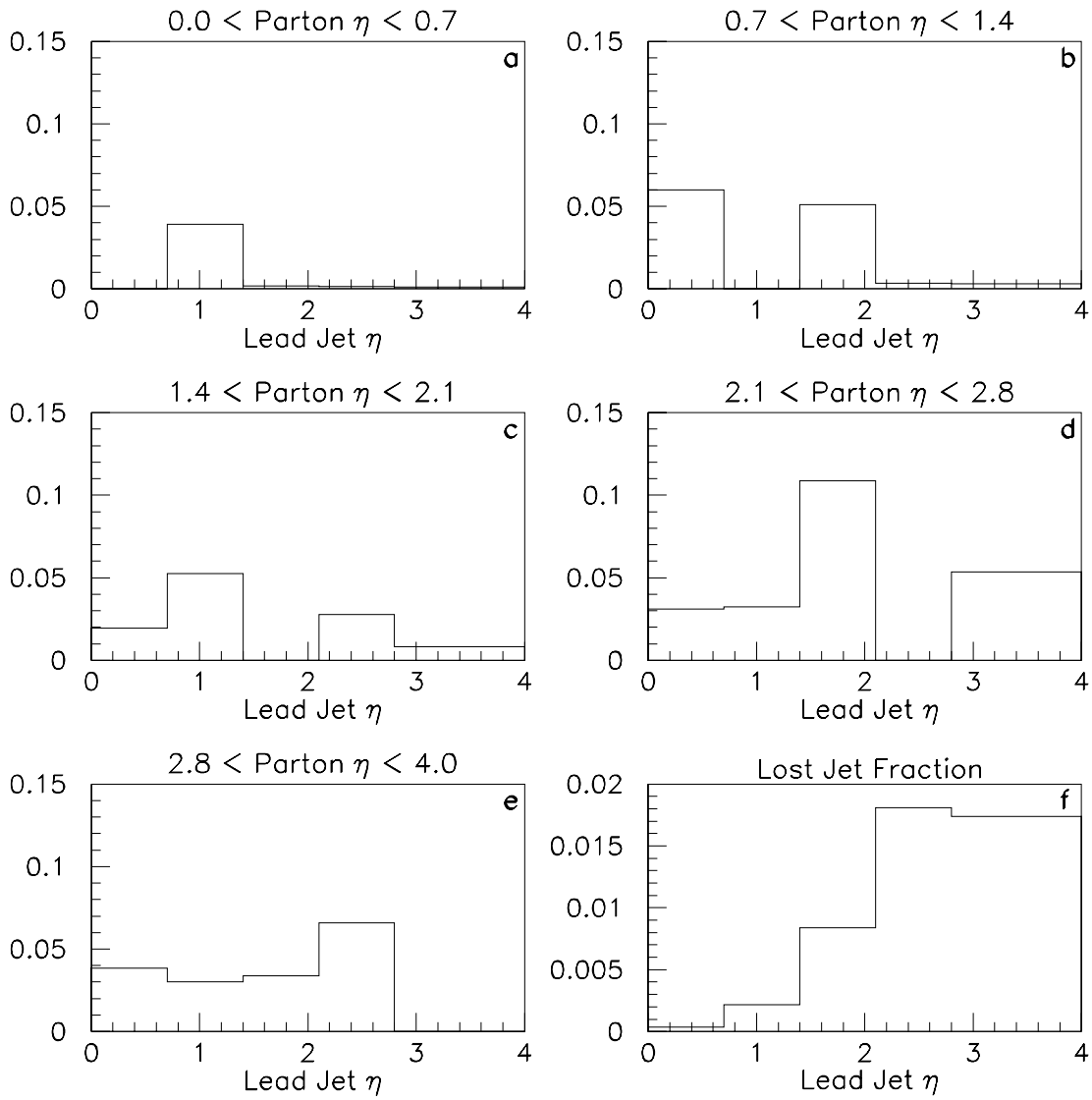

Figure G.1: A study of detector η resolution according to the $2 \rightarrow 2$+UE+K_t events. **a)** The lead jet η of events with parton η in bin 1 and lead jet η **NOT** in bin 1 is plotted, then each bin is divided by the total number of partons in bin 1. The vertical axis represents the fraction of partons in bin 1 reconstructed as jets in each other bin. Figures **b)**-**e)** present this information for bins 2-5 respectively. Figure **f)** represents the fraction of partons in each bin that were not reconstructed as jets anywhere in the detector.

In the following discussion it is always true that $j \neq k$. Make the assignments:

- $R_{jk} \equiv$ Of the partons in bin j, the fraction reconstructed as jets in bin k. These values are obtained directly from Fig. G.1a-e. R_{jk} is a direct measurement of the detector η resolution in the region of bin j and does not depend on the number of partons in bin j or in any other bin k.

- $R_j^{NR} \equiv$ Of the partons in bin j, the fraction not reconstructed as jets anywhere in the detector. These values are obtained directly from Fig. G.1f. This provides the fractional number of jets lost from bin j and not accounted for by the R_{jk} fractions.

The following equations used to calculate the elements of Ω are first presented in terms of bin $j = 1$ then generalized to include all bins. The uncorrected data in bin 1, D_1^U, equals:

- the corrected data in bin 1, D_1^C,

- minus the number of events for which the outgoing parton was in bin 1 but the associated jet was reconstructed in any other bin k,

$$-\sum_k R_{1k} D_1^C,$$

- minus the number of events for which the outgoing parton was in bin 1 but the associated jet was not recorded anywhere in the detector, $-R_1^{NR} D_1^C$,

- plus the number of events for which the outgoing parton was in any other bin k but the associated jet was reconstructed in bin 1,

$$+\sum_k R_{k1} D_k^C.$$

For bin 1, the uncorrected data is written as,

$$D_1^U = D_1^C - \sum_k R_{1k} D_1^C - R_1^{NR} D_1^C + \sum_k R_{k1} D_k^C,$$

or

$$D_1^U = D_1^C (1 - \sum_k R_{1k} - R_1^{NR}) + \sum_k R_{k1} D_k^C.$$

Since

$$D_1^U = \Omega_{11} D_1^C + \sum_k \Omega_{1k} D_k^C$$

it follows that,

$$\Omega_{11} = (1 - \sum_k R_{1k} - R_1^{NR})$$

and,

$$\Omega_{1k} = R_{k1}.$$

The generalization of this to include all bins requires the diagonal elements to be,

$$\Omega_{jj} = (1 - \sum_k R_{jk} - R_j^{NR})$$

and the off-diagonal elements to be,

$$\Omega_{jk} = R_{kj}.$$

The matrix Ω that transforms the corrected data into the uncorrected data is presented here.

$$\Omega = \begin{pmatrix} 0.956 & 0.060 & 0.019 & 0.031 & 0.038 \\ 0.039 & 0.881 & 0.052 & 0.032 & 0.030 \\ 0.002 & 0.051 & 0.885 & 0.107 & 0.033 \\ 0.001 & 0.003 & 0.027 & 0.761 & 0.065 \\ 0.001 & 0.003 & 0.008 & 0.053 & 0.818 \end{pmatrix}$$

To obtain the uncorrected data in bin j, D_j^U, from the corrected data in bin j, D_j^C, two modifications to the contents of D_j^C must be made. D_j^C must be increased by the number of jets reconstructed in bin j but associated with partons in a different bin, k. This value is obtained by summation over all jets in bin j associated with partons in any other bin k,

$$\sum_k \Omega_{jk} D_k^C.$$

Additionally, D_j^C must be decreased by the number of jets associated with a parton in bin j but reconstructed in a different bin k, or not reconstructed at all. The term $\Omega_{jj} D_j^C$ contains this information since the diagonal element, Ω_{jj}, represents the fraction of the corrected data in bin j that remains after the contents of this bin are reduced to account for lost jets.

The four off-diagonal entries in each column j, Ω_{kj}, represent the fraction of partons in bin j reconstructed as jets in a different bin k. The sum of the five elements in each column j differs from unity by the fraction of partons in bin j not reconstructed as jets in bin j or in any other bin. This value, $R_j^{NR} < 0.02$, is given in Fig. G.1f.

For instance, $\Omega_{11} = 0.956$ indicates that $\approx 96\%$ of the partons in bin one were reconstructed as jets in bin one. The $\approx 4\%$ of these partons not reconstructed as jets in bin one were primarily reconstructed as jets in bin two, as indicated by the value of $\Omega_{21} = 0.039$. Likewise, $\Omega_{12} = 0.060$ indicates that $\approx 6\%$ of the partons in the second bin are associated with jets reconstructed in the first bin.

The deconvolution matrix Ω^{-1} transforms the uncorrected data into the corrected data and is given below.

$$\Omega^{-1} = \begin{pmatrix} 1.046 & -0.063 & -0.020 & -0.032 & -0.040 \\ -0.039 & 1.139 & -0.059 & -0.035 & -0.032 \\ -0.002 & -0.051 & 1.134 & -0.119 & -0.040 \\ -0.001 & -0.003 & -0.027 & 1.321 & -0.084 \\ -0.001 & -0.003 & -0.008 & -0.052 & 1.230 \end{pmatrix}$$

The diagonal element, Ω^{-1}_{jj}, represents the fraction by which the uncorrected data in bin j must be increased to correct for the reduction of its value due to detector effects. The four off-diagonal elements, Ω^{-1}_{jk}, in each row, j, represent the fraction of bin k that must be subtracted from $\Omega^{-1}_{jj} D^U_j$ to account for the jets in bin j associated with partons in bin k.

For instance, $\Omega^{-1}_{11} = 1.046$, so the first bin of the uncorrected data is increased by $\approx 5\%$ of its value to correct for lost jets. Likewise, $\Omega^{-1}_{21} = -0.039$ indicates that the contents of bin two must be decreased by $\approx 4\%$ of the value of the uncorrected data in bin one. This accounts for the number of jets in bin two reconstructed from partons in bin one. $\Omega^{-1}_{12} = -0.063$, so $\approx 6\%$ of the uncorrected data in the second bin is subtracted from the contents of the first bin. This corrects for jets in the first bin reconstructed from partons in the second bin.

To test this procedure the corrected jet η distribution of the $2 \rightarrow 2+\mathrm{UE}+K_t$ events, J^C, is divided by the corresponding parton η distribution, P. This yields $R^C = J^C/P$ and is compared to the uncorrected jet η distribution of the $2 \rightarrow 2+\mathrm{UE}+K_t$ events, J^U, divided by P, $R^U = J^U/P$, in Tab. G.1.

The fifth bin, which spans $2.8 < |\eta| < 4.0$, is necessary to the correction of the four bins at lower η. The number of jets in bin five reconstructed from partons with

Table G.1: To test the deconvolution procedure, the corrected simulated jet η distribution is compared to the corresponding generated parton η distribution.

	Bin 1	Bin 2	Bin 3	Bin 4	Bin 5
R^C	1.00	1.00	0.99	0.98	0.98
R^U	1.00	0.97	1.04	0.95	1.74

$|\eta| > 4.0$ is unknown so the correction of its contents is not meaningful.

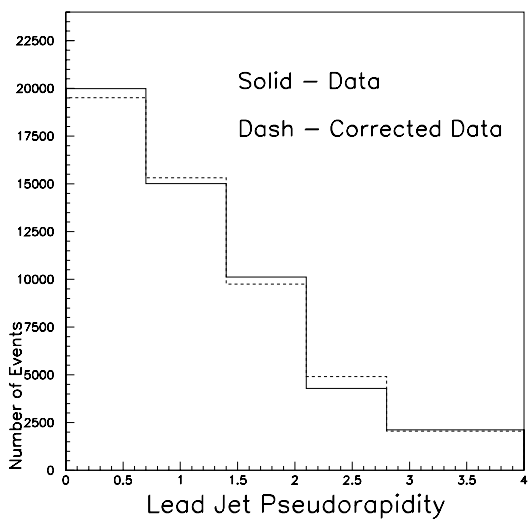

Figure G.2: The data before and after correction for detector effects. The correction to the last bin, $2.8 < |\eta| < 4.0$, is not meaningful since the number of jets that were reconstructed in this bin and associated with partons of $|\eta| > 4.0$ is unknown.

The bin width is a compromise. A large bin width minimizes corrections to each bin. However, an increased number of bins better determines the shape of the distribution. The spanned η range is also a compromise. Higher η values enhance discrimination among parton distributions. However, there are fewer data events at high η and the deconvolution procedure requires a minimum number of data events in the last bin. Beyond $\eta = 2.8$ there are 2121 events while beyond $\eta = 3.2$ there are only 556 events.

Appendix H

The Lead Jet η Resolution in Simulated Events of Various Topology

For comparison with Fig. G.1, the η resolution plots obtained using $2 \rightarrow 2$ events, $2 \rightarrow 2$+UE events, $2 \rightarrow 2+K_t$ events, and $2 \rightarrow 3$+UE$+K_t$ events are shown in Figs. H.1, H.2, H.3 and H.4 respectively. As discussed in Appendix F, the detector jet η resolution improves as the jet E_t increases. For the $2 \rightarrow 2$+UE$+K_t$ events of Fig. G.1d, $\approx 11\%$ of the partons in bin four are reconstructed as jets in bin three. According to Fig. H.4d, this is $\approx 7\%$ in $2 \rightarrow 3$+UE$+K_t$ events.

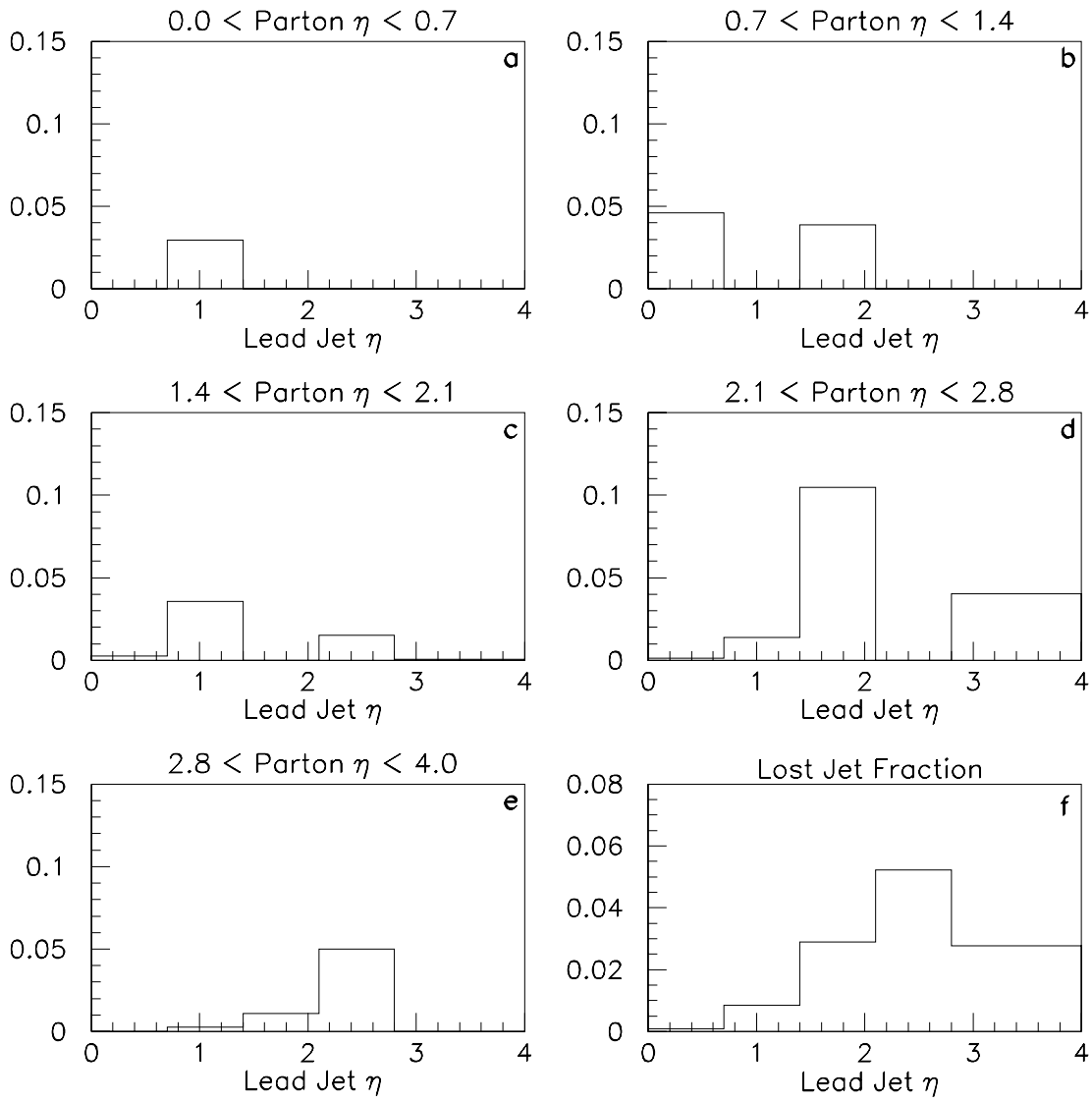

Figure H.1: A study of detector η resolution according to the $2 \rightarrow 2$ events. **a)** The lead jet η of events with parton η in bin 1 and lead jet η **NOT** in bin 1 is plotted, then each bin is divided by the total number of partons in bin 1. The vertical axis represents the fraction of partons in bin 1 reconstructed as jets in each other bin. Figures **b)**-**e)** present this information for bins 2-5 respectively. Figure **f)** represents the fraction of partons in each bin that were not reconstructed as jets anywhere in the detector.

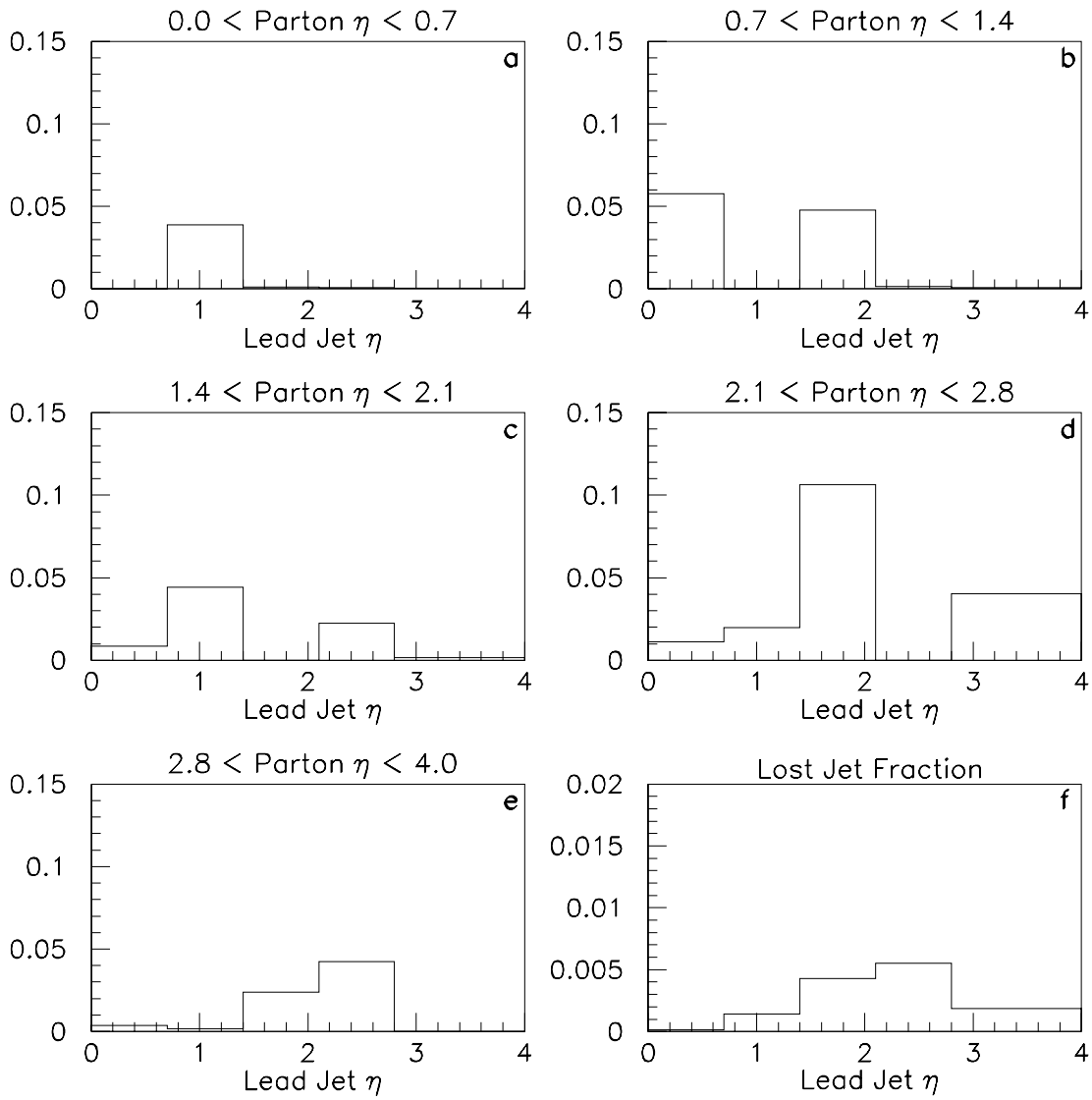

Figure H.2: A study of detector η resolution according to the $2 \rightarrow 2$+UE events. **a)** The lead jet η of events with parton η in bin 1 and lead jet η **NOT** in bin 1 is plotted, then each bin is divided by the total number of partons in bin 1. The vertical axis represents the fraction of partons in bin 1 reconstructed as jets in each other bin. Figures **b)**-**e)** present this information for bins 2-5 respectively. Figure **f)** represents the fraction of partons in each bin that were not reconstructed as jets anywhere in the detector.

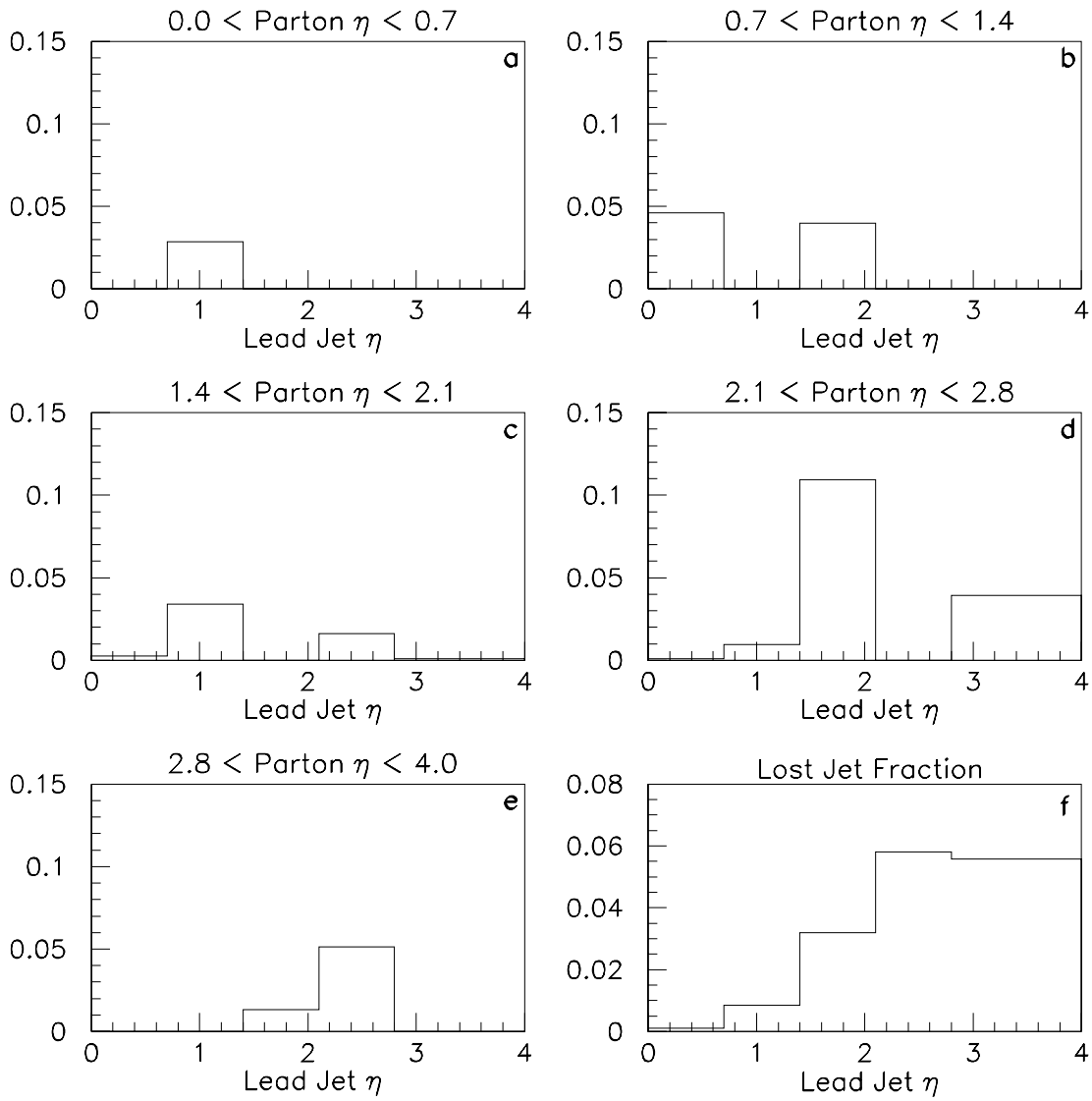

Figure H.3: A study of detector η resolution according to the $2 \rightarrow 2+K_t$ events. **a)** The lead jet η of events with parton η in bin 1 and lead jet η **NOT** in bin 1 is plotted, then each bin is divided by the total number of partons in bin 1. The vertical axis represents the fraction of partons in bin 1 reconstructed as jets in each other bin. Figures **b)**-**e)** present this information for bins 2-5 respectively. Figure **f)** represents the fraction of partons in each bin that were not reconstructed as jets anywhere in the detector.

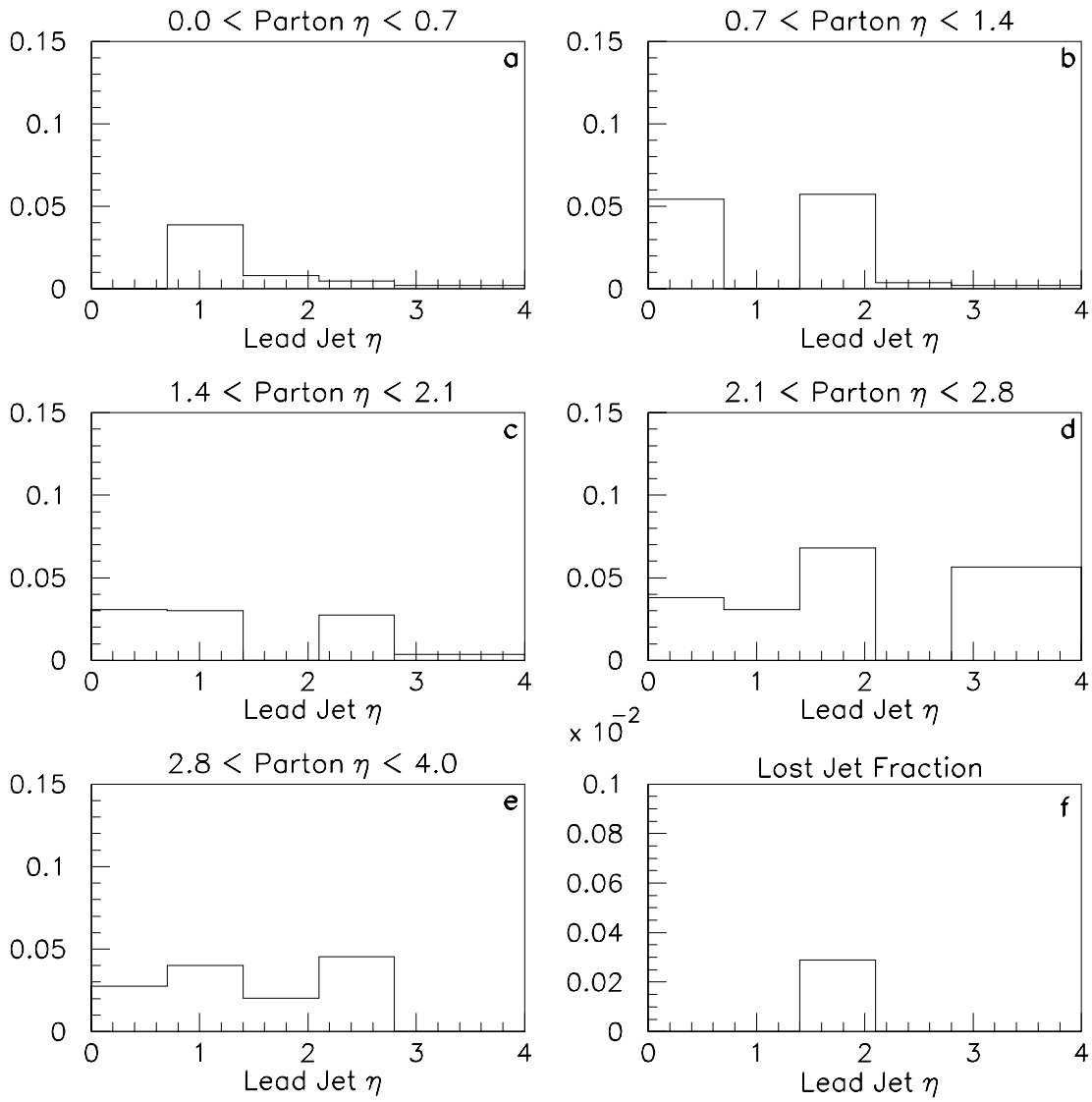

Figure H.4: A study of detector η resolution according to the $2 \rightarrow 3$+UE+K_t events. **a)** The lead jet η of events with parton η in bin 1 and lead jet η **NOT** in bin 1 is plotted, then each bin is divided by the total number of partons in bin 1. The vertical axis represents the fraction of partons in bin 1 reconstructed as jets in each other bin. Figures **b)**-**e)** present this information for bins 2-5 respectively. Figure **f)** represents the fraction of partons in each bin that were not reconstructed as jets anywhere in the detector.

Appendix I

The Systematic Uncertainty Associated with the Detector Simulation

In the detector simulation program, QFL, transverse shower spreading is described by one routine for the central calorimeters and another routine for the forward calorimeters. If a particle deposits energy in more than one detector, whichever detector the particle first encounters corresponds to the routine that is used. In most cases, shower energy that spreads beyond the physical dimension of the detector is not recorded, it is considered to be lost. The routine that models the shower spreading for the scintillator calorimeters also includes the PHA (gas) calorimeter so that if the energy of a particle is deposited in both the WHA and the PHA, the energy from each detector is recorded. In the routine that simulates the shower spreading in the FHA and FEM calorimeters, any shower energy that spreads beyond the physical extent of the detector is modeled as lost and is not recorded.

The jet cone spans several calorimeter towers. An energy fluctuation in one tower shifts the E_t-weighted jet centroid and may move the jet out of the correct η bin. See Tab. F.1. Such changes to the distribution of E_t within the jet $\eta - \phi$ cone occur more frequently for jets that overlap the detector η cracks. Misidentification of the lead jet through loss of total jet E_t occurs more often in these regions as well.

Two sets of $2 \rightarrow 2+\mathrm{UE}+K_t$ events were designed to test this effect. In each set the

simulated distribution of E_t within the jet $\eta - \phi$ cone was altered prior to clustering. In one set, referred to here as the S50% events, energy recorded in the towers bordering the three detector η cracks was increased by 50% of its value. In the other set, referred to here as the S0 events, this energy was set to zero.

Each calorimeter tower is assigned a number, from 1 to 84, that increases with η. Tower 1 edges on $\eta = -4.2$ and tower 84 edges on $\eta = +4.2$. The number assigned to each tower that borders an η crack is listed below for positive (negative) η.

Central Crack:	EM and HAD Towers 43,(42)	$\lvert\eta_D\rvert < 0.1308$
Plug Crack:	EM Towers 52,53 (33,32)	$1.1 < \lvert\eta_D\rvert < 1.2$
	HAD Towers 54,55 (31,30)	$1.2 < \lvert\eta_D\rvert < 1.4$
Forward Crack:	EM and HAD Towers 66, (19)	$2.3 < \lvert\eta_D\rvert < 2.4$

The S50% events determine the systematic uncertainty associated with the simulated distribution of jet E_t within the jet $\eta - \phi$ cone near the detector cracks. Table I.1 lists the difference, $\Delta B^{50\%}$, between the data corrected using this simulation, $D^{50\%}$, and those corrected with the standard simulation, D^C.

The S0 events overestimate the effect and provide an upper limit on the uncertainty. Table I.1 lists the difference, ΔB^0, between the data corrected using this simulation, D^0, and those corrected with the standard simulation, D^C.

The S50% and S0 events exhibit fluctuations in mean jet E_t that correspond to the altered energy in the crack regions. These are comparable to the difference between the *dijet balancing* [30] plots of QFL and the data. Dijet balancing models jet energy loss in the η cracks. A dijet event results from a $2 \rightarrow 2$ process and produces two

Table I.1: The sensitivity of the deconvolution matrix, Ω^{-1}, to the simulated distribution of jet E_t near the detector η cracks.

	Bin 1	Bin 2	Bin 3	Bin 4
D^C	1.000	1.017	1.073	1.074
$D^{50\%}$	1.000	0.984	1.126	1.037
D^0	1.000	1.091	0.967	1.116
$\Delta B^{50\%}$	0.000	0.033	-0.053	0.037
ΔB^0	0.000	-0.074	0.106	-0.042

jets balanced in E_t. Excluding detector effects and K_t, their E_t ratio, R_{DJ}, should be unity.

In Fig. I.1 [36] one jet is constrained to the central detector and the other, the probe jet, ranges over all η. Detector effects become evident through the behavior of R_{DJ} when the probe jet loses energy in the detector η cracks. This ratio is similar for the data, R^D_{DJ}, and for the detector simulation, R^{QFL}_{DJ}, as shown in Fig. I.1.

Table I.2 compares the mean E_t of jets with η in the crack regions, E_t^{CR}, to the mean E_t of jets with η in the central region, E_t^{CEN}. The central region is $0.4 < |\eta| < 0.6$, and the crack regions are $|\eta| < 0.1308$, $1.1 < |\eta| < 1.4$, and $2.3 < |\eta| < 2.4$. So that $\eta_D \approx \eta$, the events used in this study were selected to have $|z| < 25$ cm. This comparison takes the form $\Delta E_t \equiv |(E_t^{CEN} - E_t^{CR})|/E_t^{CEN}$. For S50% events this is $\Delta E_t^{50\%}$ and for S0 events this is ΔE_t^0.

To demonstrate that the S50% events provide a reasonable estimate of E_t fluctuations, Tab. I.2 shows that $\Delta E_t^{50\%}$ is consistent with $S = R^D_{DJ} - R^{QFL}_{DJ}$.

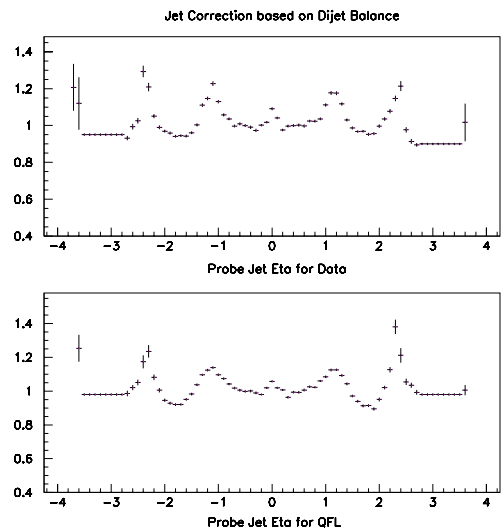

Figure I.1: A dijet balancing plot representing R^{D}_{DJ} and R^{QFL}_{DJ} [36]. In the η crack regions these ratios depart from unity.

Table I.2: A comparison between the mean jet E_t in the central detector and in the crack regions for simulated events with a non-standard distribution of energy within the jet $\eta - \phi$ cone for jets that overlap the η cracks. Also presented is the difference between the data and the detector simulation dijet balancing plots of Fig. I.1 in the relevant η regions.

	$\Delta E_t^{50\%}$	ΔE_t^{0}	S
$0.4 < \lvert\eta\rvert < 0.6$	2%	9%	1-2%
$1.1 < \lvert\eta\rvert < 1.4$	9%	18%	5-8%
$2.3 < \lvert\eta\rvert < 2.4$	3%	10%	5-10%

Appendix J

The Systematic Uncertainty Associated With the Underlying Event Simulation

To test the sensitivity of Ω^{-1} to the underlying event, the standard correction, which uses underlying event simulation, is compared to one that does not. Table J.1 presents the data subjected to the standard correction, D^C, and the data subjected to this variation of the standard correction, D^{NoUE}.

Table J.1: The sensitivity of the deconvolution matrix, Ω^{-1}, to the underlying event.

	Bin 1	Bin 2	Bin 3	Bin 4
D^C	1.000	1.017	1.073	1.074
D^{NoUE}	1.000	1.008	1.025	1.031

Replacing the parton with a neutrino in 2 $\rightarrow$ 2+UE events produces a set of simulated events in which every 'jet' results from an upward fluctuation of the underlying event energy since the weakly interacting neutrino is not recorded in the detector. The fraction of these events with a cluster of E_t above a given threshold exceeds that in the minimum bias data for each of the E_t thresholds presented in Tab. J.2. Figure J.1 compares the E_t distribution of these events with that of minimum bias events. SET-PRT overestimates the amount of underlying event energy found in the data. Even so,

the corrected data are insensitive to addition or deletion of underlying event energy in the simulated events. See Tab. J.1

Table J.2: A comparison between the fraction of events, F^J, with at least one jet of $E_t > E_t^{MIN}$ in data events recorded using a minimum bias trigger and in the simulation of the underlying event energy by SETPRT.

E_t^{MIN}	Minimum Bias Events F^J	Simulated Underlying Event Energy F^J
1 GeV	0.43	0.98
5 GeV	0.37	0.95
10 GeV	0.09	0.36
15 GeV	0.02	0.08

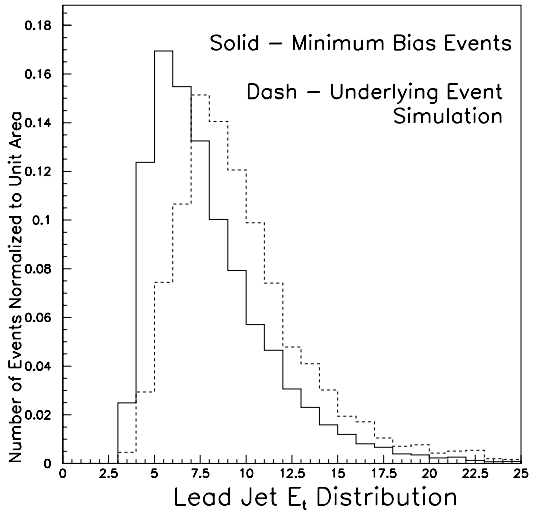

Figure J.1: A comparison between the E_t spectra of clusters in minimum bias events and in the simulated underlying event.

Appendix K

The Systematic Uncertainty Associated With Photon + 2 Jet Events

To test the sensitivity of Ω^{-1} to the $2 \rightarrow 3$ process, the standard correction, which uses $2 \rightarrow 2+\mathrm{UE}+K_t$ events exclusively, is compared to one that uses a mixture of simulated events. This mixture, prior to the back-to-back cut, consists half of $2 \rightarrow 2+\mathrm{UE}+K_t$ and half of $2 \rightarrow 3+\mathrm{UE}+K_t$ events. Table K.1 presents the data subjected to the standard correction, D^C, and the data subjected to this variation of the standard correction, D^{NLO}.

Table K.1: The sensitivity of the deconvolution matrix, Ω^{-1}, to the $2 \rightarrow 3$ process.

	Bin 1	Bin 2	Bin 3	Bin 4
D^C	1.000	1.017	1.073	1.074
D^{NLO}	1.000	1.019	1.067	1.056

Appendix L

The Systematic Uncertainty Associated With K_t and Variation of the Back-to-Back Cut

Soft gluon emission from the initial or final state parton affects the momentum of the outgoing photon and jet. Specifically, this K_t may impart jet momentum transverse to the direction defined by the photon. The back-to-back cut requires the photon and lead jet to be back-to-back in ϕ within $\Delta\phi = \pm 30^o$ and rejects events strongly affected by K_t. To test the sensitivity of Ω^{-1} to the back-to-back cut, the standard correction, which uses $\Delta\phi = \pm 30^o$, is compared to that using $\Delta\phi = \pm 20^o$ and that using $\Delta\phi = \pm 40^o$. Tightening the back-to-back cut selects events that are more likely to contain correctly identified lead jets. Table L.1 presents the data subjected to the standard correction, D^C, and the data subjected to these variations of the standard correction, D^{BTB20^o} and D^{BTB40^o}.

Table L.1: The sensitivity of the deconvolution matrix, Ω^{-1}, to variation of the back-to-back cut.

	Bin 1	Bin 2	Bin 3	Bin 4
D^C	1.000	1.017	1.073	1.074
D^{BTB20^o}	1.000	1.019	1.082	1.023
D^{BTB40^o}	1.000	1.034	1.095	1.069

Comparison of the standard correction, which includes K_t simulation, to one that does not tests the sensitivity of Ω^{-1} to K_t. Table L.2 presents the data subjected to the standard correction, D^C, and the data subjected to this variation of the standard correction, D^{NoK_t}.

Table L.2: The sensitivity of the deconvolution matrix, Ω^{-1}, to the effect of K_t.

	Bin 1	Bin 2	Bin 3	Bin 4
D^C	1.00	1.017	1.073	1.074
D^{NoK_t}	1.00	1.008	1.036	1.037

Appendix M

The Systematic Uncertainty Associated With the Spectrum Dependence of the Deconvolution Procedure

As discussed in Appendix G, there is no spectrum dependence between the different bins represented in the ratios R_{jk} and R_j^{NR} that comprise Ω. However, the shape of the spectrum within each bin presents an unavoidable spectrum dependence. If the generated spectrum is steeper than that of the data, the η resolution of the detector in the lower η region within each bin is overemphasized and that of the higher η region underemphasized.

To test the sensitivity of Ω^{-1} to the generated parton η spectrum, the standard correction, which uses Martinelli parton distributions, is compared to that using the parton η spectrum dictated by either the CTEQ2MF or the CTEQ2ML parton distributions. The CTEQ2MF and CTEQ2ML parton distributions yield the largest theoretical variation in Fig. 5.5. Table M.1 presents the data subjected to the standard correction, D^C, and the data subjected to these variations of the standard correction, D^{2MF} and D^{2ML}.

Figure M.1 shows a shape comparison between the η distribution that results from the Martinelli parton distributions used in Papageno for generation of the simulated events, and that that results from the CTEQ2M parton distributions used in the NLO QCD theoretical calculation.

Table M.1: The sensitivity of the deconvolution matrix, Ω^{-1}, to the η spectrum of the generated events.

	Bin 1	Bin 2	Bin 3	Bin 4
D^C	1.000	1.017	1.073	1.074
D^{2MF}	1.000	1.017	1.084	1.043
D^{2ML}	1.000	1.017	1.086	1.038

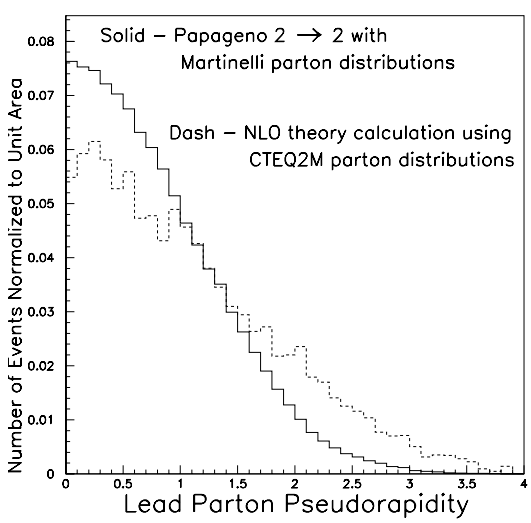

Figure M.1: A comparison between the lead jet η spectrum corresponding to Martinelli parton distributions and that corresponding to CTEQ2M parton distributions.

Appendix N

The Systematic Uncertainty Associated with the Background Subtraction

The CPR limited systematic uncertainty for the CES background subtraction method yields an $< 2\%$ uncertainty in the shape of the lead jet η distribution. The final measurement is divided by the value of the central bin and is essentially independent of the photon E_t. See Fig. 2.10. Most of the systematic uncertainty resulting from the background subtraction cancels in the ratio.

The weight applied to each data event is modified to reflect a 1 σ systematic uncertainty in the inclusive photon cross section. Table N.1 presents the data with the standard background subtraction, D^C, and the data subjected to the modified background subtraction, D^{BS}.

Table N.1: The systematic uncertainty associated with the subtraction of multiple photon background.

	Bin 1	Bin 2	Bin 3	Bin 4
D^C	1.000	1.017	1.073	1.074
D^{BS}	1.000	1.016	1.072	1.076

Appendix O

The CDF Collaboration

F. Abe,[13] M. G. Albrow,[7] S. R. Amendolia,[22] D. Amidei,[16] J. Antos,[28] C. Anway-Wiese,[4] G. Apollinari,[26] H. Areti,[7] M. Atac,[7] P. Auchincloss,[25] F. Azfar,[21] P. Azzi,[20] N. Bacchetta,[20] W. Badgett,[16] M. W. Bailey,[18] J. Bao,[35] P. de Barbaro,[25] A. Barbaro-Galtieri,[14] V. E. Barnes,[24] B. A. Barnett,[12] P. Bartalini,[22] G. Bauer,[15] T. Baumann,[9] F. Bedeschi,[22] S. Behrends,[3] S. Belforte,[22] G. Bellettini,[22] J. Bellinger,[34] D. Benjamin,[31] J. Benlloch,[15] J. Bensinger,[3] D. Benton,[21] A. Beretvas,[7] J. P. Berge,[7] S. Bertolucci,[8] A. Bhatti,[26] K. Biery,[11] M. Binkley,[7] F. Bird,[29] D. Bisello,[20] R. E. Blair,[1] C. Blocker,[3] A. Bodek,[25] W. Bokhari,[15] V. Bolognesi,[22] D. Bortoletto,[24] C. Boswell,[12] T. Boulos,[14] G. Brandenburg,[9] C. Bromberg,[17] E. Buckley-Geer,[7] H. S. Budd,[25] K. Burkett,[16] G. Busetto,[20] A. Byon-Wagner,[7] K. L. Byrum,[1] J. Cammerata,[12] C. Campagnari,[7] M. Campbell,[16] A. Caner,[7] W. Carithers,[14] D. Carlsmith,[34] A. Castro,[20] Y. Cen,[21] F. Cervelli,[22] H. Y. Chao,[28] J. Chapman,[16] M.-T. Cheng,[28] G. Chiarelli,[22] T. Chikamatsu,[32] C. N. Chiou,[28] L. Christofek,[10] S. Cihangir,[7] A. G. Clark,[22] M. Cobal,[22] M. Contreras,[5] J. Conway,[27] J. Cooper,[7] M. Cordelli,[8] C. Couyoumtzelis,[22] D. Crane,[1] J. D. Cunningham,[3] T. Daniels,[15] F. DeJongh,[7] S. Delchamps,[7] S. Dell'Agnello,[22] M. Dell'Orso,[22] L. Demortier,[26] B. Denby,[22] M. Deninno,[2] P. F. Derwent,[16] T. Devlin,[27] M. Dickson,[25] J. R. Dittmann,[6] S. Donati,[22] R. B. Drucker,[14] A. Dunn,[16] K. Einsweiler,[14] J. E. Elias,[7] R. Ely,[14] E. Engels, Jr.,[23] S. Eno,[5] D. Errede,[10] S. Errede,[10] Q. Fan,[25] B. Farhat,[15] I. Fiori,[2] B. Flaugher,[7] G. W. Foster,[7] M. Franklin,[9] M. Frautschi,[18] J. Freeman,[7] J. Friedman,[15] H. Frisch,[5] A. Fry,[29] T. A. Fuess,[1] Y. Fukui,[13] S. Funaki,[32] G. Gagliardi,[22] S. Galeotti,[22] M. Gallinaro,[20] A. F. Garfinkel,[24] S. Geer,[7] D. W. Gerdes,[16] P. Giannetti,[22] N. Giokaris,[26] P. Giromini,[8] L. Gladney,[21] D. Glenzinski,[12] M. Gold,[18] J. Gonzalez,[21] A. Gordon,[9] A. T. Goshaw,[6] K. Goulianos,[26] H. Grassmann,[6] A. Grewal,[21] L. Groer,[27] C. Grosso-Pilcher,[5] C. Haber,[14] S. R. Hahn,[7] R. Hamilton,[9] R. Handler,[34] R. M. Hans,[35] K. Hara,[32] B. Harral,[21] R. M. Harris,[7] S. A. Hauger,[6] J. Hauser,[4] C. Hawk,[27] J. Heinrich,[21] D. Cronin-Hennessy,[6] R. Hollebeek,[21] L. Holloway,[10] A. Hölscher,[11] S. Hong,[16] G. Houk,[21] P. Hu,[23] B. T. Huffman,[23] R. Hughes,[25] P. Hurst,[9] J. Huston,[17] J. Huth,[9] J. Hylen,[7] M. Incagli,[22] J. Incandela,[7] H. Iso,[32] H. Jensen,[7] C. P. Jessop,[9] U. Joshi,[7] R. W. Kadel,[14] E. Kajfasz,[7a] T. Kamon,[30] T. Kaneko,[32] D. A. Kardelis,[10] H. Kasha,[35] Y. Kato,[19] L. Keeble,[8] R. D. Kennedy,[27] R. Kephart,[7] P. Kesten,[14] D. Kestenbaum,[9] R. M. Keup,[10] H. Keutelian,[7] F. Keyvan,[4] D. H. Kim,[7] H. S. Kim,[11] S. B. Kim,[16] S. H. Kim,[32] Y. K. Kim,[14] L. Kirsch,[3] P. Koehn,[25] K. Kondo,[32] J. Konigsberg,[9] S. Kopp,[5] K. Kordas,[11] W. Koska,[7] E. Kovacs,[7a] W. Kowald,[6] M. Krasberg,[16] J. Kroll,[7] M. Kruse,[24] S. E. Kuhlmann,[1] E. Kuns,[27] A. T. Laasanen,[24] N. Labanca,[22] S. Lammel,[4] J. I. Lamoureux,[3] T. LeCompte,[10] S. Leone,[22] J. D. Lewis,[7] P. Limon,[7] M. Lindgren,[4] T. M. Liss,[10] N. Lockyer,[21] C. Loomis,[27] O. Long,[21] M. Loreti,[20] E. H. Low,[21] J. Lu,[30] D. Lucchesi,[22] C. B. Luchini,[10] P. Lukens,[7] J. Lys,[14] P. Maas,[34] K. Maeshima,[7] A. Maghakian,[26] P. Maksimovic,[15] M. Mangano,[22] J. Mansour,[17] M. Mariotti,[20] J. P. Marriner,[7] A. Martin,[10] J. A. J. Matthews,[18] R. Mattingly,[15] P. McIntyre,[30]

P. Melese,[26] A. Menzione,[22] E. Meschi,[22] G. Michail,[9] S. Mikamo,[13] M. Miller,[5] R. Miller,[17] T. Mimashi,[32] S. Miscetti,[8] M. Mishina,[13] H. Mitsushio,[32] S. Miyashita,[32] Y. Morita,[32] S. Moulding,[26] J. Mueller,[27] A. Mukherjee,[7] T. Muller,[4] P. Musgrave,[11] L. F. Nakae,[29] I. Nakano,[32] C. Nelson,[7] D. Neuberger,[4] C. Newman-Holmes,[7] L. Nodulman,[1] S. Ogawa,[32] S. H. Oh,[6] K. E. Ohl,[35] R. Oishi,[32] T. Okusawa,[19] C. Pagliarone,[22] R. Paoletti,[22] V. Papadimitriou,[31] S. P. Pappas,[35] S. Park,[7] J. Patrick,[7] G. Pauletta,[22] M. Paulini,[14] L. Pescara,[20] M. D. Peters,[14] T. J. Phillips,[6] G. Piacentino,[2] M. Pillai,[25] R. Plunkett,[7] L. Pondrom,[34] N. Produit,[14] J. Proudfoot,[1] F. Ptohos,[9] G. Punzi,[22] K. Ragan,[11] F. Rimondi,[2] L. Ristori,[22] M. Roach-Bellino,[33] W. J. Robertson,[6] T. Rodrigo,[7] J. Romano,[5] L. Rosenson,[15] W. K. Sakumoto,[25] D. Saltzberg,[5] A. Sansoni,[8] V. Scarpine,[30] A. Schindler,[14] P. Schlabach,[9] E. E. Schmidt,[7] M. P. Schmidt,[35] O. Schneider,[14] G. F. Sciacca,[22] A. Scribano,[22] S. Segler,[7] S. Seidel,[18] Y. Seiya,[32] G. Sganos,[11] A. Sgolacchia,[2] M. Shapiro,[14] N. M. Shaw,[24] Q. Shen,[24] P. F. Shepard,[23] M. Shimojima,[32] M. Shochet,[5] J. Siegrist,[29] A. Sill,[31] P. Sinervo,[11] P. Singh,[23] J. Skarha,[12] K. Sliwa,[33] D. A. Smith,[22] F. D. Snider,[12] L. Song,[7] T. Song,[16] J. Spalding,[7] L. Spiegel,[7] P. Sphicas,[15] L. Stanco,[20] J. Steele,[34] A. Stefanini,[22] K. Strahl,[11] J. Strait,[7] D. Stuart,[7] G. Sullivan,[5] K. Sumorok,[15] R. L. Swartz, Jr.,[10] T. Takahashi,[19] K. Takikawa,[32] F. Tartarelli,[22] W. Taylor,[11] P. K. Teng,[28] Y. Teramoto,[19] S. Tether,[15] D. Theriot,[7] J. Thomas,[29] T. L. Thomas,[18] R. Thun,[16] M. Timko,[33] P. Tipton,[25] A. Titov,[26] S. Tkaczyk,[7] K. Tollefson,[25] A. Tollestrup,[7] J. Tonnison,[24] J. F. de Troconiz,[9] J. Tseng,[12] M. Turcotte,[29] N. Turini,[22] N. Uemura,[32] F. Ukegawa,[21] G. Unal,[21] S. C. van den Brink,[23] S. Vejcik, III,[16] R. Vidal,[7] M. Vondracek,[10] D. Vucinic,[15] R. G. Wagner,[1] R. L. Wagner,[7] N. Wainer,[7] R. C. Walker,[25] C. Wang,[6] C. H. Wang,[28] G. Wang,[22] J. Wang,[5] M. J. Wang,[28] Q. F. Wang,[26] A. Warburton,[11] G. Watts,[25] T. Watts,[27] R. Webb,[30] C. Wei,[6] C. Wendt,[34] H. Wenzel,[14] W. C. Wester, III,[7] T. Westhusing,[10] A. B. Wicklund,[1] E. Wicklund,[7] R. Wilkinson,[21] H. H. Williams,[21] P. Wilson,[5] B. L. Winer,[25] J. Wolinski,[30] D. Y. Wu,[16] X. Wu,[22] J. Wyss,[20] A. Yagil,[7] W. Yao,[14] K. Yasuoka,[32] Y. Ye,[11] G. P. Yeh,[7] P. Yeh,[28] M. Yin,[6] J. Yoh,[7] C. Yosef,[17] T. Yoshida,[19] D. Yovanovitch,[7] I. Yu,[35] J. C. Yun,[7] A. Zanetti,[22] F. Zetti,[22] L. Zhang,[34] S. Zhang,[16] W. Zhang,[21] and S. Zucchelli[2]

(CDF Collaboration)

[1] *Argonne National Laboratory, Argonne, Illinois 60439*

[2] *Istituto Nazionale di Fisica Nucleare, University of Bologna, I-40126 Bologna, Italy*

[3] *Brandeis University, Waltham, Massachusetts 02254*

[4] *University of California at Los Angeles, Los Angeles, California 90024*

[5] *University of Chicago, Chicago, Illinois 60637*

[6] *Duke University, Durham, North Carolina 27708*

[7] *Fermi National Accelerator Laboratory, Batavia, Illinois 60510*

[8] *Laboratori Nazionali di Frascati, Istituto Nazionale di Fisica Nucleare, I-00044 Frascati, Italy*

[9] *Harvard University, Cambridge, Massachusetts 02138*

[10] *University of Illinois, Urbana, Illinois 61801*

[11] *Institute of Particle Physics, McGill University, Montreal H3A 2T8, and University of Toronto, Toronto M5S 1A7, Canada*

[12] *The Johns Hopkins University, Baltimore, Maryland 21218*

[13] *National Laboratory for High Energy Physics (KEK), Tsukuba, Ibaraki 305, Japan*

[14] *Lawrence Berkeley Laboratory, Berkeley, California 94720*

[15] *Massachusetts Institute of Technology, Cambridge, Massachusetts 02139*

[16] *University of Michigan, Ann Arbor, Michigan 48109*

[17] *Michigan State University, East Lansing, Michigan 48824*

[18] *University of New Mexico, Albuquerque, New Mexico 87131*

[19] *Osaka City University, Osaka 588, Japan*
[20] *Universita di Padova, Istituto Nazionale di Fisica Nucleare, Sezione di Padova, I-35131 Padova, Italy*
[21] *University of Pennsylvania, Philadelphia, Pennsylvania 19104*
[22] *Istituto Nazionale di Fisica Nucleare, University and Scuola Normale Superiore of Pisa, I-56100 Pisa, Italy*
[23] *University of Pittsburgh, Pittsburgh, Pennsylvania 15260*
[24] *Purdue University, West Lafayette, Indiana 47907*
[25] *University of Rochester, Rochester, New York 14627*
[26] *Rockefeller University, New York, New York 10021*
[27] *Rutgers University, Piscataway, New Jersey 08854*
[28] *Academia Sinica, Taiwan 11529, Republic of China*
[29] *Superconducting Super Collider Laboratory, Dallas, Texas 75237*
[30] *Texas A&M University, College Station, Texas 77843*
[31] *Texas Tech University, Lubbock, Texas 79409*
[32] *University of Tsukuba, Tsukuba, Ibaraki 305, Japan*
[33] *Tufts University, Medford, Massachusetts 02155*
[34] *University of Wisconsin, Madison, Wisconsin 53706*
[35] *Yale University, New Haven, Connecticut 06511*

References

[1] CTEQ Collaboration, *Handbook of Perturbative QCD*, (1993).

[2] F. Halzen and A. Martin, *Quarks and Leptons: An Introductory Course in Modern Particle Physics*, John Wiley and Sons, Inc. 1984.

[3] J.F.Owens, Rev. of Mod. Phys. **59** 465 (1987).

[4] P.N.Harriman, *et al.*, Phys. Rev. **D 42** 798 (1990).

[5] J.G. Morfin and W.K.Tung, Z. Phys. **C 52**, 13-29 (1991).

[6] A.D. Martin, *et al.*, Phys. Rev. **D 43** 3648 (1991).

[7] P.N. Harriman, *et al.*, Phys. Lett. **B 243** 421 (1990).

[8] F. Abe, *et al.*, Phys. Rev. Lett. **74** 2626 (1995).

[9] J. Ohnemus, H. Baer and J.F. Owens, Phys. Rev. **D 42** 61 (1990).

[10] C. Yosef, Private Communication (1995).

[11] C. Hawk, "A Measurement of the Leading Jet η Boost and η^* distribution in Direct Photon plus Jet Events", CDF Note 2668.

[12] J. Botts *et al.*, The CTEQ Collaboration, Phys. Lett. **B 304** 159 (1993).

[13] H.L. Lai, Phys. Rev. **D 51** 4763-4782 (1995).

[14] Phys. Rev. **D 47** 867 (1993).

[15] I. Hinchliffe (LBL, Berkeley). "The Papageno Partonic Monte Carlo Program", LBL-34372, 7pp. (1993). Submitted to the *Workshop on Physics at Current Accelerators and the Supercollider*, Argonne, IL, June 2-5, 1993.

[16] D. Brown, "A Single Parton Fragmentation Module", CDF Note 1916.

[17] M. Shapiro, "A User's Guide to QFL", CDF Note 1810.

[18] ISAJET Monte Carlo version 3.12, I. Hinchliffe, (to be published).

[19] E. Kovacs, Private Communication (1994).

[20] F. Abe, *et al.*, Nucl. Inst. and Meth. **A 271**, 387 (1988), and the references therein.

[21] J. Thompson, "Introduction to Colliding Beams at Fermilab", FERMILAB-TM-1909 (1994).

[22] H. Goldstein, *Classical Mechanics* , Addison-Wesley Publishing Company, 1980.

[23] W.R. Leo, *Techniques for Nuclear and Particle Physics Experiments*, Springer-Verlag Berlin Heidelberg, 1987.

[24] F. Abe, *et al.* (CDF Collaboration), Phys. Rev. **D 48** 2998 (1993). F. Abe, *et al.* (CDF Collaboration), Phys. Rev. Lett. **68**, 2734 (1992).

[25] F. Abe, *et al.* (CDF Collaboration), Phys. Rev. Lett. **73** 2662 (1994).

[26] Y.S. Tsai., Rev. Mod. Phys. **46** 815 (1974).

[27] R. Brun *et al.* GEANT3. CERN DD/EE/84-1.

[28] A. Maghakian, "Isolation Cut Efficiency in Direct Photon Analysis", CDF Note 2214.

[29] A. Maghakian, "Inclusive Photon Cross Section 1992", CDF Note 1963.

[30] L. Keeble, "New Jet Correction Function QDJSCO 2.0", CDF Note 1513.

[31] J. Tonnison, "QDJSCO Corrections for 6.01 Data", CDF Note 2053.

[32] J. Tonnison, "A Pre-Release of Jet Corrections for 6.1 Data", CDF Note 2189.

[33] B. Flaugher, "Calibration Stability and the Jet Energy Scale: Run 0 and Run 1A Compared", CDF Note 2902.

[34] A. Bhatti, "Inclusive Jet Cross Section From 1992-93 Data Set", CDF Note 1971.

[35] R. Harris, "Calibration of CPR Conversion Probability from Fully Reconstructed η and π^o Mesons", CDF Note 2318.

[36] J. Tonnison, Private Communication, (1994).

[37] M. Diemoz, F. Ferroni, E. Longo, and G. Martinelli Z. Phys. **C 39** 21 (1988).

[38] D. Quarrie, "The CDF Event Structure", CDF Note 152.

Vita

Carol Margaret Hawk

1982 Graduated from George Mason High School, Falls Church, Virginia.

1983-84 Attended University of Massachusetts, Amherst, Massachusetts.

1984-87 Attended University of Virginia, Charlottesville, Virginia. Majored in Physics.

1987 B.A., University of Virginia.

1987-96 Graduate work in Physics, Rutgers, The State University of New Jersey, New Brunswick, New Jersey.

1987-90 Teaching Assistant, Department of Physics.

1990-96 Graduate Research Assistant, Department of Physics.

1994 C. Hawk for the CDF Collaboration, A Study of Parton Distribution Functions with the use of Photon + Jet Event Kinematics in $p\bar{p}$ Collisions at $\sqrt{s} = 1.8$ TeV. Proceedings of 1994 Meeting of the American Physical Society, Division of Particles and Fields (DPF 94), Albuquerque, NM, 2-6 Aug (1994).

1994 F. Abe et al. (CDF Collaboration), A Precision Measurement of the prompt photon cross-section in $p\bar{p}$ Collisions at $\sqrt{s} = 1.8$ TeV. Phys. Rev. Lett. **73**, 2662 (1994).

1995 F. Abe et al. (CDF Collaboration), Observation of Top Quark Production in $p\bar{p}$ Collisions. Phys. Rev. Lett. **74**, 2626 (1995).

1996 Ph.D. in Physics and Astronomy.